KTH Industrial Engineering and Management

Multifunctional magnetic materials prepared by Pulsed Laser Deposition

Sandeep Nagar

Doctoral Dissertation

Stockholm 2012

Royal Institute of Technology
School of Industrial Engineering and Management
Department of Material Science and Engineering
Technical Material Physics Division
Fakultelsopponent. Prof. Prashant Kamat, Univ. of Notredam, IN, USA

Akademisk avhandling som med tillstånd av Kungliga Tekniska Högskolan I Stockholm framlägges för offentlig granskning för avläggande av teknologie doktorsexamen Tisdagen den **29 Maj 2012**, **kl. 10 i F3** Kungliga Tekniska Högskolan, Stockholm.

ABSTRACT of the Thesis Content

Pulsed LASER deposition (PLD) is widely recognized as excellent deposition technique owing to stoichiometric transfer of target material, easy preparation and high quality. Thin films from few nanometers to micrometer regime can be fabricated with equal ease. Although a batch process is not suitable for mass scale industrial production, PLD is a versatile technique, efficient and convenient for high quality basic research. This thesis illustrates the use of PLD technique to study the emerging trends in tailoring multifunctional magnetic thin films both from basic nanoscience and device development point of view.

After a comprehensive review of magnetism in chapter 1. entitled *'A journey through classical to modern trends in magnetism, and multifunctional thin film devices'* followed by a reasonably thorough discussion on Pulsed Laser thin film technique in Chapter 2, we present.

1) Studies of tailoring composite high energy product permanent magnetic FePtB based thin films for applications in NEMS /MEMS, (Chapter 3).

2) Study of search for new multiferroic materials by investigating the properties of Chromites. Crystalline Chromites are antiferromagnetic below 150^{o}C. However depositing thin films by PLD off the crystalline 95.5% dense targets produced by Surface Plasma Sintering, we discovered that the resulting films were amorphous and ferromagnetic beyond room temperature. Moreover advanced spectroscopic techniques revealed that the amorphized state is metallic with Cr in a mixed valence state. An understanding of the underlying physics of the observed phenomenon has been carried out based on first principles calculations. These results are now being considered for publication in a high profile journal. Extensive studies on the films showing that these materials are ferromagnetic, but not ferroelectric are discussed in chapter 4. A preliminary presentation of these studies was pier reviewed and published in MRS symposium proceedings.

3) Fabrication of Room temperature, Transparent, high moment soft ferromagnetic amorphous Bulk metallic glass based FeBNbY thin films by PLD, suitable for Nanolithography in NEMS/MEMS device development . (Chapter 5). A manuscript is being submitted to a high profile journal.

From a basic study point of view on new trends on magnetism we present.

4) The use of PLD technique to demonstrate room temperature ferromagnetism in undoped MgO, and V-doped MgO thin films (discussed in chapter 6). Both of these oxides which do not contain any intrinsically magnetic elements and are diamagnetic in their bulk form belong to a new class of magnetic films, the so called d^0 magnets signifying that robust above room temperature ferromagnetism arising from defects and controlled carriers and no occupied d-states can be tailored in semiconductors and insulators. A paper with first principles calculations on magnetism in MgO has apprared in Applied Physics Letters, and the paper on V doped MgO has been submitted. These, mostly ZnO and MgO based thin films which may be classified as Dilute Magnetic Semiconductors, DMS, and Dilute Magnetic Insulators, DMI, are now the materials of active interest in future Electronics involving components which exploit both charge and spin of electrons in the arena of SPINTRONICS.

Extensive characterization of magnetic, electrical, optical properties and microscopic structure with strong international collaboration has ensured development of high quality magnetic materials for future applications. Further research on these promising materials is expected to yield new generation spintronic devices for better performance in terms of efficiency, energy consumption and miniaturization of sizes.

Present document is dedicated to those who chose to remain untamed and followed the tougher path of challenging authorities

Acknowledgments

It'd been a long and challenging path until this work could have appeared in the current shape. Many persons, plenty of events and happily fortune returns, have come across that way in a certain period of my life that has an important contribution to the Thesis, you are reading at the moment. The list of names I am thankful to, would probably fit in a telephone book. Without their aid, without their support, without their encouragement this work probably could not have been even started at all. To all these people I am sending my warm gratitude and acknowledgments.

I am thankful to Prof. K.V. Rao for allowing me to work at his lab and guiding me through all the projects. It is my privilege to thank Prof. Misuteru Inoue (Japan), Prof. Jinghua Guo (Berkeley), Prof. Gillian Gehring (Sheffield, UK), Prof. Akihisa Inoue (Sendai, Japan), Prof. J.F.Scott (Cambridge UK),and Prof. A.K.Tyagi (BARC, India), Prof. Gunnar Niklasson (Uppsala), Prof. Rajiv Ahuja (Uppsala) and some of their group members for many interactions during my research collaborations with them. I am also thankful to Dr. L. Belova and Anastasiia Riazanova for their assistance with SEM/FIB characterization of all samples in my research. I am also very thankful to Dr. Tamaki for his valuable assistance in teaching me Faraday rotation experimental technique. I am very thankful to Dr. V. Ström for very useful discussions, assistance during operation and repair of equipment and guidance during challenging times in the investigations. Dr. Parmanand Sharma, Mr. Ansar, Dr. Mukes Kapilashrami, Dr. Yan Wu, Dr. German Salazar Alvarez, Dr. Emad, Dr. O.D. Jayakumar, Dr. S.M. Lee, Dr. Tarja Volotinen, Ms. Mei, Mr. Sreekanth have all extended a very helping hand during my work and I am very grateful to them. I am also very thankful to Prof. D.R.S Somayajulu for encouraging me to pursue further studies in physics during and after my M.Sc.

Above the all I wish to thank my family for the grand support that they extended to me in difficult times. I thank my father and mother for giving me excellent educational, social and financial opportunities to make it up till here and I thank my brother and sister-in-law for extending much needed supports of all kinds to keep myself in perfect fit mental state.

I am very thankful to funding agencies: VINNOVA, KTH and HERO-M projects for their financial support for the research projects involved in this thesis.

Table of Contents

List of publications from this thesis work

Publications from this thesis work*

(* *in all the papers below my contribution consists of fabrication of the films by PLD, characterization by XRD, SQUID etc., analyses of the data, and among others initial manuscript preparation.*
Note: In all the papers attached herein, except in one, I am the first author from our group)

1. **Exchange-coupled FePtB nano-composite hard magnets produced by pulsed laser deposition**
   Neelam Kaushik ,Parmanand Sharma, ***Sandeep Nagar****, K.V. Rao, Hisamichi Kimura, Akihiro Makino and Akihisa Inoue*, *Materials Science and Engg. B,*171 **(2010)** 62-68
   My contribution: This collaborative project with Prof. Sharma and his student Neelam was carried out in our labs using PLD and I did most of the work including SQUID measurements, analysis and write up of the part of the work done at Tmfy-MSE
2. **Room Temperature Ferromagnetism and Lack of Ferroelectricity in Thin films of 'Biferroic?' $YbCrO_3$,**
   Sandeep Nagar*, K.V Rao, Lyubov Belova, G. Catalan, J. Hong, J. F Scott, A. K Tyagi, O. D Jayakumar, R. Shukla, Yi Sheng Liu and Jinghua Guo,*
   Mater. Res. Soc. Symp. Proc. Vol. 1161 **(2009)**1161-I07-04
   My contribution: The discovery of ferromagnetism in chromite work on amorphization, and complete structural and magnetic characterization , and initial write up is by myself
3. **Transformation to Room Temperature Ferromagnetism on Amorphizing Chromite Thin Films**
   *C. Moyses….****Sandeep Nagar****…et al. (under review,-only abstract page included)*
   My contribution: this high profile journal submission is a result of collaboration with six theorists and is based on my experimental finding of RT-Ferromagnetism. My contribution is the experimental part along with colleagues from Berkeley who collaborated on the spectroscopic study.
4. **Magnetic and electronic properties of glassy $(Fe_{72}B_{24}Nb_4)_{95.5}Y_{4.5}$ ferromagnetic thin films fabricated using Pulsed Laser Deposition technique**
   Sandeep Nagar *et al* ***(to be published)***
   My contribution: This original work on BMG based thin films was an '*invited talk' at* IUMRS, Japan.
5. **A new material for Magneto-Optical applications.$(Fe_{72}B_{24}Nb_4)_{95.5}Y_{4.5}$glassy thin film**
   Sandeep Nagar *et al* ***(to be published)***
   My contribution: Production of films by PLD, Characterization by SQUID, XRD, resistivity, Faraday rotation investigations, analyses, initial manuscript etc
6. **Room temperature ferromagnetism in pristine MgO thin films**
   C. Moyses Araujo, Mukes Kapilashrami, Xu Jun, O. D. Jayakumar, ***Sandeep Nagar****, Yan Wu, Cecilia Århammar, Börje Johansson, Lyubov Belova, Rajeev Ahuja, Gillian A. Gehring, and K. V. Rao, Appl. Phys. Lett.* 96 **(2010)** 232505
   My contribution: a group activity with theorists and three deposition techniques, mine is PLD approach to establish ferromagnetism in MgO.
7. **Room temperature ferromagnetic V doped MgO nanoparticles**
   Sandeep Nagar, *O D Jayakumar, Lyubov Belova, K.V. Rao* **(submitted to review)**
   My contribution: XRD, SQUID Characterization, analyses, and initial manuscript drafting.

List of Figures

List of Tables

Chapter 1

A Journey through classical to modern trends in Magnetism, and multifunctional thin film devices

1.1 ***Magnetism: a historic perspective***

Study of magnetism finds its roots in almost all ancient civilizations. Stöhr and Siegmann, gave an excellent account of development of the field of magnetism in their book [1] on *'Magnetism from fundamentals to nanoscale dynamics'*. Magnetic compass was the first recorded use of magnetic materials by Chinese in the late 11^{th} century and by Europeans in late 12^{th} century. According to Pliny the Elder's (23-79 AD) Historia naturalis the name "magnet" came from a shepherd called Magnes who found his iron-nailed shoes or iron tipped cane stuck to ground. First direction pointers were obtained from Qin dynasty (221-206 BC) which were fabricated by balancing a piece of lodestone. These direction pointers were mainly used for feng shui or geomancy, the technique of harmonizing the forces of nature by proper alignment and placement of objects. In western literature, phenomenon of magnetism was first described by Thales of Miletus (about 634-546 BC) as attraction of iron by "lodestone" (Magnetite, Fe_2O_3). Guanzhong (died 645 BC) also mentions references to loadstone as chi shi, the "loving stone" because of its ability to attract iron. About 2,500 years of research has produced diverse applications in almost all fields of human life on earth and beyond. Most importantly the magnetic compass based navigating systems enabled explorers to reach distant parts of the worlds, which ultimately unified humanity.

The first scholarly work on magnetism was performed by French scholar Pierre Pèlerin de Maricourt in 1269 who gave information about the facts known about loadstone and wrote about art of magnetic instrument making. William Gilbert (1540-1603) published his treatise De Magnete in 1600, which extensively described earth's magnetic field characteristics. Most important of the description was the fact that geographic north does not coincide with magnetic pole and hence describing the earth's axis of rotation. Earth's magnetic field was studied in detailed manner by Carl Friedrich Gauss (1777-1855) who we honor now by assigning "gauss" as a unit of magnetic field. As the field of Electricity and magnetism gained rapid strides, some

more discoveries led up to their unification. Hans Christian Ørsted was the first one to demonstrate that current carrying conductor can produce magnetic field in 1819. Jean-Baptiste Bio (1774-1862) and Felix Savart (1791-1841) derived magnetic field around a current carrying wire and André Marie Ampere (1775-1836) described forces between such wires. Work of these four men of science, paved the way to numerous discoveries in electromagnetism.

Michael Faraday discovered electromagnetic induction in 1831 and magneto-optical Faraday-effect in 1845 which ultimately connected the fields of magnetism and light. James Clark Maxwell (1831-1879) gave a mathematical structure to Faraday's ideas and developed theory of electromagnetism. Using Maxwell's theory, Heinrich Hertz, Nicolai Tesla and J.C. Bose developed radio waves in late 1880s. Investigating the atomic origins of magnetism, Pieter Zeeman, in 1896 found splitting of atomic spectra in the presence of magnetic field. Independent discovery of electron by Joseph John Thomson and Emil Wiechert in 1897, became the defining moment because now electron could be ascribed to have an intrinsic magnetic moment due to spin and hence Zeeman effect could be explained. Pierre Weiss, in 1907, introduced theory of ferromagnetism based on molecular field concept. His theory along with that of Paul Langevin (1872-1946) explained Curie temperatures quite accurately. In 1913 Neils Bohr postulated angular momentum of electrons being quantized and that orbital magnetic moment is related to orbital electrical currents. Soon Otto Stern and Walter Gerlach observed splitting of beam of Ag atoms in non-uniform magnetic field which became the basis of the concept of spin which was properly theorized by Wolgang Pauli (in 1925) and his successive investigators.

Development of quantum mechanics by Werner Heisenberg and Erwin Schrödinger in late 1920s, fermented the ideas of spin as the basis of magnetism. Dirac's work on QED (quantum electrodynamics) and its refinement by Sin-Itiro Tomonaga, Julian Schwinger and Richard P. Feynman established the fact that charged particles interact by emitting and absorbing photons, so that photons can be safely described as carriers of electromagnetic force. Heisenberg's formulation of spin-dependent model for exchange interactions refined Weiss molecular field theory by linking its origin to exchange interactions. Louis Néel developed concept of anti-ferromagnetism which was experimentally verified by neutron diffraction by Clifford G. Schull. In mid 1930s, Neville F. Mott, John C. Slater and Edmund C. Stoner applied band theory to magnetic systems which explained the non-integer values of magnetic moments.

Discovery of electromagnetism relieved humanity from the need to use magnetic materials to produce magnetic fields. Electromagnets shaped by course of industrial revolution in the form of electric motors, generators and transformers, from early 19^{th} century onwards and they are still considered one of the most useful components in machines. Discovery of high energy product permanent magnets drove the miniaturization trend of devices like electric motors and audio speakers. Post world war era started the race towards information technology driven devices where electromagnetism played a central role. Magnetic materials especially the data storage and computer memory devices became so important that it was widely accepted that whoever dominates the field of magnetism, can control the world order in cold-war driven society. As early as 1888 magnetic recording was proposed by Oberlin Smith that was used by Valdemar Poulsen in 1894 to patent Telegraphone [2]. Next major breakthrough came in 1949 when An Wang created a device based on small ferrite rings, called "cores", which could be switched by current flow through the wires that penetrate them. This invention matured into magnetic core memory for computer devices in 1950s until 1970s when semiconductor memories were invented. Thin film based memory devices like MRAM are the key to computer industry now. Past 30 years have seen an unusually fast evolution of the field of "spintronics" (using the spin and charge of electron for data storage and computation) which is now considered to be next-generation electronics.

1.2 Multifunctional Magnetic Thin films: Demands and challenges

Fabrication of whole electronic circuit on a single wafer of Si has revolutionized the way electronic devices are produced. Bulky electronic circuits gave way to lighter and compact ones and thus propelled a race towards miniaturization. Thin film based technologies were the key to this drive for miniaturization. Fabrication of good quality thin films is still a challenging area for various applications. Quality of a thin film is measured in accordance to its application. For most of the applications the level of impurities, surface roughness, epitaxial growth, amount of defects, crystallography etc. for the basic concerns for researchers.

Since magnets form the core of our modern industrial revolution (particularly post World War II era), it was natural to attempt fabrication of magnetic thin films. The rapid development of magnetic recording technology can be cited as an example of great success of industrial application of magnetism. 50 billion dollars per year magnetic storage industry provides the

backbone for monetary support for magnetic thin films research and applications efforts. These magnetic structures are not the bulk materials of past, but engineered thin films at atomic scale, where one or more dimensions fall within few nanometers. Sandwiched magnetic sensors ("read heads") such as spin valves and single/multilayered ferromagnetism thin film acting as magnetic media which can store information in nano-sized bits, are the key components of magnetism based computer technology. The growth of this technology is due to development in three key areas:

1. The development of new materials
2. Development of new experimental techniques
3. Subsequent development in theoretical understanding of new phenomenon generated by (1) and (2)

The development of new materials requires them to possess detectable equilibrium magnetization, a preferred magnetization direction (anisotropy) and well defined coercivity at room temperature. Development of new experimental techniques concerns the techniques involving fabrication, detection and manipulation of magnetization in a desired fashion. Many new phenomenon come into picture when above experimental efforts are put into practice and these new ideas are then explained using new theories which refine our understanding for behavior of magnets in various conditions.

One such new branch of study called "spintronics" was derived out of quest for understanding of electronic and magnetic properties of electron. Amalgamation of magnetism and electricity has been the core issue for physicist from the onset of electromagnetic theory. Since an electron carries a quantum mechanical spin, so it carries an intrinsic magnetic moment. Hence during electron transport, spin of electron can also be utilized to control the transport properties. Thus we can fuse together the seemingly different areas of electronics and spin-based magnetism which gave rise to a new branch of physics called "spintronics" (or ***spin electronics***). But we must remember that spin is a quantum property and hence classical computing will have to give way to quantum computing if spintronics based computing devise comes into picture. Important difference between classical and quantum computing (Table: 1.1) was highlighted by Williams [3]

Assumption	Classically	Quantum mechanically
A bit always has a definite value	True	False. A bit need not have a definite value until the moment after it is read
A bit can only be 0 or 1	True	False. A bit can be in a superposition of 0 and 1 simultaneously
A bit can be copied without affecting its value	True	False. A qubit in an unknown state cannot be copied without necessarily changing its quantum state
A bit can be read without affecting its value	True	False. Reading a qubit that is initially in a superposition will change the qubit
Reading one bit in the computer memory has no effect on any other (unread) bit in the memory	True	False. If the bit being read is entangled with another qubit, reading one qubit will affect the other
To compute the result of a computation, you must run the computer	True	False

Table: 1.1 *Difference between classical and quantum computing*

It is important to mention that any discrete two-state system (plane of polarization of a linearly polarized photon, the direction of rotation of a circularly polarized photon, or the discrete energy levels in an excited atom) qualifies for quantum computing. Spin based computing architecture is just one of these ways to construct quantum computing devise. So in general, whenever magnetic field is used as excitation and/or sensing source and electrons are used as manipulable entities, we term that area of technology as "spintronics"

This idea has already claimed Nobel prize in 2007 (Albert Fert and Peter Grünberg) and we already use devises making use of Giant magneto-resistance (GMR) effect, in our iPods and computers. Finding and subsequent successful application of GMR effect ignited a race for research in spintronics at an unprecedented pace. GMR effect simply demonstrates the importance of considering the effect of magnetic field to the flow of electrons as spin can contribute significantly to the scattering mechanism (and hence effective resistance) of electron in a lattice when the experimental structures are constructed in nanometer dimensions.

1.3 Magnetic thin films for NEMS/MEMS applications

A vibrant area of development of new magnetic thin film materials is Nano/Micro Electro

Mechanical Systems (NEMS/MEMS). These are devises integrating the functional properties of electrical and mechanical nature at micron and nanometer orders. MEMS devises generally range in size from few micrometers to a millimeter. Fabrication and integration of transistors, diodes and transformers with mechanical actuators, pumps and motors at these scales of length, enable ultra-small physical, biological and chemical sensors. The major advantages of such devices is low mass, high mechanical resonance frequencies (hence larges operation windows) and high surface to volume ratio for better surface based detection mechanisms. Apart from this, a single chip can possess sensors, processing unit and output unit which essentially makes it a fully functional unit on a single chip, which is sometimes referred to as "lab on a chip". Towards NEMS applications, an IBM team [8, 9] successfully demonstrated very large scale integration (VLSI) NEMS device using an array of AFM (Atomic Force Microscope) tips for form a memory storage device. In 2007, the International Technical Roadmap for Semiconductors (ITRS) contains NEMS memory as a new entry for the emerging research division section. Hence fabrication of new magnetic thin film materials for NEMS/MEMS applications has found its significance in future technologies. Basic process for these systems encompasses following steps:

1. Deposition
    - Deposition of uniform high quality magnetic thin film material with desired dimensions
2. Patterning
    - Transfer of a physical pattern from source to deposited thin films is usually termed as patterning. This can be done using photosensitive, magneto-sensitive, electro-magneto-sensitive techniques and/or ion beam lithography techniques.
3. Etching
    - Etching refers to the removal of undesired materials from the pattern. This can be done using chemicals (wet etching) or using sputtering or reactive vapors/ions).

In general fabrication of NEMS/MEMS uses two complementary approaches i.,e top-down approach requires optical/electrical/X-ray lithography techniques to carve out nanometer

dimension architectures in a magnetic media, which itself can be within nanometer regime. This method is limited by many factors. Wavelength of lithography beam (Rayleigh's criterion) and fabrication of lens systems with larger numerical apertures at smaller length scales, limits the size of smallest structure which can be created. Crystallinity and grain boundaries in crystalline structures limit the sharpness of the edges for the devise and hence limit the overall size of the devise. In contrast, bottom-up approach using self-organizing and positional assembly of nanometer dimensional magnetic structures. Limitations of this method rely on the magnetic and other forces (Van der Waal, electrostatic, surface effects etc.) which play important role in nanometer dimensions. Fabrication technique first depends upon the choice of one of these approaches and then upon the desired material in question.

Chapter 3 of present thesis presents a study of one such material: FePtB which can be used for permanent magnet fabrication in MEMS/NEMS devices. Different parameters like effect of temperature and choice of substrate is outlined in this study. The deposition is compared with results from previous experiments with sputtering system. It's particularly interesting to observe that thin film grows differently in the two cases and hence has different physical properties. This experiment outlines the fact that each deposition technique needs to be optimized separately to obtain the same quality of physical properties. In our experiment we found out that due to different growth mechanisms involved in PLD and sputtering, thin film grows differently under same deposition conditions of temperature and choice of substrate. This is due to the fact that PLD involves plasma species which are considerably different in their charge density, charge, Kinetic energy profile. This is mainly because sputtering generates plasma species by momentum transfer process whereas PLD involves transfer of optical energy to the system for ejection of surface materials from the target. Chapter 2 outlines the physical process involved in PLD. Experiments with FePtB thin films fabricated by PLD gives a very clear viewpoint about how PLD is different than sputtering and also outlines some distinct advantages of PLD over sputtering deposition of material.

1.4 Multi-ferroic oxide thin films

Adding one more functionality to existing magnetic materials makes it multi-functional and hence increases the use of its scope. For these applications, one needs multiferroic materials which are actuated by one more physical field apart from magnetic field. Multiferroic materials which are both ferroelectric and ferromagnetic, find their applications in computer memories. Fujitsu Inc. already supplies [4] ferroelectric Random Access Memory (FeRAM) as a non-volatile high-speed writing, low power consumption and long rewriting endurance devise. If ferroelectric layers has an added functionality of being magnetic, single ferroelectric cell can be addressed by both magnetic and electric fields and this widens the scope and reliability of applications. For these multi-functional applications, such materials are needed which are both ferroelectric and ferromagnetic i.e. materials which have atleast one magnetic ions in its composition [5]. Only a small league of materials qualify for this category due to contra-indication between conventional mechanism for cation off-centering in ferroelectrics (this requires empty d-shells) and the formation of magnetic moments (this requires partially filled d-shells) [6]. Hence if ferromagnetism and ferroelectricity has to coexist in a single phase, atom that moves off center to form an electric dipole moment must be different from those that carry magnetic moment.

Thin film form [7] of these materials is particularly important to fabricate multi-layered ferroelectric devices. Advances in thin film growth techniques have provided ways to phases (with both ferroelectric and ferromagnetic characteristics) and structures which were inaccessible by traditional chemical means.

Chapter 4 of present thesis presents a study of one such material in thin films form: $YbCrO_3$. This study resulted in an important investigation into the crosschecking of true ferroelectricity in such system and finally outlined a careful mechanism to rule out misleading measurements attributed to ferroelectricity

1.5 Amorphous magnetic thin films based on bulk metallic glass

Mechanical properties are not independent of sample dimensions and crystals start showing strong size effects at submicron scales [10, 11, 12, 13, 14, 15]. Hence crystalline structures are increasingly becoming unsuitable for NEMS fabrication technology even though

they were fine with MEMS fabrication. Advances in fabrication of glassy/amorphous materials have found this replacement in NEMS/MEMS devices because of their flexible fabrication mechanism on virtually any kind of substrate (since epitaxial growth is not an issue here) [16]. Glassy/amorphous material is characterized with a short range order of atoms. Amorphous materials possess a distinct advantage when we wish to machine structures down to atomic resolution. Lack of crystallinity makes it possible for us to fabricate sharp features down to nanometer level. Superplasticity of glassy compositions in supercooled liquid regimes is a distinct advantage while forming NEMS components with sharp features.

Nano-Imprint Lithography (NIL) employs a die (a mechanical system on which original pattern is etched) which is then imprinted on a photoresist material. Owing to their superior mechanical strength, amorphous/glassy materials can be used for making dies which are subsequently used for nano-imprint Lithography (NIL). If the glass transition temperature of such materials is sufficiently high then they can be used repeatedly without the loss of shape and size of imprints. Being chemically stable in nature, metallic glass compositions present themselves as prospective candidate in this arena. Amorphous molecular glasses are low molar-mass materials which resist crystallization on the time scales of intended usage and that form a uniform transparent thin films which lacks grain boundaries and exhibits isotropic properties. They can be used as a photoresist material for NIL [17, 18, 19, 20]. Metallic glassy structures are chemically stable and mechanically superior to traditional polymer materials which are used for lithography purposes. Particularly for magnetic NEMS applications, it is difficult to find a suitable magnetically doped polymer. Magnetic glassy compositions come very handy in these situations.

Chapter 5 of present thesis presents study of Fe based Bulk Metallic Glass (BMG) composition thin films for various applications. An extensive study of optical, magnetic and electrical properties is presented for future applications in NEMS devices and other thin film based devices.

1.6 Room temperature ferromagnetic MgO thin films: Devices to d^0 Magnetism

Presently study of d^0 magnetism is a hot topic of basic research since it opens up a new area of magnetic materials which do have empty d-shell but still show magnetic properties. Usually partially filled 3d and 4f shells are responsible for magnetism and hence magnetic materials can be segregated in the periodic table very easily. Apart from doped semiconductors and insulators (one of the magnetic ions replaces cation of parent compound), no report of magnetic material was known which had an empty d-shell but in recent years, these kind of materials are increasingly been reported.

Apart from study of traditional magnetic media, study of magnetism in new phenomenon like d^0 magnetism in semiconducting and insulating oxides also requires fabrication of high quality thin films for the same. Fabrication of materials in nanometer scales leads to predominant contribution of surface states to physical properties. These surface states are known to act as electron trap centers. Also the effect of the defects in nanometer scale structures is larger than that of bulk due to their volume fraction. These two issues contribute to the possibility of existence of magnetism even with empty valence shell. For making nanometer sized particles in powder form, various chemical techniques are employed whereas for fabricating thin films with nanometer thickness range, various deposition techniques are employed.

MgO is widely used insulating material particularly in TMR (Tunnel magneto-resistance) devices. Since many similar oxide [21] materials like CaO, HfO_2, CeO_2, Al_2O_3, ZnO, In_2O_3, TiO_2, CuO_2, SrO and SnO_2 were reported to show room temperature ferromagnetism, hence study of MgO for d^0 magnetism has become an active field amongst researchers. Underlining mechanism for room temperature ferromagnetism is hotly debated as due to cation vacancies, anion vacancies, interstitials as well as impurities in very small amounts.

Chapter 6 of present thesis presents a study of d^0 magnetism in MgO in thin films as well as powder form.

1.7 Need for high quality thin films

It should be clear from above discussions by now that applications of magnetic thin films require fabrication of few nm thick thin films. Latest report from Loth et.al [22] shows that it is possible to fabricate a magnetic storage bit with just 12 Fe atoms, which is the smallest magnetic bit till date. This provides means to fabricate multi-Terabyte per square inch storage devices. These high quality thin film work requires sophisticated deposition techniques since demands on uniformity, thickness, purity and surface quality of these thin films can be very high. Hence very sophisticated techniques such as Sputtering, Molecular Beam Epitaxy (MBE) and Pulsed LASER deposition (PLD) are used to produce high quality thin films for spintronic application.

The demands for purity, epitaxy, thickness uniformity, crystal quality and orientation require careful judgment about the method of deposition. Each method has its merits and demerits. Historically Sputtering and MBE have been used to fabricate multilayered structures for magnetic applications but slowly and steadily PLD is firming its grip in this arena because it possess many simplicities and advantages with new materials which are being explored in the area of magnetic thin films. Though MBE and sputtering can produce high quality thin film, but they are relatively complex when compared to PLD. Sputtering needs to be modified to a magnetron RF sputtering technique to be able to work with non-conducting samples (especially for spin tunneling devises which require an insulating layer) and conditions of depositions needs to be changed for each material. Complex electronics is required to maintain a steady RF power during the deposition. Deposition rate is sometimes as low as few Angstroms per minute for some materials. This makes it quite cumbersome for multilayers. MBE needs to employ raw materials, which can be easily vaporized, and sometimes new promising materials do not possess such raw materials. Proper direction of vapor onto substrates is a complex art in itself. Contamination of vapor materials of one kind over another during multi-layer deposition is an unavoidable problem. The efficiency of the whole process is also very low since a fraction of vapor produced is actually used for deposition and rest of it remains as a contaminant in the system which, then needs to be cleaned for fresh use.

PLD comes to our rescue in this case since it simple and straightforward technique where few parameters govern the quality of thin film and many of them can be easily tuned for almost any type of target materials. There is only one requirement that target should be dense. There is

no restriction on the type of substrate used since anything from soft polymers to diamond can be coated. Alloys maintain their stoichiometry during deposition which turns out to be a great advantage in the case of using doped semiconductors and insulators as spacer layers and magnets.

Chapter 2 in present thesis illustrates the use of PLD technique for depositing a variety of thin films, which find their application as magnetic thin films. Important parameters and limitations of PLD techniques are outlined and its used for subsequent depositing of composite permanent magnetic FePtB thin films, amorphous FeBNbY films suitable for nanolithography in NEMS/MEMS device development, and also for two basic studies: namely, amorphization of chromite thin films to test the multifunctional coexistence of ferromagnetism vs ferroelectricity, and d^0 ferromagnetism at room temperatures in doped and undoped MgO. The specific advantage of using PLD for these varieties of materials lays in its ability to form stoichiometric, uniform and high quality impurity free thin films with relatively easily controllable and changeable depositing parameters.

As, is noticeable from the above list, different materials require specific conditions of deposition of high quality thin films. PLD technique was chosen for advantages which will be outlined in chapter 2. Using other techniques like sputtering and MBE pose certain disadvantages like difficulty in controlling desired elemental composition, low rate of deposition and difficulty to change the deposition set up when changing from insulators to metallic compositions. PLD provides a simpler route to overcome these problems and we believe that these four studies demonstrate the robustness and versatility of this technique for its applications in spintronic industry.

1.8 ***References***

1. Magnetism from fundamentals to nanoscale Dynamics, Springer Series in Solid-State Sciences, J. Stöhr, H.C. Siegmann , ISSN 0171-1873, ISBN-10 3-540-30282 ISBN-13 978-3-540-30282 Springer Berlin Heidelberg New York, (page 1-14)
2. Magnetism from fundamentals to nanoscale Dynamics, Springer Series in Solid-State Sciences, J. Stöhr, H.C. Siegmann , ISSN 0171-1873, ISBN-10 3-540-30282 Springer Berlin Heidelberg New York, ISBN-13 978-3-540-30282 Springer Berlin Heidelberg New York (page 1-14)
3. Explorations in quantum computing, Colin P Williams, second ed. Chapter 1, page 8
4. http://www.fujitsu.com/emea/services/microelectronics/fram/
5. Sang-Wook Cheong, Maxim Mostovoy, *Nature Materials* 6 **(2007)** 13
6. Nicola A. Spadin, Manfred Fiebig, 309 *Science* **(2005)** 391-392
7. R. Ramesh, Nicola A. Spaldin, *Nature Materials* 6 **(2007)** 21
8. P. Vettiger, J. Brugger, M. Despont, U. Drechsler, U. Dürig, W. Häberle, M. Lutwyche, H. Rothuizen, R. Stutz, R. Widmer, G. Binnig, *Microelectronics Engineering* 46 **(1999)** 11-17
9. M. Despont, J. Brugger, U. Drechsler, U. Dürig, W. Häberle, M. Lutwyche, H. Rothuizen, R. Stutz, R. Widmer, G. Binnig, H. Rohrer, P. Vettiger, *Sensors and Actuators* 80 **(2000)** 100–107
10. L.V. Raulea , A.M. Goijaerts , L.E. Govaert , F.P.T. Baaijens , *J. Mater. Process. Technol.* 115 **(2001)** 44
11. G.P. Zhang , C.A. Volkert , R. Schwaiger , P. Wellner , E. Arzt , O. Kraft , *Acta Mater.* 54 **(2006)** 3127
12. N.S. Tambe , B. Bhushan , *Nanotechnology* 15 **(2004)** 1561
13. M.G.D. Geers , W.A.M. Brekelmans , P.J.M. Janssen , *Int. J. Solids Struct.* 43 **(2006)** 7304
14. J.R. Geer , W.C. Oliver , W.D. Nix , *Acta Mater.* 53 **(2005)** 1821
15. M. Klein , A. Hadrboletz , B. Weiss , G. Khatibi , *Mater. Sci. Eng. A* 319 – 321 **(2001)** 924

16. V. Lindroos , Handbook of Silicon based MEMS Materials and Technologies, Elsevier publication **(2010)** chapter 27, Page 447
17. D. Yang , S.W. Chang , C.K. Ober , *J. Mater. Chem.* 16 **(2006)** 1693
18. D. Bratton , D. Yang , J. Dai , C.K. Ober , *Polym. Adv. Technol.* 17 **(2006)** 94
19. N.M. Felix , K. Tsuchiya , C.K. Ober , *Adv. Mater.* 18 **(2006)** 442
20. S.W. Chang , R. Ayothi , D. Bratton , D. Yang , N. Felix , H.B. Cao , H. Deng , C.K. Ober , *J. Mater. Chem.* 16 **(2006)** 1470
21. Kesong Yang, Rongqin Wu, Lei Shen, Yuan Ping Feng,Ying Dai, and Baibiao Huang, *Phys. Rev. B* 81 **(2010)**125211
22. Sebastian Loth, Susanne Baumann, Christopher P. Lutz, D. M. Eigler, Andreas J. Heinrich, *Science*, 335**(2012)** 196

Chapter 2

Pulsed LASER Thin film deposition

2.1 Introduction

With the advent of microelectronics, chip fabricators started investigating various methods to develop high quality thin films for various device applications. Quality of thin film is judged by application of the material involved. But in general impurity free, epitaxial and stoichiometric thin films deposition with good control over thickness and higher deposition rate has been the main focus of researchers involved in development of new deposition techniques. Deposition techniques like sputtering, Chemical Vapor Deposition (CVD), Metal Organic CVD (MOCVD), thermal evaporation are widely used for fabricating thin films.

PLD is one of these thin film growth technique. Here photonic energy is transferred to bulk material via electronic process, which in turn is used up to ablate few surface layers as plasma and this plasma is then deposited onto a desired substrate under suitable conditions. Since high intensity pulsed beam (width of beams ranges from ns to fs) of LASER is focused on a very small area (few mm), non-equilibrium process of plasma generation allows great degree of freedom to change various parameters to fabricate desired high quality thin films. Due to pulsed nature of the process, it offers an easier alternative to otherwise complex ways to control the thickness and quality of thin films precisely.

After the invention of LASER in 1960s, they were predominantly used for selective heating with high lateral and depth resolution rather than ablation of material. Serious attempts towards ablation of solid target materials using LASER beams started in mid 1980s [1, 2,3] and it turned out to be an efficient way to fabricate complex thin film structures with relatively simpler procedures on a variety of substrate-target combinations.

2.2 Various thin films deposition techniques

Sputtering technique requires target material to be conductive. **Radio-frequency (RF) sputtering** is used for semiconducting and insulating samples. Magnets are used in sputtering system to direct plasma towards a particular area and also for increasing the efficiency of discharge which makes plasma. **Thermal evaporation** techniques simply heats up the target material to decompose it into vapor which is then cooled down on a desired substrate surface.

Chemical vapor deposition mixes various vapors of elements/compounds on a desired substrate surface. To avoid inorganic impurities, which are difficult to avoid sometimes during CVD process, organometallic compounds are used as precursor materials to produce desired vapors for mixing and this process is termed **MOCVD** accordingly. **The sol-gel technique** is a chemical procedure where a particular chemical mixture forms a gel-like diphasic liquid and solid phases and phase separation techniques are used to obtain desired solid phase onto a substrate surface by spin coating or so.

In general, these techniques use decomposition of target materials with the aid of electrical and/or thermal energy and thus generating the precursor material in gas or plasma form, which is then cooled down on a substrate surface and develops crystallographic properties according to the thermodynamic conditions involved in the process. In general, all of these methods use equilibrium thermodynamic systems during deposition process.

When a system is driven in a **non-equilibrium** state, there is a greater flexibility to change the parameters and drive the system in a particular thermodynamic direction. When a system is driven out of thermal equilibrium to perform physical and chemical processes such as breaking and making of chemical bonds by ensemble species, Maxwell-Boltzmann energy distribution equations cannot account for the system i.e. a single temperature cannot account for the process (hence the name : non-thermal interactions). Hence each component of a system can be addressed independent of each other. This gives tremendous flexibility in tuning composition and crystallization process.

2.3 PLD as a non-equilibrium process [4]:

Thermal deposition techniques are defined as those in which kinetic energies of impinging particles are of the order of 0.1 eV. In the case of non-thermal interactions, energy can be guided selectively and non-thermally pumped (ex. Laser light or electric field) into one degree of freedom that is effectively decoupled from rest of the system (molecular or atomic). In this way, activation barrier for the reaction is alterable and preferably lowered by non-thermal manipulation of electron energy distribution (electrons have negligible thermal mass). The major advantage of this method is that reduction of activation barrier can be done while maintaining the whole system (which carries rest of the thermal mass) at a low temperature. In these cases,

process chamber remains are lower temperatures whereas temperature of electrons may be many thousands of degrees Kelvin. In PLD, Ion and electron temperatures are of the order of several thousand Kelvin and also plasma has high degree of ionization while the deposition chamber remains at almost room temperature during the entire operation.

2.4 Working mechanism of PLD process

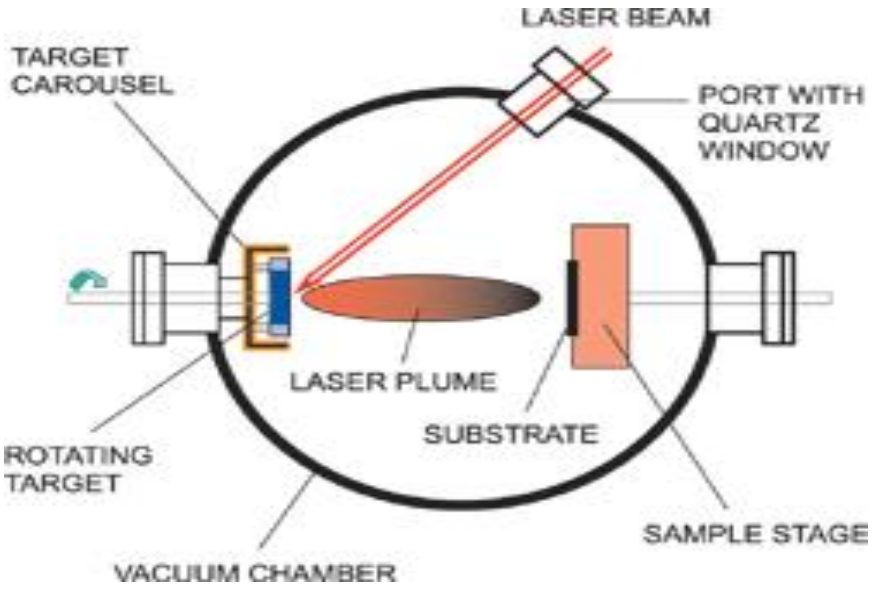

Fig: 2.1: *Schematic diagram of PLD system*

As shown in Fig: 2.1, an intense LASER pulse is focused onto a target material placed inside a vacuum chamber, where it is partially absorbed. Above a threshold power density (depends on target material but it's usually of the order of 10-500 $MWcm^{-2}$ laser pulses of few ns duration for UV wavelengths), materials ejects out as luminous plasma (luminosity comes from excited species de-exciting to lower energy states or neutrals). Vacuum chamber can be filled with a controlled atmosphere of gas to enable chemical reactions to make desired stoichiometry (this is termed as "reactive PLD" technique). Plasma material re-condenses on the substrate to proceed for film growth via crystallization process. Since plasma species consist of highly energetic particles, hence the landing species have enough energy to overcome adhesive forces and epitaxial barriers. Thus they self-assemble themselves into least energy expensive crystallographic orientation.

Mechanism of PLD involves complex interplay of many variables such as:

1. LASER wavelength
2. Pulse duration
3. Power density delivered to target
4. Pressure of background reactive gas
5. Shape and size of LASER beam spot on target
6. Distance between target and substrate
7. Temperature of substrate during deposition
8. Relative orientation of target and substrate holder assembly

In the rest of this description the effects of these variables during a deposition process is discussed in detail.

2.5 Discussion about various parameters

There are various LASERs available with a wide range of wavelength including pulsed and continuous wave ones. Pulsed LASERs are preferred for material deposition owing to their high power output and pulse nature which provides digital control over deposition process. Ablation performance is governed by a variety of LASER beam and material parameters. LASER beam parameters include wavelength, pulse frequency, energy fluence, spot size etc. The material parameters include reflectance, absorption coefficient, specific heat, thermal conductivity, latent heat etc. Quality of thin film is affected by parameters which include substrate temperature, ambient gas pressure of chamber, substrate-target distance and deposition geometry. Industrial applications demands higher deposition rates, which can be achieved by fine tuning each parameters for best quality thin film. Shape and size of spot determines the power density delivered to the target. Well defined shape and smaller sizes of spot sizes are desired in case of material deposition.

Reactive gases are sometimes introduced to form a desired phase during material deposition. Use of inert gases like Ar is also useful when high levels of purity are desired for a particular application. Use of good vacuum conditions followed by Ar gas flushing of vacuum for a few times ensures an impurity free environment for material deposition.

Distance between target and substrate is determined by kinetic energy of plasma species which reach substrate. The effect of varying this distance is reflected in crystallinity and surface roughness of the thin film as landing species with sufficient kinetic self-assemble on the surface while excessive kinetic energy of landing species sputter out the depositing material.

Crystallinity and phase generation in deposited thin films also depends on the temperature of substrates. Higher temperatures change the surface conditions of substrate to assist or degrade (as per choice of material-substrate choice) crystallinity of thin film. Temperature of substrate can be used by landing plasma species to overcome activation barrier to form new phases too.

Relative orientation of substrate and target holder assembly results in different qualities of thin films as landing plasma species arrive at an angle to the substrate and thus adhesive forces can be tuned to our advantage. This method can also be used to our advantages to reduce the number of droplets on the surface (discussed at later sections).

2.6 Stoichiometric transfer

One of the most important features of PLD is its ability to realize stoichiometric transfer of ablated material from target to substrate surface. This arises from the non-equilibrium nature of ablation process involved since very high energy density is absorbed by very small volume of target material. Evaporative flux from a multicomponent target chiefly depends on the vapor pressure of its constituents. At lower fluence (low energy density per unit area of target material) ablation threshold for some constituents may be crossed so that they form the plasma but higher fluence result in vaporization which does not depend on vapor pressure of constituents and hence plasma plume consists of species of all constituents in exact proportion as that of target material. Many reports [5, 6] demonstrated how fluence affects the stoichiometric transfer of target material but there are other parameters like background gas, surface roughness of target and physical properties (optical, mechanical and thermal) target material itself, which govern the ejection of stoichiometric volume of material on contact with LASER pulse. This phenomenon is discussed in more details below.

But it is important to note that there exists a widely tuned set of conditions when stoichiometry transfer is possible [7]. First indications towards this aspect was highlighted by

Venketesan et.al [2] when it was reported that laser ablation of $Y_1Ba_2C_3O_{7-x}$ target results in simultaneous formation of stoichiometric ablated material and non-stoichiometric evaporated material during the same run. A detailed review of many aspects of non-stoichiometric composition has been discussed by Schou [7] and following recommendations were made to avoid deviations from stoichiometry:

- **LASER fluence**:
    - Avoid too low fluence since evaporation dominates ablation in this regime and evaporation does not follow stoichiometric transfer.
    - Avoid too high fluence since it leads to (re)sputtering of thin films on substrate by plasma species.
    - To fine tune the fluence of ablated particles, background gas should be used as moderator.
- **Background gas pressure**:
    - Avoid too high pressure because it leads to preferential diffusion of light atoms in the gas
    - Stopping distance of plume (which depends directly on choice of background gas) should govern the choice of target to substrate distance. Substrate should be placed outside the stopping distance of plume to avoid (re)sputtering of thin films by plasma species.
    - If the plasma species include volatile components, like oxygen for oxides and nitrogen for nitrides, background gas amount should be fine-tuned to compensate for the lack of stoichiometry.

2.7 A brief review of Ablation process and thin film generation

2.7.1 Light interaction with target

Absorption of light by target surface and subsequent excitation of target materials is vital process to understand the plasma generation. When light is absorbed by the surface of the target, the electromagnetic energy is transformed into electronic excitation in various forms like plasmons, unbound electrons and excitons in the case of insulators. Dielectric function of the materials plays a crucial role in this process.

The Electric field amplitude E of an electromagnetic wave is given by [4]:

$$E = \left(\frac{2\phi}{cn\varepsilon_0}\right)^{1/2}$$

Where φ is power density, ε_0 is the permittivity of free space, c is the velocity of light and n is the refractive index. An incident radiation of power density 2 x 10^8 Wcm^{-2} on a material of refractive index 2 will be subjected to field strength of 2 x 10^5 Vcm^{-1}. This is sufficient to cause breakdown and hence ionization in most of the materials which results in plasma formation. Threshold electric field strength for dielectric breakdown is proportional to the square root of the power density which is proportional to laser fluence and inversely to laser pulse duration. But this scenario also encompasses an important aspect of thermal conduction through the lattice, which cannot be avoided.

According to Fick's law, thermal diffusion length of a solid is given by [8]:

$$l_T = 2\sqrt{D_T \tau_l}$$

Where τ_l is LASER pulse duration (few ns) and D_T is thermal diffusitivity.. $l_T \propto \sqrt{\tau_l}$.

Hence τ >20s results in ablation via conventional heat deposition.

The optically excited electrons transfer energy to lattice within few picoseconds which results in heating of material in the optical absorption depth given by 1/α where α is the optical absorption coefficient. If the thermal diffusion length is $l_T < 1/\alpha$, the bulk will be heated down to 1/α independent of pulse duration. This scenario is important in the case of multi-elemental target where one desires congruent evaporation. Hence the use of fast UV source is favored. When $l_T \gg 1/\alpha$ (in the case of using femtosecond LASER), absorption layer receives the photonic energy and thermally transport it to the depth of l_T.

For metals, l_T is of the order of 1μm. This 1 micron sized area of material experiences a unique phenomenon known as laser supported absorption. Time required for the surface to reach its boiling temperature is square of absorbed laser density. For LASER intensity 10^8-10^9 $W.m^{-2}$, this time is of the order of 0.1-1ns. The first pulse produces a partially thermally ionized plasma layer on the surface and subsequent LASER energy is spent on superheating the plasma layer. Hence LASER mostly impinges on liquid, gaseous or plasma phase of the material. In this way,

only a small portion of target material is ablated but this volume of material is highly thermally excited. This is called Laser Supported Ablation. Subsequent plasma's K.E. profile is a result of out-of-surface explosion caused by LSA mechanism which produces high pressure and high temperature conditions. This scenario changes the effective thermal diffusion length to $l_T^{eff} = 2\sqrt{D\tau_{eff}}$ where τ_{eff} is the time needed to create an erosion plasma after the first pulse.

The magnitude of ablation yield depends on the cohesive energy i.e. the energy required to release an atom from a solid. Typically yield lies in the range of 10^{15} atoms/pulse [9] which shows that many layers of material is ablated during one pulse. The characteristics of the volume of ablated material depend on the uniformity of the LASER beam. If the intensity of LASER beam spot is non-uniform then evaporation (not ablation) will take place in areas with low intensity i.e. edges and ablation in areas with high intensity i.e. center of the beam. Hence it is quite important to check for uniformity of intensity within a LASER beam spot since evaporation of material induces non-stoichiometry as well as reduction in rate of ablation.

1. Plasma plume formation and its expansion (Fig: 2.2)

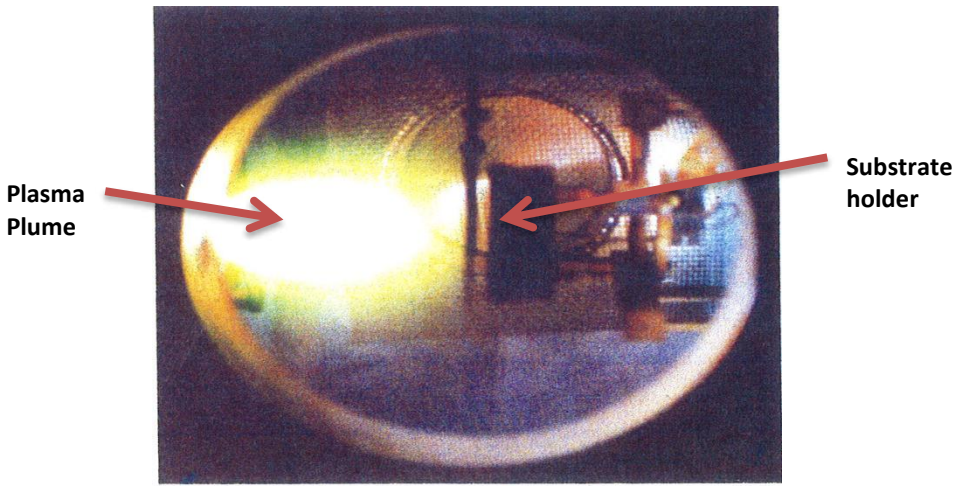

Fig. 2.2 *Plasma plume interaction with substrate surface during interaction. The luminosity of plasma plume is due to the fact that excited ions and charge species recombine or convert to neutrals results in generation of photons.*

Plasma plume propagation can be studied in two stages [7]:

- One dimensional expansion during the ns-pulse
- Three dimensional expansion

2.7.2 One dimensional expansion during ns-pulse

One dimensional expansion of plasma species involves the photo-excitation lead ionization of the all component in almost same ratio as in the target (provided energy threshold of all species is exceeded by energy of incident light pulse). After termination of light pulse, the plume front already propagates 30-100μm. High temperature induced pressure can be as high as 5-10 bars and this drives the further expansion. At a distance of 200-500 μm, kinetic energy will exceed the thermal energy of plume and will take over as a propelling source for plume into vacuum of background gas atmosphere. It is important to note that in the case of multicomponent target, if the variation of photo-excitation cross-section is too large for different components then non-stoichiometric plasma generation occurs in this step, which might ultimately induce non-stoichiometric thin film.

2.7.3 Three dimensional expansion

Now plume expands adiabatically in chamber atmosphere until pressure of the plume decreases significantly (in case of background gas, it decreases drastically). Plume is strongly peaked in forward direction due to pressure gradients during one dimensional expansion. Adiabatic expansion velocity should ideally be inversely proportional to square root of mass of constituent species [10] but it deviates from ideal result in experiments. Ion velocities for metals vary from 30 to 10 Km/s [9]. In case of background gas, plume ultimately slows down and is confined as a sphere which stops the motion on a microsecond timescale [11] creating a shockwave at the contact front between ablation plume and background gas [12]. Strikovski and Miller [13] defined a stopping distance i.e distance from target at which the thermal velocity equals the front velocity. Energetically, K.E of plume is converted into thermal energy of plume and background gas. Clearly, the stopping distance has direct correlation with atomic mass of the target. Also, range of plume becomes extremely important parameters while deciding the target to substrate distance to optimize a decent deposition rate. Angular distribution of plume entirely depends on deposition chamber atmosphere as the background gas atoms are responsible for the scattering of plasma species [9]. Choice of heavier atoms for background gas will pronounce the angular distribution. It is important to note that scattering is mass specific phenomenon and hence it introduces non-stoichiometric profile in plasma plume which might lead to non-stoichiometric thin film growth [14].

Fluid dynamic modeling explains successfully, the expansion of nascent erosion plasma [15]. Wilmott and Huber's review [4] compiled the information about the expanding plasma and its re-condensation on the substrate which eventually leads to film growth. As is the case of most PLD depositions, when the ablation yield is much above 0.1 monolayer per ns, collision-less movement of plasma particles is not possible due to higher density of particles in the plasma. Also, the degree of ionization depends on LASER parameters like wavelength, fluence, and pulse duration as well as target material. Also, degree of ionization will change as the plasma expands (and subsequently relaxes by thermally equilibrating via collisions and forming Knusden layer). Through Ion-electron recombination and electron transfer between ions and neutrals, plasma relaxes over few millimeters and become collision less. Though nascent plasma near the surface initially has temperatures of the order of 20000°K, it adiabatically cools to 3000-5000K and plasma species (ions, neutrals and molecular species) can have energies close to 1-500eV depending on material. These conditions must be taken care of while studying plasma dynamics.

There are many ways to study the plasma composition and its dynamics like optical spectroscopy, time-of-flight mass spectroscopy and time-of-flight mass quadrupole spectroscopy. Though optical spectroscopy seems to be an excellent tool since most of the charged species become neutral by emission of visible and UV photons (which gives plasma its characteristic color),it is infested with many errors due to plasma sheath distortion due to charge buildup, local electric field inhomogeneity and chemical modifications of surface.

Angular distribution of plume is approximated as $\cos^{n}(\theta)$ with n ranging from 2 to 20 depending on fluence. But this simple picture becomes complicated once we take into account shock fronts which generate plasma wings for higher intensities. J.F. Ready [16] performed one of the earliest experiments to study the generation of plasma plume. By taking high-speed photographs (frame time=10ns) of 30MW LASER pulse interaction with carbon block in air, LASER-target interaction was studied. Velocity of plasma plume was found to be about 2×10^{6}cm/s. This work reinforced the concept of sub-surface boiling of target material as the cause of production of particulates on the surface. Timm et.al. [8] Observed the exfoliation effect of target by studying target surface roughness.

2.7.4 Re-condensation of plasma on substrate surface:

Growth of thin film on a substrate is a complex phenomenon since there are virtually innumerable combinations of substrate-deposition material combination and many parameters govern their interaction. Arriving atoms/molecules/ions/charged species may stock to the surface at the point of impact itself or they can diffuse some distance on the surface (if they have enough K.E) until energetically favorable bonds have been established with substrate as well as adjacent atoms. Apart from adsorption of incoming species, reflection and sputtering of adsorbed species also occur and constantly erode the developing thin films. These phenomenon are discussed in details below.

Highly energetic charged ions and neutral specials land on substrate surface with enough Kinetic Energy (K.E) to self-assemble according to energy kinetics of the system. Energy kinetics includes adsorption energy, K.E of landing species, reactions between subsequent ions and surface properties exposed to plasma. Discussion about plasma condensation is specific for particular set of material and substrate hence it should be studied within those specificities using the parameters for energy kinetics as mentioned above. Re-condensation of plasma species can be fine-tuned by the thermal state of substrate surface. By heating or cooling the substrate surface, development of particular crystallographic phase of thin films can be achieved with relative ease.

In general, an adsorbed atom/ion on surface can:

- diffuse across the surface
- escape into vacuum
- bond as an ad-atom

Diffusion rate of ad-atoms across surface is given by:

$$D_s = D_0 \exp(\in/kT)$$

$\in$ is the activation energy for diffusion (about 2-3 eV) on an atomically flat covalent surface

Surface diffusion allows ad-atoms to move to thermodynamically stable sites to minimize their surface energy. Surface temperature catalyzes this process. But this also leads to concomitant increase in surface to bulk diffusion and bulk inter-diffusion. Hence instead of increasing the temperature, enhancing the energy transfer from species impinging from gas phase

to surface species, seems a favorable option. In this regard, PLD is a favorable technique of depositing high quality thin films.

Changing the chamber atmosphere also affects the deposited thin films characteristics. Marcu et.al [17] observed that changing the distance between substrate and target only influences the growth rate but changing the LASER energy changes the growth rate as well as growth regime from island-type growth to nanowire growth for MgO. Nanowire growth requires catalyst particles which are supplied only in the case of higher energy LASER where kinetic energy of plasma species becomes higher.

One major issue with higher fluence, employed to obtain higher deposition rates, is that of resputtering [18, 19] which changes the morphology, stoichiometry and in extreme cases, the whole growth dynamics of thin film. Hence it's important to judge the deposition parameters like fluence and background pressure to minimize resputtering.

2.8 Limitations of PLD

Two major limitations limit PLD use when compared with commercially available CVD techniques. One of them is small area of uniform deposition in a PLD chamber and second one is the problem of droplet formation on the surface of PLD deposited thin film. Now we shall discuss these limitation and ways to overcome them.

2.8.1 Large Area PLD

Because of $\cos^n$-distribution (n>1) of plasma plume, deposited thin film is non-uniform beyond few mm^2 of deposited area. Dietsch et.al. [20, 21] used a scanning dual beam LASER on a cylindrical target to deposit uniformly over a large area of 6 inch substrate diameter (Fig: 2.3).

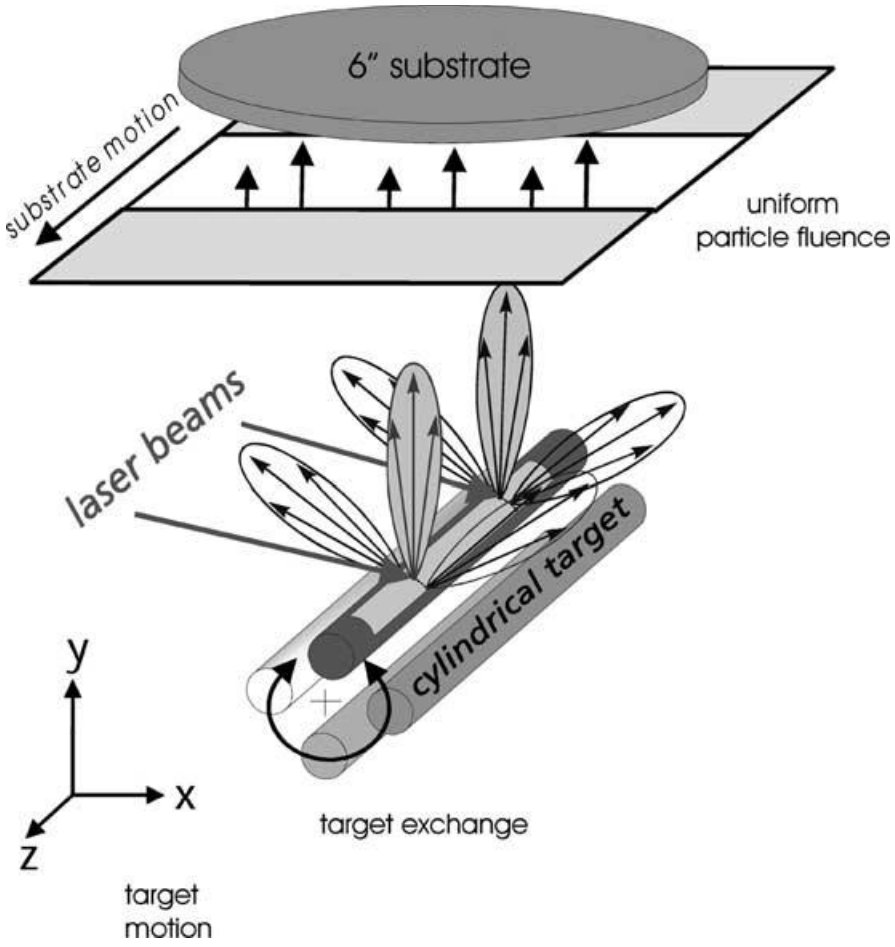

Fig: 2.3 *Schematic diagram of rotating cylindrical target arrangement for large area PLD*

Targets of lengths 165mm and diameter 20 mm were used for this purpose with target to substrate distance tunable from 150 to 250mm. This experiment effectively demonstrated that PLD systems can upscale to commercial requirements without a need of complex arrangements.

2.8.2 Macroscopic particulate production

Thin films developed using Pulsed LASER deposition technique presents good quality stoichiometry and roughness control, but it also comes with a disadvantageous feature of producing droplets on the surface. These droplets present a problem in multi-layer depositions, especially when layers are confined to nanometer regime. Various methods have been explored to avoid droplets on the surface but none of them have been successful to obtain a 100% droplet free surface, though number of droplets can be reduced to great extent so that considerable droplet free area can be fabricated for device fabrication. To reduce the number density of droplets, we will first study their origin and then explore various methods proposed in literature.

Interaction of a high intensity LASER pulse with a target has been studied and simulated, to study the formation of droplets on thin film surface. When a high intensity LASER pulse hits the target surface, the mechanical forces due to thermal induced shock wave in a target, can lead to the ejection of macroscopic particulates. Nascent plasma when in contact with the target surface can induce forces of up to 10^4 N during irradiation. These macroscopic particulates are generally labeled as "laser droplets". Droplets are usually smoothly round in shape which indicates that they were probably molten before hitting the substrate surface.

Droplets are observed with a smooth spherical shape which suggests that they originate from a large chunk of molten material which solidifies on its way towards the substrate. Since aggregation and condensation at film surface does not necessarily produce a spherical shape, hence droplets definitely originate from the molten chunk of material from the target. Fähler et.al. [22] observed micron and submicron seized droplets for stainless steel target and similar results have been observed by us in our experiments too. They have following features:

- **Micron sized**
    - Non-uniform distribution
    - Peaked in direction of incoming plume
    - Usually observed only with rough target surface
    - Number density show a minima at 8J/cm^2 after which it remains constant.
    - Average velocity ~20m/s
- **Submicron sized**
    - Homogeneous distribution
    - Present even with a smooth target
    - Number density shows a minima at 8J/cm^2 after which it increases again.
    - Average velocity~50m/s and maximum velocity~150m/s.

Difference in number density behavior indicates different origins of these two kinds of droplets. Bigger droplets are caused by erosion of large chunks of target material due to thermal induced shock wave (which eventually makes target rough). When eventually target smoothens out, these droplets vanish. If the target is well polished and smooth, the big droplets can be

avoided. Smaller droplets originate due to "sub-surface heating" [23,24]. Absorbed light heats up certain depth of the target. Surface of this area cools down due to latent heat of evaporation. This leads to bubbling and hence formation of droplets. This phenomenon is directly proportional to energy density of LASER light and inversely proportional to absorption coefficient of target material. Another proposed origin of these droplets is the "hydrodynamic sputtering" [25]. Due to continuous thermal shock, surface develops cracks and material at surface sputters away in the form of tiny droplets. More detailed discussion on this topic is presented in following sub-section.

2.8.2.1 Origin of droplets

A detailed discussion about the origin of droplets is presented in this section since the study of original and various techniques to remove these droplets elaborates the basic working mechanism and its possible alterations to our advantage. In this sense, this section essentially supplies the practical knowledge about the ablation process and how this process can be altered to get desired quality of thin films. It also elaborates the limitation of alteration which is essential to know when one has to plan industrial grade PLD systems. Three different phenomena are responsible for their origin [4], which are discussed below.

2.8.2.1.1 Subsurface boiling

When time needed to convert laser energy into heat and transfer it into the bulk, is shorter than the time needed to evaporate the surface layer, the surface boiling phenomenon occurs. The thickness of surface layer affected by LASER pulse is defines as skin depth δ [16]:

$$\delta = \sqrt{\frac{2}{\mu_0 \sigma \omega}}$$

Where μ_0 is permittivity of free space, σ is electrical conductivity of target material and ω is the angular frequency of incoming LASER light. Target material layers, defined by the thickness of skin depth, reaches its vaporization temperature before the surface has absorbed its latent heat of vaporization. This results in a thermal explosion due to a pulse of high pressure produced by super-heating of underlying material resulting in formation of a highly condensed gas. Due to low σ, subsurface boiling is negligible for high dielectric material but it is very dominant in low dielectric materials.

2.8.2.1.2 Recoil ejection

If the density of target material is low, due to mechanical stress produced by thermal induced shockwave, target surface material can recoil eject to form droplets. This can be effectively controlled by choosing high density targets.

2.8.2.1.3 Exfoliation

Due to surface erosion and repeated melt-freeze cycles of the target material, roughness of target surface increases. Eventually mechanical outgrowths are thermally decoupled (exfoliation). Timm et.al. [8] observed the effect of target roughness on droplet formation and suggest steps to avoid this effect. Metallic targets are recommended to be polished very carefully to give them a mirror-like finish.

The first two of these are termed ‘‘splashing’’ phenomena and, to a first approximation, are independent of the target morphology and can produce droplets from a single laser shot. Thus production of macroscopic droplets cannot be avoided but various measures are suggested to effectively reduce their number density for devise fabrication work.

2.8.2.2 Effect of wavelength

Effect of wavelength can be understood in present context as wavelength and the absorption coefficient of the material, determines the amount of energy used up in heating. Koren et.al [26] found that using shorter UV wavelengths for $Y_1B_2Cu_3O_{7-\delta}$ resulted in reduction of droplets on the surface of the thin film. Tcheliebou and Baik [27] found similar result for $Ba_{0.5}Sr_{0.5}TiO_3$ films.

2.8.2.3 Number and Size distribution:

Szörenyi et.al.[28] studied the number and size distribution of droplets and found that:

- Area of the film covered by droplets monotonously increases with the energy density.
- Number of submicron droplets is one order of magnitude less than number of bigger than 1 micron diameter droplets.

2.8.2.4 Effect of droplets on Physical properties:

Droplets have not affected optical properties of $(Fe_{72}B_{24}Nb_4)_{95.5}Y_{4.5}$ glassy thin films I have prepared. We measured transmittance and reflectance spectra of thin films in wide-angle mode where these properties are measured when scattering of light is a dominant phenomenon. Surface droplets can be a major cause of scattering of light. We found that scattering was

responsible for $\sim 3-4\%$ of total transmitted and reflected signal, which indicates that droplets do not cover majority of surface area and hence do not significantly alter the optical transmittance and reflectance of thin films under study. Misra et.al also reported that droplets do not affect the superconducting properties of $Y_1Ba_2Cu_3O_{7-8}$[29]. Even though droplets do not affect the physical properties considerably, they present a major stumbling block in developing multi-layered thin film structures for device applications and hence needs to be addressed surely.

2.8.2.5 Recommended steps to be taken to reduce the number of droplets:

In view of the above previously mentioned arguments about production of droplets, following steps are recommended to reduce the number of droplets.

- Energy density should only be slightly above the evaporation threshold.
    - Absorption coefficient of the target material should be known for the wavelength of LASER used. Using this absorption coefficient, energy absorbed per pulse can be calculated for a particular volume of target. This energy density should be just enough to evaporate the target.
- Target surface should be smooth. It is recommended to smoothen target surface after each deposition.
- Target should be as dense as possible. A dense target can avoid undue exfoliation of target material from the surface on LASER impact.

2.8.2.6 Various methods to decrease/remove droplets from thin film surface:

After taking care of before mentioned steps to reduce the number of droplets, they do appear on thin film surface. Multilayered thin film depositions require droplet free smooth surface and hence removal of droplets from PLD thin film surfaces has been attempted by many researchers in past. Some of the techniques which have been employed for the same are as follows:

2.8.2.6.1 Eclipse PLD[30]

High energy particles of the plasma plume are obstructed physically to reach the substrate by employing line-of-sight shadow techniques. This method has two distinct disadvantages namely (i) the obstruction material may sputter out impurities which might reach the substrate resulting in impurities in thin film and (ii) stoichiometry of plasma plume is disturbed [31].

2.8.2.6.2 Aperture plate [32]

Plasma plume is made to pass through an aperture which regulated the forward direction movement of big particulates. Again this method pose the same disadvantage as that of eclipsing the plasma as obstruction material may sputter out impurities which might reach the substrate resulting in impurities in thin film.

2.8.2.6.3 Rotating vane velocity filters [33]:

Instead of a stationary obstruction, plasma plume passes through a rotating vane velocity filter which rotates close to velocity of macroscopic particulates and hence filters out plasma particles of a certain range of velocity and thus can be used to obstruct high energy particles which are responsible for droplet formation.

2.8.2.6.4 Double slit [34]:

A double slit is used as an obstruction to the plasma plume path to trap the droplets before reaching the substrate Crossing the two slits with respect to each other (each having slits of 1mm each) can effectively prevent micron size droplets from reaching the substrates.

Off-axis deposition

Holzapfel et.al [35] demonstrated reduction of particulates without using an obstruction to plasma plume. Substrate is kept parallel to the direction of ejected particles. This method has an additional advantage that deposition can be performed on both sides of the substrate. It was reported that this method effectively reduces the number density of the particles at the cost of a severe drop in deposition rate. Kennedy [36] used this technique for producing single and multilayers of superconducting materials. Deposition rate was reported to drop by a factor of 3 but produced smooth crystalline thin films. Zemsky et.al [37] showed similar results for B_4C deposition and noted that in the case of columnar growth of material, shadowing effect plays a crucial role in film growth. Columns were found to tilt towards the incident flux. Lee. et.al [38] also demonstrated reduction of large droplets for $YBa_2Cu_3O_7$ thin films and highlighted a new problem of off-stoichiometric growth from deposited species due to local inhomogeneous mixing of ablated species.

2.8.2.6.5 Cross Fluxes Technique:

Cross fluxes techniques are techniques where one or more plasma plumes are crossed in their path to scatter the bigger particles. Cracium [39] proposed a simpler version of this method

which does not required more than one LASER beam using concave shaped Target. The rectangular laser beam was focused exactly at the tip of the concave shaped target. Each part of the laser spot created two symmetrical plasma plumes on each side of the concave target and interacted in the region of target axis. Similar to the previous attempts of Cross flux technique using two LASER beams [40], the heavy droplets will pass through the interaction region without colliding with other droplets, maintain their velocity direction and move away from the system axis. The majority of the ions and atoms ablated from one half of the laser spot will collide with those ablated from the other half and, because of the symmetry of the concave-shaped target, acquire a velocity component along the system axis, and move towards the substrate.

2.8.2.6.6 Inverse Pulsed LASER deposition (IPLD)

One of the most usual but un-noticeable phenomenon concerning PLD is the material deposition on target surface and surrounding. This is usually noted as an undesirable effect but it can be exploited to our benefit for production of smoother thin films by utilizing back scattering plasma species which are usually free of particulates. Égerházi et.al [41] details this simple option to remove the droplets. In this geometry, substrate(s) is/are placed parallel to and slightly above the target plane and grows thin films on the surface utilizing the backscattered plasma species. To enhance backscattering, higher pressures (1-30 Pa) are employed and the value must be fine-tuned according to the target composition. Reports for stoichiometry studies have not come up yet for this geometry owing to its recent origin [42, 43, 44, 45, 46], but it shows a promising technique to reduce/remove droplets from the surface.

2.8.2.6.7 Magnetic field assisted PLD:

Since Plasma behaves like a magnetic material hence plasma species can be directed using magnetic field. Fernández et.al [47] designed and experiment where an axial field was generated opposing the plasma expansion and a transverse field was used to direct the particles towards the substrate. Droplets were be filtered out by modulating the magnetic fields. Kawasaki et.al [48] also used crossed-magnetic field technique to change the shape of plasma plume and hence deflecting away the droplets. The reported effective reduction the droplets when compared to usual case.

2.8.2.6.8 Electric Field assisted PLD:

Patsalas et.al. [49] biased the target using a DC electric field so that secondary ionization and field assisted acceleration in plasma species reduce particulate density by orienting and accelerating desired kinetic species towards the substrate. This method has additional advantage of improving the deposition rate (in this case, deposition rate increased from 2 to 7nm/min). It was also observed that these changes depend on the wavelength of LASER light as absorption coefficient of target material varies with incident light's wavelength and hence the plasma species changes considerably. Instead of DC field, Fominski et.al [50] used a pulsed electric field to accelerate selected plasma species for MoS_x thin films while maintaining the same stoichiometry.

2.8.2.6.9 Plume heating

Koren et.al [51] used a secondary LASER beam to heat up the plasma plume produces by primary beam and hence blow off the big droplets in the plume. This arrangement neither requires complicated geometry changes inside the chamber nor introduces foreign obstacles to the path of plasma which may contaminate. Thin films of $YBa_2Cu_3O_{7-\delta}$ were deposited with appreciably less droplets on the surface.

2.8.2.6.10 Femtosecond ablation

Gamaly et.al [52] demonstrated the advantages of shortening the LASER pulse width to picoseconds while depositing amorphous carbon films. Reducing the LASER pulse energy and increasing the repetition rate maintains the same deposition rate as well as removes the source of macroscopic particulate origin. Eventually they were able to obtain thin films with less than one particle per mm^2 which is an acceptable case for devise fabrication. Cannulescu et.al. [53] highlighted the difference in ablating $La_{0.6}Va_{0.4}CoO_3$ using a nanosecond and femtosecond pulse as well as the fact that femtosecond laser pulse do introduce deficiency of certain component species too! (Similar results about deficiency of certain component species was reported for Yttria stabilized zirconia for picosecond pulsed LASER by Salminen et.al [54]) Hence, femtosecond LASER pulses (which range from 6-fs to 200-fs) have found their use in a wide variety of material deposition apart from their traditional use in precision micromachining. Willmott and Huber [4] reviewed this state-of-art technique as one of the most promising one for multi-component thin film deposition. Dobbelly et.al. [55] described the dynamics of plasma plumes produced using a Langmuir ion probe technique. Advantage of using femtosecond

LASER pulse is that it takes few picoseconds to couple electronic energy to lattice. Thus femtosecond pulse effectively decouples these two processes. Thus ablation is performed without any collateral damage to the target material and this avoids the explosive material removal and hence the particulates on the thin film surface. Thus femtosecond ablation is more efficient since most of the incident photonic energy can be accounted for by the vaporization of ablated volume and subsequent kinetic energy of plasma species and degree of ionization of plasma. Negligible thermal effects, precise ablation threshold, high repeatability and efficiency and highly precise control of ablation geometry are few other advantages of using femtosecond LASER pulses. But these advantages come with additional cost of the equipment and its complex maintenance which has limited their use in academia as well as commercially.

Thus there exists various ways to control the number density of droplets on thin film surface. Choice of one or more above mention methods depends on the requirements of particular application. If droplets do not significantly alter the physical properties of single layer thin films, they can be ignored. In this thesis, we have just used the judicious use of suitable target to substrate distance to control the number density of droplets. Also, reduction of droplets was not our primary aim as they did not altered significantly any of the physical property of the material under study and also we did not aimed to produce multi-layered structures.

2.9 *Advantages of PLD*:

PLD counts some advantages over well-established physical methods of thin film deposition:

1. PLD can work with almost any kind of material including non-volatile materials whereas molecular Beam epitaxy limits its choices with easily volatile materials only.
2. Energy source (LASER) is placed outside the vacuum chamber which offers flexibility in geometrical arrangement of deposition system components as well as measurement systems if any.
3. Due to local heating, material can be selectively deposited from a layered target also.
4. Pulsed nature offer unique controllability of deposition thickness.
5. High kinetic energy of plasma plume promotes surface mobility and hence high-quality crystalline films can be achieved in a relatively simpler way. At the same time, they can be tuned to avoid bulk displacements.

6. Source material choice is virtually unlimited as choice of LASER parameters (like wavelength, intensity etc.) will determine the ablation process.
7. Under suitable conditions, ratio of elemental components can be maintained exactly the same as the target material. This offers a great advantage as compared to other methods where many parameters need to be finely optimized and even finely maintained during the whole course of deposition.
8. Ability to work in non-equilibrium conditions enables us to produce species with electronic states far from chemical equilibrium and hence novel and meta material's fabrication is much easier using PLD.
9. The LASER-target interaction responsible for ablation process is completely decoupled from other process parameters like background gas, type of substrate and substrate temperature. This results in better control of ablation dynamics for a variety of materials.

2.10 *Disadvantages of PLD*:

1. Formation of droplets poses a big disadvantage. A separate section is presented about minimizing droplet formation.
2. Impurity of target materials will be reflected in thin films too. Hence great deal of care is necessary to avoid any impurity from the starting of experiments.
3. Impurity in atmosphere of vacuum chamber will also be forced into thin film and hence high purity gases should be used and deposition chamber should be regularly cleaned after some set of depositions (particularly when targets are exchanged for depositions).
4. Crystallographic defects are generated in the thin film due to impinging high kinetic energy species. This can be avoided by fine tuning the LASER energy and deposition pressure.
5. Any inhomogeneity in flux and angular distribution of ablation plume is reflected as inhomogeneous thin film property. This can be avoided by polishing the target surface before mounting it on the target holder using suitable electronics to avoid instabilities fed to LASER,
6. PLD depositions are limited to smaller areas usually few mm^2. This can be improved by rotating the substrate holder and/or using multiple LASER beams.

7. PLD is a batch process and cannot be used for continuous deposition of films. This is a major disadvantage from an industrial use point of view.

2.11 Deposition of soft materials

Despite using high energy LASER light which violently ejects the target material to produce plasma which then rises to thousands of degrees, PLD can be used to deposit soft materials like polymers too. First report of polymer deposition was given by Hansen and Robitaile [56] where they used a weakly focused (spot size 0.1 cm^2) Nd.YAG LASER (energy range was 193 to 1064 nm and pulse energy density was 0.01-2J/cm^2) of smooth, homogeneous and pinhole-free polymer thin films. In the case of softer materials, it is important to use low energies but appropriate wavelength where ablation threshold of the components can be crossed without damaging the target and without depolymerizing the ablated species by thermal or photochemical means. Ueno et.al. [57] deposited PTFE (polytetrafluoroethylene) successfully. György et.al. [58] deposited even fragile bio-molecular papain (a protein cleaving enzyme derived from papaya plant) thin films using matrix assisted pulsed LASER deposition method. Matrix assisted target was prepared by dissolving papain in distilled water at 10 wt % papain concentration and freezing before and during the experiment in a custom made sample holder which circulates liquid nitrogen from low temperature maintenance. Usually matrix is chosen in such a way so that matrix has higher absorption coefficient than the embedded material. In this way, matrix absorbs the light and transfers it to embedded material which then receives appropriate energy for ablation. Leveugle and Zhigilei [59] developed molecular dynamics simulation model for ejection and transport of polymer molecules in matrix assisted pulsed LASER ablation and found out that explosive disintegration of overheated matrix resulting in polymer-matrix droplets. Violent phase explosions at higher fluences and stronger polymer entanglement for large polymer concentrations cause bond-breaking reactions and hence these conditions should be avoided.

Biological coatings [60, 61] can be fabricated using PLD with better efficiencies, especially in the cases where maintaining stoichiometry is a critical parameter for performance.

LASER ablation in liquid [62] is a new field which used PLD to synthesize high quality nanocrystals in liquid media. This new method is attracting attention since its chemically simple and clean synthesis process which can be run under ambient conditions without any extreme temperature and pressure requirements.

2.11.1 Experimental system of PLD at Tmfy-MSE

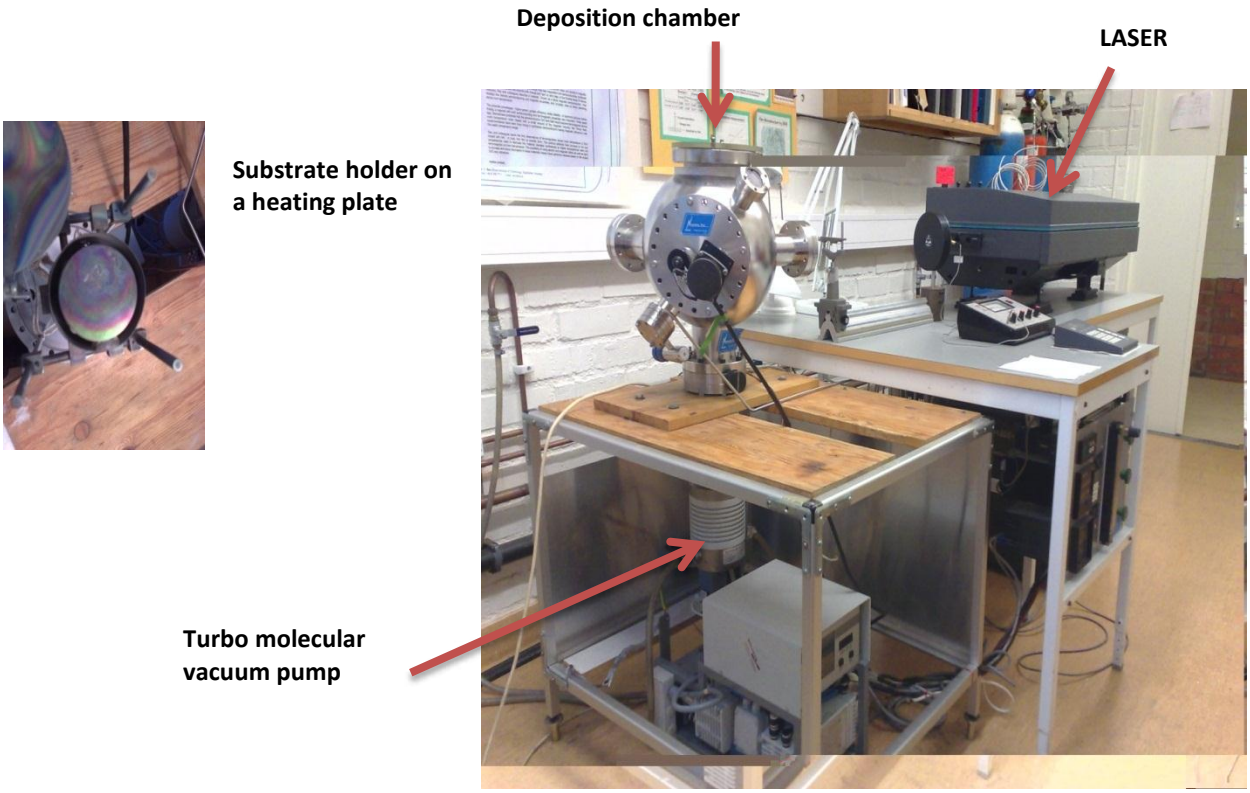

Fig. 2.4 *Our system consists of a Continuum NY 81C-10 Nd.YAG laser, a balzer trubo molecular pumping unit TSH 180 H and Neocera pulsed LASER deposition system*

2.11.2 Continuum NY 81C-10 Nd:YAG laser system (Fig: 2.4):

Nd:YAG LASER may be classified in the category of solid state LASER which consists of a transparent crystal as a host within which ionic species of LASER atoms (lasant) are interspersed or "doped". Typical host material includes Al_2O_3, garnates and various forms of glasses with most common lasing species being Nd ions. 1-2 % Nd^{3+} ions are used as the lasant with YAG($Y_3Al_5O_{12}$) as the host in our solid state laser system. The output wavelength for the fundamental frequency is 1.06μm which fall under the near IR region. Using harmonic

generators, harmonics are generated in visible (532 nm) and UV (355) regime as shown in Table: 2.1, 2.2 and 2.3

Wavelength (nm)	Energy (mJ)± Energy stability (%)
1064	1100±2.5
532	550±3.5
355	280±4

Table: 2.1 *Wavelength and corresponding energies for fundamental frequency (1064 nm) and its harmonics (532 and 355 nm).*

Wavelength (nm)	Pulse width (ns)
1064	5-7
532	4-6
355	4-6

Table: 2.2 *Wavelength versus Pulse width (given by full width half maximum)*

Divergence (full angle for 86% energy) = 0.45 (mrads)

Rod Diameter = 9.5mm ,Beam pointing stability = 250μrad and Jitter =0.5 n

Wavelength (nm)	Power Drift(±%)
1064	3
532	5
355	5

Table: 2.3 *Power drift at different wavelengths*

Power drift measurements are taken from operation for 8 hours

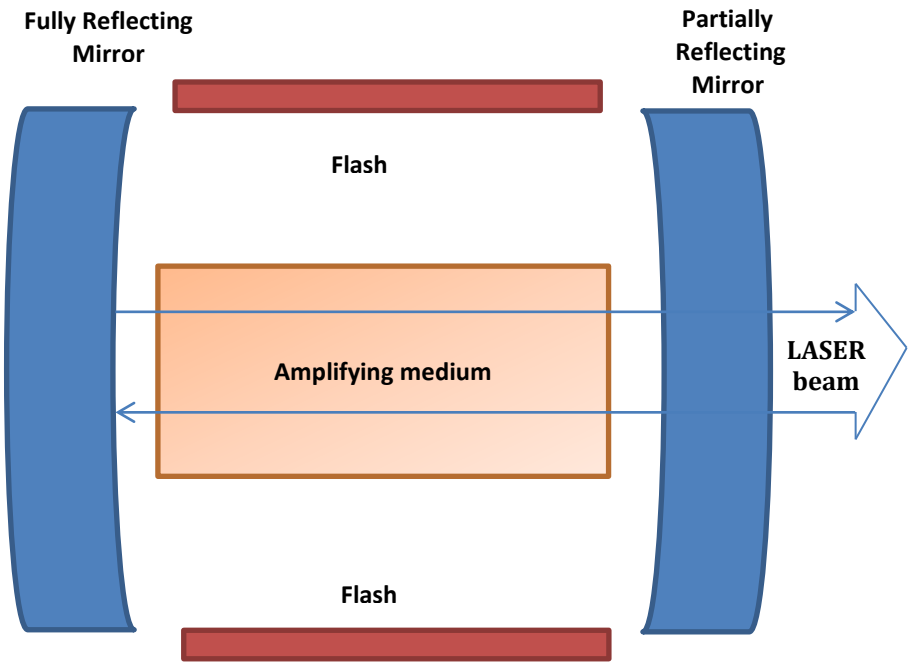

Fig: 2.5 *Schematic diagram of LASER cavity oscillator.*

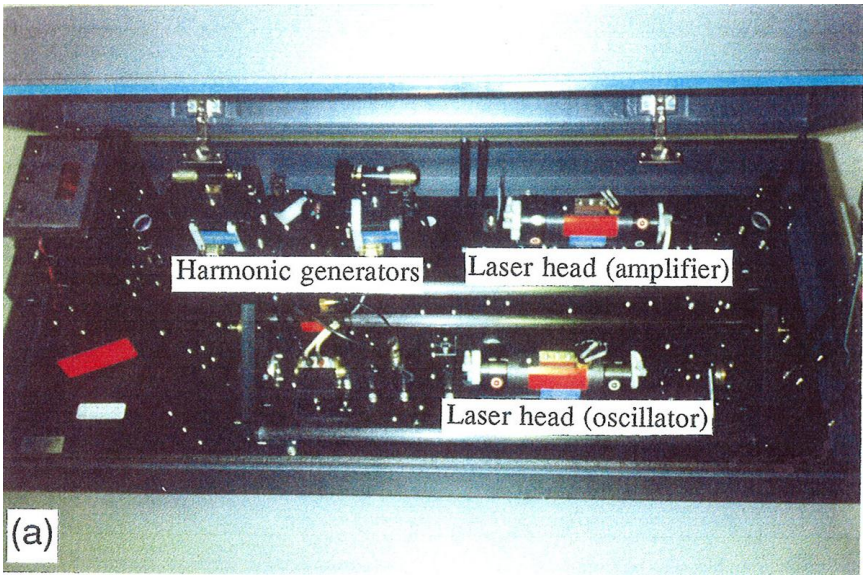

Fig: 2.6 *Position of Laser heads and harmonic generators on the optical bench.*

As seen in Fig: 2.5 and 2.6, LASER assembly is placed on an optical bench where distances are calibrated as per requirements. Whole assembly is secured with a dust-tight compartment during the routine operation.

2.11.3 Balzer turbo molecular pumping unit TSH 180H

Vacuum pump system consists of three components: a turbomolecular pump (10^{-8} to 1 Torr range with volume flow rate of 180 l/sec for nitrogen), MD 4 TC three stage diaphragms as dry working chamber backing pump, and electronic drive unit TCP 380. Advantage of the choice of using dry working chambers for vacuum pumps is that oil contaminants do not enter the deposition chamber.

2.11.4 Neocera pulsed LASER deposition system

Deposition system consists of:

1. 12” spherical chamber assembly
    - Contains two viewport and one input port (with quartz window) for LASER light, gas flow flange with a pirani vacuum guage and butterfly gate valve.
    - The 8” viewport window at top is used for visual check actual deposition process
2. A carousel 3 target holder assembly.
    - Target assembly can hold three targets, which can be switched without breaking the vacuum. Thus multilayers can be produced in situ. Target also rotates on its axis to avoid pitting during LASER ablation of its surface. Incident LASER beam hits the target at 45° at the target and send out plasma plume normal to surface of target. Exposed target area is regulated by a target shutter which avoids contamination of other targets during deposition from one of them
3. Substrate heater flange assembly
    - The substrate heater flange assembly allows heating the substrates up to 900°C for depositing at high temperatures.
4. Control panel
    - A programmable temperature controller is provided to regulate the step size and rate of temperatures for deposition.

2.12 ***References***

1. D. Dijkkamp, T. Venkatesan, X.D. Wu, S.A. Shaheen, N. Jisrawi, Y.H. Min-Lee, W.L.McLean, M. Croft, *Appl. Phys. Lett.* 51 **(1987)** 619
2. T. Venkatesan, X.D. Wu, A. Inam, J.B. Watchman, *Appl. Phys. Lett.* 52 **(1988)** 1193
3. J.T. Cheung, E.-H. Cirlin, N. Otsuka, *Appl. Phys. Lett.* 53 **(1988)** 53
4. P. R. Willmott and J. R. Huber *Reviews of Modern Physics,* 72 **(2000)** 315
5. T. Ohnishi, m. Lippmaa, T. Yamamoto, S. Meguro, H. Koinuma, *Appl. Phys. Lett.* 87 **(2005)** 241919
6. B. Dam, J.H. rector, J. Johansson, j. Huijbregtse, D. G. De Groot, *J. Appl. Phys*, 83 **(1998)** 3386
7. J, Schou, *Applied Surface Science* 255 **(2009)** 5191-5198
8. R. Timm, P. R. Willmott, and J. R. Huber, *J. Appl. Phys.* 80 **(1996)** 1794
9. B. Thestrup, B. Toftmann, J. Schou, B. Doggett, J.G. Lunney, *Applield Surface Science* 197-198 **(2002)** 175-180
10. R.K. Singh, J. Narayan, *Phys. Rev. B* 41 **(1990)** 8843
11. A. Amoruso, A. Sambri, X. wang, J. Appl. Phys, 100 (2006) 013302, N. Arnold, j. Gruber, J. Heltz, *Appl. Phys. A* 69 **(1999)**S87
12. S. Amoruso, R. Bruzzese, N. Spinelli, R. Velotta, M. Vitiello, X. wang, *Phys, Rev. B* 67 **(2003)**224503
13. M. Strikovski, J.H. Miller Jr., *Appl. Phys. Lett* 73 **(1998)**1733
14. C. B. Arnold, M. J. Aziz, *Appl. Phys. A* 69 **(1999)** S23-S27
15. Sibold, D., and H. M. Urbassek, *Phys. Fluids A* 4 **(1992)** 165
16. J. F. Ready, *Appl. Phys. Lett.* 3 **(1963)**11
17. Aurelian Marcu, Takeshi Yanagida, Kazuki Nagashima, Hidekazu Tanaka, and Tomoji Kawai, *Journal of Applied Physics* 102 **(2007)** 016102
18. Kai Sturm, Hans-Ulrich Krebs, J. Appl. Phys. 90 (2001) 1061, S. Fähler, K. Sturm, H-U. Krebs, *Appl. Phys. Lett*, 75 **(1999)** 3766
19. Wolfgang Bauer, Gerhard Betz, Herwig Bangert, Anton Bergauer, Christoph Eisenmenger-Sittner, *J. Vac. Sci. Technol. A* 12 **(1994)** 3157

20. R. Dietsch, Th. Holz, H. Mai, C-F Meyer, R. Scholz, B. Wehner, *Applied Surface Science* 127-129 **(1998)** 451-456
21. R. Dietsch, Th. Holz, D. Weißbach, R. Scholz, *Applied Surface Science* 197-198 **(2002)** 169-174
22. S. Fähler, M. Störmer, H.U. Krebs, *Applied Surface Science* 109/110 **(1997)** 433
23. R.K. Singh, D. Bhattacharya and I. Narayan, *Appl. Phys. Lett.* 57 **(1990)** 2022
24. Wee-Ong Siew, Wai-Keat Lee, Hin-Yong Wong, Thian-Khok Yong, Seong-Shan Yap, Teck-Yong Tou, *Appl. Phys. A* 101 **(2010)** 627-632
25. R. Kelly and A. Miotello, ``Mechanisms of Pulsed Laser Sputtering'' in Pulsed Laser Deposition of Thin Films, D. B. Chrisey and G. K. Hubler (editors), John Wiley & Sons Inc., New York, (**1994)**
26. G. Koren, A. Gupta, R J. Baseman, M. I. Lutwyche, and R. B. Laibowitz, *Appl. Phys. Lett.* 55 **(1989)** 2450
27. Frédéric Tcheliebou and Sunggi Baik, *J. Appl. Phys.* 80 **(1996)**7046
28. T. Szörényi, R. Stuck , F. Antoni , E. Fogarassy, *Applied Surface Science* 247 **(2005)** 45
29. D.S. Misra and S.B. Palmer, *Physica C* 176 **(1991)**43-48
30. Lai et.al. *Chineese Journal of Physics*, 36**(1998)**382
31. Z. Trajanovic, S. Choopun, R. P. Sharma, T. Venkatesan, *Appl. Phys. Lett.* 70 **(1997)** 3461
32. Inoue et.al. *Jpn. J.Appl. Phys.* 36**(1997)**704
33. Tsuyoshi Yoshitake, *Jpn. J. Appl. Phys.* 41 **(2002)** 836
34. Hino et.al. *Vacuum* 70 **(2003)** 47
35. Holzapfel, B. Roas, l. Schultz, p. Baeur, G. Saemann-Ischenko, *Appl. Phys. Lett.*, 61**(1992)**3178
36. Robin J. Kennedy, *Thin Solid Films*, 214 **(1992)** 223-228
37. Daniel Zemsky, Roni Shnech, Paul J. Dagdigian, IIana Bar, *Journal of Applied Physics* 102 **(2007)**104309
38. Soon-Gul lee, Doo-Sup Hwang, Yong Ki Park, Jong-Chul Park, *Appl. Phys. Lett*, 65 **(1994)** 764
39. Valentin Craciun, *Mat. Res. Soc. Symp. Proc*. 526 **(1998)**111

40. M.D. Strikovsky, E.B. Klyuenkov, S.V. Gaponov, J. Schubert and C.A. Copetti, *Appll. Phys. Lett.* 63**(1992)**1146
41. L. Égerházi, Zs Geretovsky, T. Szörényi, *Appl. Phy. A* 93 **(2008)** 789
42. L. Égerházi, Zs Geretovsky, T. Szörényi, *Appl. Surf. Sci.* 247 **(2005)** 182, 252 **(2006)** 4656, 252 **(2006)**4661
43. P. Petrik, T. Lohner, L. Égerházi, Zs Geretovsky, *Appl. Surf. Sci.* 253 **(2006)** 173
44. T. Szörényi, Zs Geretovsky, *Thin Solid Films* 484 **(2005)** 165
45. L. Égerházi, Zs Geretovsky, T. Szörényi, *Appl. Surf. Sci.* 257 **(2011)** 5324
46. V. M. Gordienko, V. A. Dyakov, Y. Y. Kuzyakov, I. A. Makarov, E. V. Rakov, M. A. Timofeev, *Quantum Electron.* 37 **(2007)** 285
47. C. de Julián Fernández et al. *Applied Surface Science* 138–139 **(1999)** 150
48. Hiroharu KawasakiU, Kazuya Doi, Satoshi Hiraishi, Yoshiaki Suda, *Thin Solid Films* 374 **(2000)** 278-281
49. P. Patsalas, S. Kaziannis, C. Kosmidis, and D. Papadimitriou, G. Abadias, G. A. Evangelakis, *J. Appl. Phys*, 101 **(2007)**124903
50. V. Yu. Fominski, V. N. Nevolin, and R. I. Romanov, I. Smurov *J. Appl. Phys* 89 **(2001)**1449
51. G. koren, R.J. Baserman, A. Gupta, M.I Lutwyche, R.B. Laibowitz, *Appl. Phys. Lett.* 56 **(1990)**2144
52. E.G. Gamaly, A.V. Rode, B.Luther-Davies, *J. Appl. Phys*, 85 **(1999)**4213
53. S. Canulescu, E. Papadopoulou, D. Anglos, T. Lippert, M.J. Montenegro, S. Georgiou, M. Döbeli, A. Wokaun, *Appl. Phys. A* 105 **(2011)** 167-176
54. Turkka Salminen, Mikko Hahtala, Ilkka Seppälä, Pekka Laukkanen, Tapio Niemi, *Appl. Phys. A* 101 **(2010)** 735-738
55. T. Donnely, J.G. Lunney, S. Amoruso, R. Bruzzese, X. Wang, X Ni, *J. Appl. Phys*, 108 **(2010)**043309
56. S. G. Hansen and T. E. Robitaille, *Appl. Phys. Lett.* 52**(1988)** 81
57. Y. Ueno, T. Fujii, and F. Kannari, *Appl. Phys. Lett.* 11**(1994)**1370
58. E. György, A. Pérez del Pino, G. Sauthier, and A. Figueras, *J. Appl. Phys.* 106 **(2009)**114702
59. Elodie Leveugle and Leonid V. Zhigilei, *J. Apply. Phys*, 102**(2007)** 074914

60. E. L. Solla, J. P. Borrajo, P. González, J. Serra, S. Chiussi, B. León, J. García López, *Applied Surface Science* 253 **(2007)** 8282-8286
61. S. Liste, P. González, J. Serra, J. P. Borrajo, S. Chiussi, B. León, M. Pérez-Amor, J. García López, F. J. Ferrer, Y. Morilla, M.A. Respaldiza, *Thin Solid Films* 453-454 **(2004)** 219-223
62. Yang G. W, *J. Prog Mater Sci* **(2006)**, doi:10.1016/j.pmatsci.2006.10.016
63. Operations and maintainence manual NY 80,81,82, Continuum, Oct **1990**

Chapter 3

High energy product thin films for NEMS/MEMS

Tailoring PLD deposited $Fe_{52}Pt_{30}B_{18}$ based films to become Nanoscale Exchange coupled 'Spring Magnets'

3.1. *PLD technique enables deposition of Fe-based Films*

High-energy product permanent magnets have been used in a variety of applications. Recently thin film technology driven NEMS/MEMS (Nano/Micro Electro-Mechanical Systems) devises employed miniaturized component sizes, thus demanding a more efficient and cost effective devise fabrication. MEMS employing magnetic components would require high quality permanent magnet components too. Thin films of high energy product permanent magnets will fulfill this requirement. For reasons to be elaborated later Magnetron Sputtering technique is not suitable to tailor cobalt free Fe-Pt-B based thin films as hard magnets. We have developed such magnets by using PLD technique.

In the case of High-energy product permanent magnets, the primary requirements are large saturation magnetization and high coercivity. Kneller and Hawing [1] proposed a new material principle for devising permanent magnets using nanocomposite of a soft and hard magnetic phase. They proposed that the essential conditions for the microstructure of such materials are a fine and regular dispersion of soft and hard magnetic phases on a scale of the order 10 nm and exchange coupling between these regions. Fabricating such a complex composite material, which has crystallographically coherent formation of two phases with generally different structures, involves growth of these phases from a glassy state using suitable annealing conditions. Fabrication of desired permanent magnet from glassy state has been studied for over two decades now [2, 3, 4, 5, 6, 7, 8]. Depending on the annealing scheme, fine and well defined size and shape of crystallites can be grown with same or different crystallographic orientations.

Coehoorn et. al. [6, 7,8] fabricated such permanent magnet using $Nd_4Fe_{77}B$ alloy by liquid quenching and subsequent heating of alloys. With 85% soft magnetic phase (73% Fe3B and 12% a-Fe) and 15% hard magnetic phase ($Nd_2Fe_{14}B$), it showed very promising large coercivity of 280kA/m along with an unusually high isotropic remanence ratio > 0.5. Kneller and Hawing

[1] followed up this work on this material and found essential conditions for fabricating spring magnets.

Nanocomposite configuration can be obtained by fabricating a magnetically hard and soft nana-scale phases, which exchange-couple at interface. Magnetic hard phase provides high-anisotropy which contributes towards higher coercivity. Magnetic soft phase provides large saturation magnetization. Also, this configuration shows reversible demagnetization curve which defines the ability of magnet to maintain its magnetization, when a magnetic field is applied in reverse direction. For this reason, these magnets are called "exchange coupled spring magnets" in analogy to motion of a mechanical spring which comes retains the amplitude of vibration according to spring constant of the material. Retention of magnetization is important from application point of view. Problem with Nd-Fe-B and Sm-Co based nanocomposite permanent magnets [9] has been their susceptibility to oxidation [10] which requires them to be coated with a protective layer for applications in strong chemical environments.

In this regard, Fe-Pt system shows promising properties as corrosion resistant [11] permanent magnet [12]. Also thin films of Fe-Pt shows higher coercivities [Hc=3200kAm^{-1}] compared to their bulk form [400kAm^{-1}] due to the formation of an ordered tetragonal phase (LI_0 FePt) which has extremely high magnetocrystalline anisotropy (K=7MJm^{-3}) [13]. This makes it ideal candidate for application in fabricating high-energy product permanent magnet, especially when the size of both hard and soft magnetic phases are in nanometer range because in that case exchange coupling is enhanced, which further enhances the energy product of the magnet [1]. The high-cost of Pt is one of the limiting reason for this material to be used in applications, thus addition of non-magnetic elements like B, C or Ag [14-20] was considered. Addition of B to FePt alloy leads to necessary L10-Fe-Pt phase isolation to weaken intergranular exchange. While this is disadvantageous for memory applications, it can be useful for high-energy product permanent magnets for MEMS applications. Using melt spinning technique, $Fe_{52}Pt_{30}B_{18}$ ribbons were made by Zhang et al [21-23] and a new type of $L1_0$ FePt/Fe_2B nanocomposite hard magnets with a lower concentration of Pt (~ 30 at %). $Fe_{52}Pt_{30}B_{18}$ ribbon magnets were obtained which exhibits good hard magnetic properties [Hc = 783kA/m and $(BH)_{max}$ = 88.0kJ/m^3].

2.2.Motivation for PLD deposition of FePtB thin films

An excellent hard magnetic property of FePtB configuration was our inspiration to fabricate thin films of this material for its potential applications in MEMS devises. Sharma et.al first fabricated these thin films using sputtering technique [24] and obtained an in-plane Hc ~604 kA/m. On the basis of existence of strong exchange coupling among the nanosized soft [Fe_xB (x = 2,3)] and L10 Fe-Pt hard magnetic phases, thin films magnetic properties were explained. But sputtering technique required specifically a disc shaped, atleast 50mm target. Fabrication of large sized sputtering targets containing Fe,Pt and B in specific composition is difficult and time consuming. Also, sputtering technique do not guarantee stoichiometric transfer of elements from target to the thin film and in our case, specific percentage of B is necessary to meet the requirements of a quality permanent magnet. These problems can be easily overcome by PLD as this technique requires a small sized target (>10mm) of virtually any shape (only the top surface for ablation should be flat). Also the deposition rate of PLD is faster as compared to sputtering system, which is a likable feature from commercial point of view. Apart from that PLD offers a wide choice of substrates for deposition. Increasing demand of NEMS/MEMS fabrication on flexible substrates makes PLD a suitable option.

In the nest section we shall discuss the fabrication of FePtB thin films on two types of substrates: Glass and Si. Effect of choice of substrate and that of deposition parameters like substrate temperature is studies in great detail to obtain best possible combination of conditions for deposition. It is particularly important to notice that even slight changes in choices of substrate and deposition conditions changes physical properties drastically and hence this particular exercise of finding the right combination for PLD deposition is repeated for each new materials in coming chapters.

3.2. *PLD Deposition*

A target of $Fe_{52}Pt_{30}B_{18}$ alloy was made by the arc-melting technique (base pressure~10^{-4}Pa) at IMR, Sendai (Japan) and supplied to us. High-purity (99.99%) Fe, Pt and B metals were arc-melted in appropriate proportions according to the stoichiometry requirements of $Fe_{52}Pt_{30}B_{18}$ composition, Arc melting was performed under an argon atmosphere in a water cooled copper die to avoid oxidation. Multiple arc-melting sessions were performed to obtain a uniform distribution of all the elements throughout the Fe-Pt-B alloy ingot. This target material was used in PLD after confirming its composition using EDS.

Three thin films were fabricated on Si substrate and 4 thin films were fabricated on fused glass substrate under conditions mentioned in the Table: 3.1

Sample #	Pressure (μbar)	Temperature (°C)	Energy (mJ/Pulse)	Time (minutes)	Substrate
P806201	7	370	100	30	Si
P806231	7	400	100	30	Si
P806251	7	450	100	30	Si
P806271	7	450	100	30	Fused Glass
P806301	7	475	100	30	Fused Glass
P806302	7	500	100	30	Fused Glass
P807021	7	525	100	30	Fused Glass

Table: 3.1 *Deposition conditions for $Fe_{52}Pt_{30}B_{18}$ thin films using PLD.*

Crystallographic information about the thin films was obtained by using an X-ray diffractometer (XRD). Electron Probe microanalysis (EPMA) was used for the compositional analysis. The magnetic properties of the films were measured by using a quantum design SQUID magnetometer. The scanning electron microscope (SEM) and atomic force microscope (AFM) were used to study the surface morphology and the growth structure.

3.3. *Tailoring the composite structure*

Sharma et.al [24] found that at a substrate temperature (T_s) of ~ 370 ^oC, a nano-composite structure mainly made of soft-magnetic Fe_2B and hard-magnetic L10-FePt phases was formed.

At T_s ~ 370 ^oC on Si substrate, the major phase was found to be disordered (111) face centered cubic (fcc) FePt, suggesting that a higher temperature is required to form L10-FePt and Fe_2B phases in case of PLD. It is important to note here that substrate temperature requirements for sputtering and PLD system might not be same as growth conditions from plasma can be considerably different in both cases.

As described in chapter 2, PLD deposition process is an non-equilibrium dynamics process and hence deposition requirements are quite distinct compared to other deposition process. Incoming species to the substrate vary in charge, mass, kinetic energy etc. when compared with sputtering and hence deposition rates as well as thin film growth on substrate vary with change of deposition technique.

Sputtering develops plasma by momentum transfer of accelerated charge ions from the target which yields lower degree of ionization. In case of PLD, due to non-equilibrium dynamics of high energy-light incident on target material, degree of ionization and composition of plasma in general is different, which leads us to believe that PLD may require separate set of conditions to grow thin films of same configuration as that of sputtering.

Hence it is pertinent to explore the deposition conditions of FePtB system fresh, during PLD depositions. Simultaneous XRD, AFM and magnetic measurements guide us towards best possible set of parameters of deposition. Also, when we change the substrate to see the effect of substrate on thin film properties (due to change in growth dynamics at substrates which offer different growth surfaces), we have to perform simultaneous structural magnetic and topographic measurements to observe the changes in growth dynamics which guide us towards the best possible set of parameters.

3.5.*Structural Characterization*

XRD diffraction of the thin film guides us to correct deposition temperature for deposition by indicating the onset of crystallization of desired phase. By raising T_s to ~ 400 ^oC, XRD curve do not show any appreciable change indicating requirement of still higher temperatures for formation of nano-composite. At T_s ~ 450 ^oC, many peaks new appear in the XRD curve (Fig 3.1(a)).

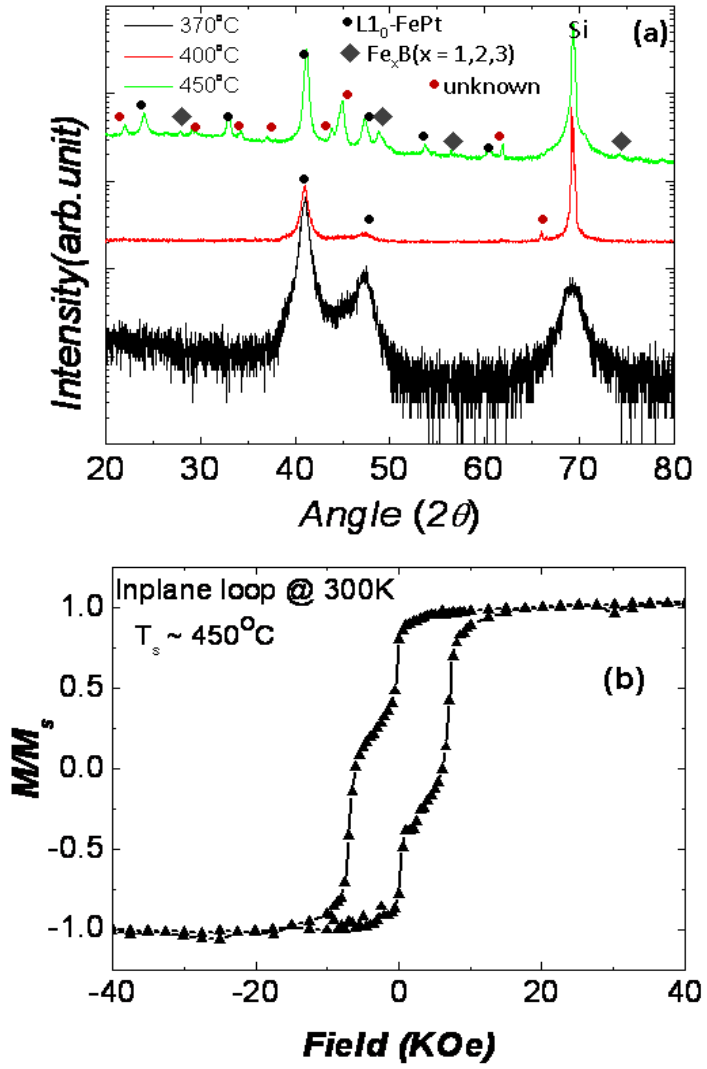

Fig. 3.1 *(a) X-ray diffraction patterns for FePtB films deposited on Si substrates at different substrate temperatures. (b) Hysteresis loop measured at room temperature (300K) for FePtB thin film deposited at T_s ~ 450^{o}C.*

Fig:3.1 (a) shows that for T_s ~ 450 ^{o}C, most of the peaks correspond to L10 FePt and Fe_xB (x=1,2,3) phases. Some unknown peaks were also noticed, which probably originate from the phases formed by diffusion of film into the Si substrate. The in-plane magnetic hysteresis loops measured at 300K showed that while the thin films deposited at T_s ~ 370 ^{o}C are soft magnetic with a coercivity value of < 5 Oe, H_c was found to increase with increase in T_s upto 6.0 KOe for T_s ~ 450 ^{o}C.. A two phase like hysteresis loop shape [Fig. 3.1 (b)] is observed. The observed magnetic properties are in accordance with the XRD results since FePt phase is indeed

a soft magnetic one and transformation from fcc FePt to L10-FePt along with formation of FeB phase leads to multi-phase magnetic behavior as seen by two phase like hysteresis loop.

Zhang et.al. [22,23] reported that for FePtB ribbons and thin films made up of soft magnetic Fe-B and hard magnetic L10-FePt, a single phase-like hysteresis loops exits due to strong inter-granular exchange-coupling among the nano-sized soft and hard magnetic [25]. If the exchange coupling is weak, two phases will show their magnetic behavior independently, as we saw in the room temperature hysteresis loop. This exchange coupling between the hard and soft magnetic phase will depend on grain-sizes, volume fractions and the separation between these two phases which would require elevated temperatures, But we observed that at T_s 450 ^oC for Si substrate, diffusion of film and substrate posed a problem in this regard. Hence these thin films must be deposited on another kind of substrate at higher temperature. We chose fused glass substrate for these experiments.

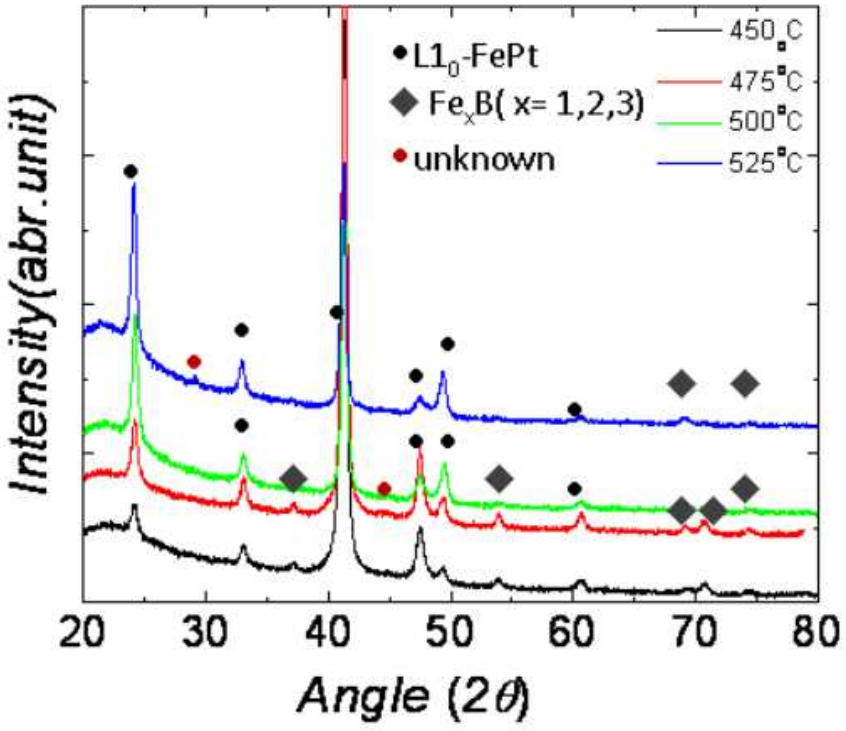

Fig. 3.2 *X-Ray diffraction patterns for FePtB thin films deposited on glass substrate at different substrate temperatures, showing formation of soft (Fe-B) and hard (L10-FePt) magnetic phases.*

XRD spectra of thin film on glass (Fig: 3.2) were checked first to identify the temperature required to form the desired nanocomposite. It was observed that growth of $Fe_{52}Pt_{30}B_{18}$ thin film is sensitively dependent on the type of substrates (Si or SiO_2) and the growth temperature (T_s) since peaks observed for $Fe_{52}Pt_{30}B_{18}$ films deposited on SiO_2 substrate are different from the films deposited on Si substrate under identical conditions. All the peaks in XRD patterns for FePtB thin films deposited on SiO_2 substrate matches with the L10-FePt and iron-boride phases. The fcc-FePt and L10-FePt phases coexist in the films deposited at 450ºC. Below 450^oC disordered fcc (111) plane is known as the dominant phase from our experiments on silicon substrate. Since the ordering transformation (fcc-FePt to L10-FePt) does not require long range diffusion, it occurs rapidly once the thermal energy is large enough for short range diffusion. At elevated temperatures another phase consisting of Fe and B (Fe_xB; x =1, 2, 3) appears. On further increase in T_s, increase in grain size and volume fraction of hard and soft magnetic phases is expected. It should be noted that the XRD pattern of FePtB thin films at Ts ~ 525 ^oC is similar to the best hard magnetic FePtB thin film deposited by sputtering technique [24] but with a much smaller target and relatively simpler fabrication method.

3.6.*Magnetic properties*:

The magnetic properties of FePtB thin films deposited on SiO_2 substrate were investigated at room temperature (300K) using a SQUID magnetometer (Fig: 3.3).

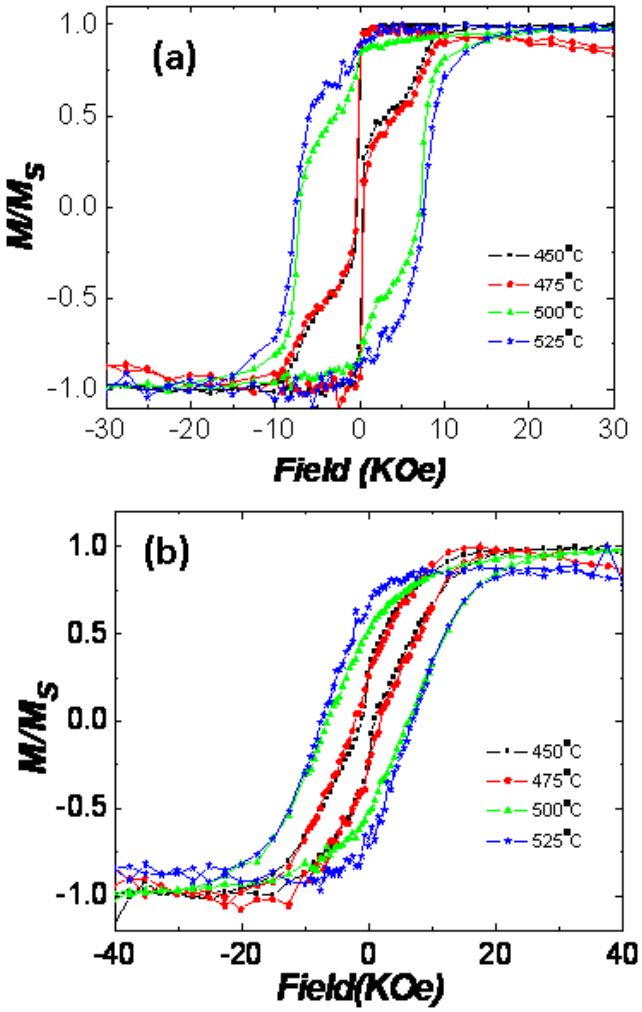

Fig. 3.3 *Hysteresis loops measures at room temperature (300K) for FePtB thin films deposited on glass substrate at different substrate temperatures (a) in-plane and (b) out-of-plane. A pronounced two phase like hysteresis loop shape in in-plane direction can be noticed at lower substrate temperatures.*

Fig: 3.3 (a), (b) shows the in-plane and out-of-plane hysteresis loops. It should be noticed that at lower T_s the H_c values are low in both the in-plane and out-of-plane configuration. As the temperature increases there is an increase in H_c values (indicating the formation of two phase system) and reaches a maximum at T_s ~ 525 ^oC. In out-of-plane hysteresis measurements, the shape of the hysteresis loop is like a single phase and does not change with increase in T_s. However, a two-phase like hysteresis loop shape can be noticed in the case of hysteresis loops measured in in-plane direction. As the T_s increases, hysteresis loop shape approaches towards the

single phase like shape. At T_s ~ 525^{o}C, the in-plane hysteresis loop shape is more close to a single phase like magnets. The value of H_c obtained for this films is ~ 7.7 KOe (613 kA/m) and ~ 7.2 KOe (573 kA/m) in in-plane and out of plane directions respectively. These values of H_c are similar to the best hard magnetic thin films obtained from sputtering technique (H_c in-plane ~ 604 kA/m; H_c out-of-plane ~ 567 kA/m) [24] which match with our XRD results too.

3.7.*SEM and AFM investigation*

Magnetic properties are a function of grain size and surface morphology so SEM and AFM investigation of these thin films were carried out. SEM images show "droplets" of on surface of these thin films, which is characteristic of PLD deposition. SEM images of the films deposited at different T_s revealed a fine nano-scale granular structure. Droplet size and their number were found to reduce with increase in T_s [Fig: 3.4 (a), (b)] which is a desirable feature for NEMS/MEMS applications.

Chapter 2 already discussed about the droplet formation during PLD deposition and it cannot be avoided. But if their number can be reduced sufficiently then one can have enough droplet free area on thin film surface to fabricate NEMS/MEMS devises. It is important to find a proper parameter to achieve reduction of droplets and in our case it turned out to be surface temperature of substrate. The reason for reduction of droplets could be enhanced mobility of incoming plasma species and their subsequent decomposition of big droplets due to elevated temperatures.

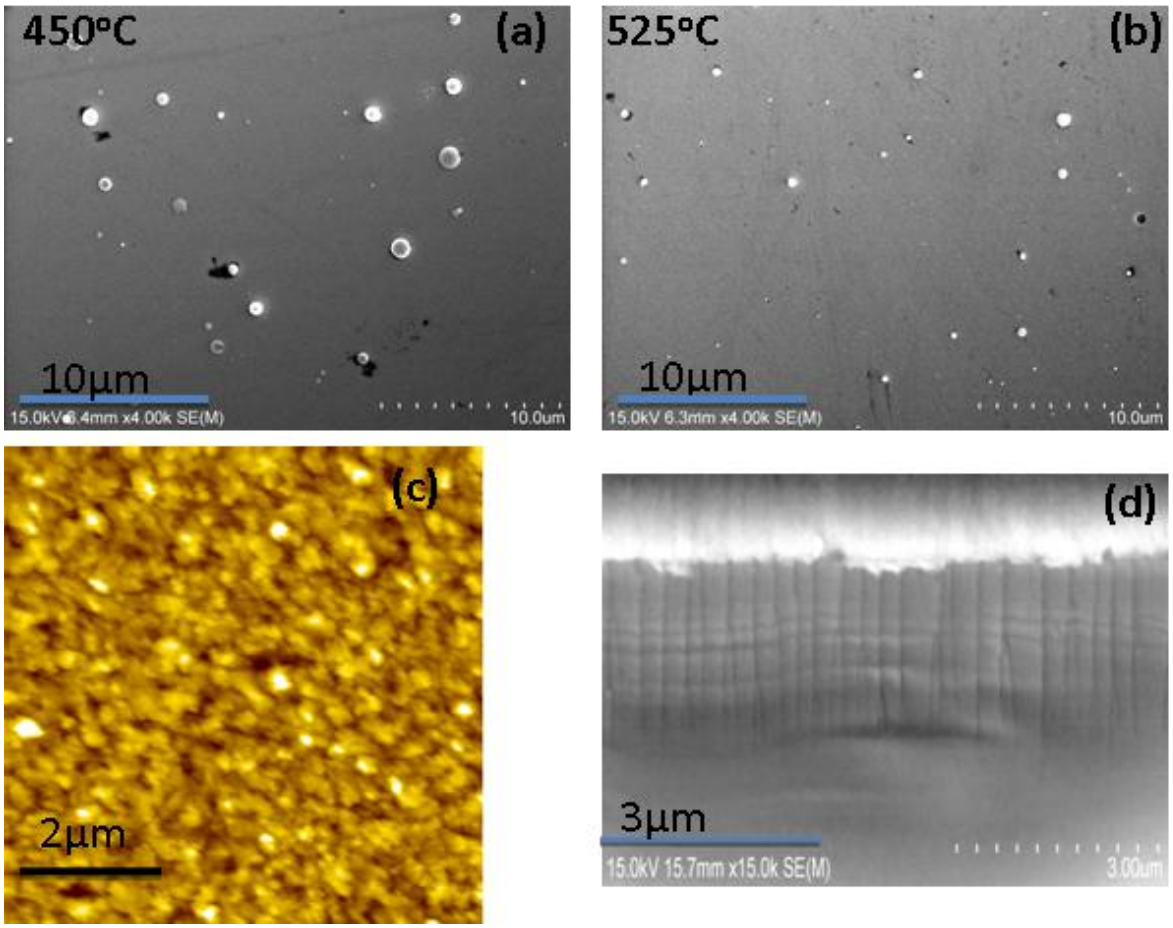

Fig. 3.4 *SEM images for FePtB thin film on fused glass deposited at (a) T_s=450°C and (b) T_s=525°C showing reduction in droplet size and density with increasing temperature. (c) Topographic AFM image of best magnetic thin film i.e T_s=525°C and (d) cross-sectional SEM image for thin film grown on fused glass substrate.*

Grain size affects magnetic properties of these thin films hence AFM topographic investigation was undertaken for the same. AFM image of best hard magnetic thin film (i.e. at T_s ~ 525°C) [Fig: 3.4 (c)] showed nanometer-sized grains with different sizes. This could be due to different phases [L10-FePt and Fe_xB (x = 1, 2, 3)] being present in the film. It would be difficult to draw this conclusion about the different types of grains from the AFM image only but we can do so by combining the visual evidences with the information gained from the XRD measurements. It is worth mentioning that in case of pure FePt thin films, the grain size distribution seen in the AFM images was reported to be narrow (i.e. the grains were nearly of same size). The grain size distribution remain narrow even with increasing T_s, which only results in the transformation of fcc FePt to L10-FePt phase along with an increase in grain size [26].

This can be easily understood because the FePt films consist mainly of a single phase. The scanning electron microscope image taken along the thickness of the film [Fig:3.4 (d)] reveals that the film growth is in the form of columns. This growth behavior is quite different from the pure L10-FePt thin films where the columnar growth structure was absent [27]. From the SEM images we have also determined the thickness of our best hard magnetic thin film and it is found to be ~ 1.7 μm.

The exact composition of the film measured by EPMA technique is $Fe_{52}Pt_{39}B_9$. A significant loss of B can be noticed in the film as compared to the target composition ($Fe_{52}Pt_{30}B_{18}$). This variation in composition is expected and can be due to the different angular distribution of ejected particles with different atomic masses. The deviation of lighter species from the normal direction due to scattering processes seems a plausible explanation for reduction in B content in the film.

3.8. ***Results***

By comparing the structural, magnetic and growth characteristics of pulsed laser deposited best hard magnetic FePtB thin films with nano-composite FePtB exchange-coupled hard magnetic thin films obtained from sputtering [24], it can be concluded that both the films exhibit similar properties. This means that the good hard magnetic properties of FePtB thin films deposited by PLD technique originate from the strong exchange coupling among the soft [Fe_xB (x = 1, 2,3)] and hard L10-FePt magnetic nano-sized grains present in the film. Here, magnetization of the soft phase is known to be pinned by the hard magnetic phase through an exchange coupling at the interfaces. As a result, the magnetic moments in the soft magnetic phase are expected to rotate reversibly up to a critical field during the magnetization reversal process. Inter-granular exchange coupling in these types of material dependens on the grain sizes of both the hard and the soft magnetic phases. It has been noticed that if the grain sizes are below or above some critical size, the exchange coupling becomes weak, showing the loops with a pronounced kink around H=0, which indicates that the soft phase does not switch together with the hard phase. This type of situation can be easily noticed in case of FePtB films deposited below $T_s < 525\ ^oC$ [Fig. Hysterisis loops for fused glass substrate (b)].

In nano-composite magnets both magneto-static (dipolar) and exchange interactions are responsible for the observed magnetic behavior [28,29]. Inter-granular dipolar interactions are generally considered as detrimental to the hard magnetic properties [29]. However, in some special cases of anisotropic magnets, dipolar interactions can improve the magnetic properties [30]. Therefore it is necessary to identify the type of coupling (exchange or dipolar) in laser deposited FePtB nano-composite magnet. The nature (exchange or dipolar) of coupling in a nano-composite magnet can be identified by measuring the Henkel plot or δM plot [29,31]. For an assembly of magnetically uniaxial non-interacting single domain particles, it is known that the remanent magnetization $M_r(H)$, which is measured after thermal demagnetization and subsequent magnetization at field H on the virgin curve, and the demagnetization remanence $M_d(H)$, which is measured after demagnetization at –H on the demagnetization curve, should obey the following relation [32]:

$$M_d(H) = M_r - 2M_r(H) \quad (1)$$

Where, M_r is the maximum remanent magnetization (remanence) measured after saturation. The deviation of measured $M_d(H)$ and $[M_r - 2M_r(H)]$, can be used for the interpretation of inter-grain exchange. This deviation dM is defined as [28]:

$$\delta M = \frac{M_d(H) - [M_r - 2M_r(H)]}{M_r} \quad (2)$$

Positive dM values are interpreted as exchange interactions, whereas negative dM values correspond to dipolar interactions. Fig. shows δM plot for laser ablated FePtB thin film exhibiting best hard magnetic properties. The positive value of δM clearly indicates an exchange type of interactions among the nano sized $L1_0$ -FePt hard and Fe_xB (x =1, 2, 3) soft magnetic phases. In addition to this, a high value of reduced remanence (M_r/M_s ~ 0.9) is also an indication of strong exchange coupling among the soft and hard magnetic phases present in the film.

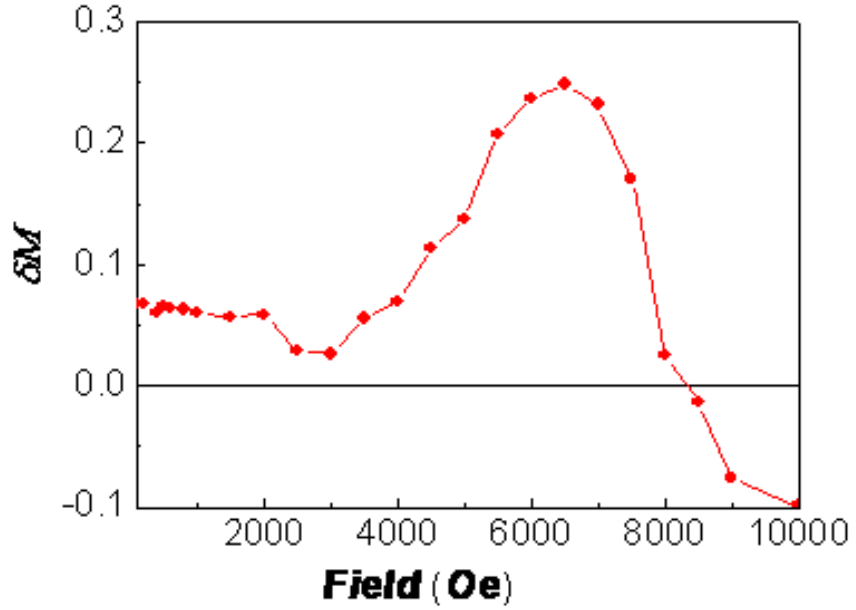

Fig. 3.5 *δM or Henkel plot measured at room temperature (300 K) for the best hard magnetic FePtB thin film. The positive value of δM shows the presence of strong exchange coupling among the soft and hard magnetic phases present in the film.*

Thus Fe-Pt-B thin films were successfully deposited on silicon and glass substrates. Proper deposition conditions like choice of substrate temperature and temperature were studied with coherent studies of XRD and magnetic measurements and finally best hard magnetic behavior [H_c ~ 7.7 KOe; M_r/M_s ~ 0.9] was observed for 525°C substrate temperature for fused glass substrate. A strong exchange coupling among the nano-sized soft and hard magnetic phases is responsible for the observation of good hard magnetic properties. PLD proved to be a promising technique for the fabrication for NEMS/MEMS applications involving permanent magnet.

3.9. ***Future work***

Following experiments can be designed to further investigate in this arena:

- Studying the effect of Fe-Pt-B composition for reducing the expensive Pt content but still maintaining good hard magnetic properties.

- Fabrication of amorphous Fe-Pt-B thin films by depositing at room temperature and study of evolution of crystallization and subsequent magnetic properties.
- Reduction of number of droplets by depositing thin films in off-axis geometry
- Fabrication of Fe-Pt-B thin films on other substrates especially flexible ones for applications involving flexible NEMS/MEMS devices.

3.10. ***References***

1. E.F. Kneller and R. Hawig, *IEEE Trans. Magn.* 27, **(1991)** 3588
2. J. J. Croat, *J. Magn. Magn. Mar*.24(**1981**)125
3. J. J. Croat, J. F. Herbst, R. W. Lee, and F. E. Pinkerton, *J. Appl. Phys.*, 55 **(1984)** 2078,
4. J. J. Becker, J. Appl. Phys., 55(**1984**) 2067
5. K. H. J. Buschow, D. B. de Mooij, and H. M. van Noort, *J. Less Common Metals*,125(**1986**) 135
6. K. H. J. Buschow, D. B. de Mooij, and R. Coehoorn, *J. Less Common Metals*,145 **(1988)**601,
7. R. Coehoorn, D. B. de Mooij, J. P. W. B. Duchateau, and K. H. J. Buschow, *J. de Phys*.49(**1988**)669,.
8. R, Coehoorn, D. B. de Mooij, and C. De Waard, *J. Magn. Magn. Mat*.80 (**1989**)101
9. D. C. Hadjipanayis, *J. Magn. Magn. Mater*. 200**(1999)** 373
10. A. Gebert, A. A. El-Monei,, O. Gutfleisch and L. Schultz, *IEEE Trans. Magn*. 38, **(2002)** 2979
11. E. Y. L. Yiu, D. T. S. Fang, F. C. Chu and T. W. Chow, *Journal of Dentistry* 32, **(2004)** 423
12. K. Watanabe and H. Masumoto, *Trans. Jpn. Inst. Met.* 24, **(1983)** 627
13. Wei Zhang, Kunio Tubuta, Parmanand Sharma, Akihisa Inoue, *Journal of Applied physics* 99 **(2006)** 08E914
14. N Li and B. M.Lairson *IEEE Trans Magn* 35 **(1999)**1077
15. N Li, B. M. Lairson and O. H. Kwon *J. Magn. Magn. Mater*. 205, **(1999)**1
16. D. J Sellmyer, C. P Luo, M. L Yan, Y. Liu *IEEE Trans Magn* 37 **(2001)** 1286
17. C. P Luo, S. H Liou, L Gao, Y. Liu, D. Sellmyer *J Appl Phys Letts* 77 **(2000)** 2225
18. Y. Shao, M. L Yan, D. J. Sellmyer, *J. Appl Phys* 93 **(2003)** 8152
19. S. K Chen, F. T Yaun, W. C Chang, T.Chin *J Magn Magn Mater* 239, **(2002)** 471
20. M. L Yan, Y. F Xu, D. J. Sellmyer *J Appl Phys* 99, **(2006)** 08G903
21. W. Zhang, D.V. Louzguine, A.Inoue, *A. Appl. Phys. Lett*, 85**(2004)** 4998

22. W. Zhang, P. Sharma, K. S. Shin, D.V. Louzguine, and A. Inoue, *Scr. Mater.* 54, **(2006)** 431
23. W. Zhang, K. Yubuta, P. Sharma, A. Makino and A. Inoue *J. Appl. Phys.* 101, **(2007)** 09K518
24. P. Sharma, J.Waki, N. Kaushik, D. V. Louzguine, H. Kimura and A. Inoue, *Acta Mater.* 55, **(2007)** 4203
25. H. Zeng, J.Li, J.P. Liu, Z.L. Wang, and S. Sun, *Nature (London)* 420, **(2002)** 395
26. A. Y. Dobin, H. J. Richter, *Appl. Phys. Lett.* 89 **(2006)** 062512
27. Y. K Takahashi and K. Hono, *Scripta Mater.* 53 **(2005)** 403
28. H. W. Zhang, C. B. Rong,X. B. Du, J. Zhang, S. Y. Zhang, and B. G. Shen *Appl. Phys. Lett.* 82 **(2003)** 4098
29. C. B. Rong, H. W. Zhang, R. Chen, S. He, B. Shen *J. Mag. Magn. Mater.* 302 **(2006)** 126
30. A. M. Gabay and G. C. Hadjipanayis *J. Appl. Phys.* 101, **(2007)** 09K507
31. N. Kaushik, P. Sharma, H. Kimura, A. Inoue, and A. Makino, *J. Appl. Phys.* 103, **(2008)** 07E121
32. E.P. Wohlfarth, *J. Appl. Phys.* 29, **(1958)** 595

Chapter 4

Towards Multiferroics : Are Chromites Ferroelectric?

The discovery of ferromagnetic amorphous chromites

4.1 ***Introduction***

Ferromagnetism and ferroelectricity have been studied as independent phenomena for many decades now. If a material contains a ferromagnetic element and has potential for charge disorder on application of electric field, it is a potential ferromagnetic material as well. These kind of materials fall into the category of multiferroics. Very few materials are reported [1] to show this property. In the ever expanding field of spintronics, these materials offer one more degree of freedom to control material behavior; hence they have become an important candidate for investigation. A necessary (but not sufficient) condition for ferromagnetic and ferroelectric coupling is that these materials should be insulating and contain at least one magnetic ion. Rare-earth orthochromites satisfy these conditions very well, so we decided to investigate $YbCrO_3$ and $YCrO_3$ in their thin film form as a potential multiferroic material.

XCrO3 (X=Rare earth elements) are well known materials to study some of the most fascinating and unusual magnetic phenomenon. In general, these are anti-ferromagnetic insulators with a weak canting moment due to Dzhialoshinskii-Moriya interaction [2,3]. Rare earth orthochromites show interesting magnetic properties [4,5] like temperature dependent spin re-orientation induced by a temperature change in $YCrO_3$ [6] which is studied by means of spectral changes of R exciton lines corresponding to the $^4A_{2g} \rightarrow {}^2Eg$ transitions of Cr^{3+} as magnetic symmetry change associated with spin re-orientation is directly reflected in the selection rules of the polarized R exciton lines. They also show a change in direction of easy axis of magnetization from one crystal axis to another on application of magnetic field. When external magnetic field is applied along c-axis, $\Gamma_2(F_xC_yG_z;F_x{}^RC^R{}_y)$ phase changes to $\Gamma_4(G_xA_yF_z;F_z{}^R)$, which has been observed for several orthochromites [7,8].

Since these materials are centrosymmetric in general, hence they should not be ferroelectric. However, there have been claims that rare-earth orthochromites may actually

become ferroelectric [9, 10,11] when fabricated in nanometer dimensions. Materials which are centrosymmetric in bulk form may become ferroelectric in thin films form owing to the epitaxial strain which breaks centrosymmetry [12]. It was thus of interest to fabricated thin films of (Yb/Y)CrO_3 for magnetic and electrical characterization and explore their possible multiferroic properties.

4.2 ***Search for Multiferroic Chromites***:

4.2.1 Preparation of PLD target

4.2.1.1 Preparation of raw powder material

Powder material was prepared at Chemistry division, Bhabha Atomic Research Center, India using combustion reaction. Combustion reaction yields few grams of material within few minutes, which was sufficient to make one PLD target. A combustion reaction employs a fuel material to ignite the oxidants at a particular temperature to produce the reaction products. Since the reaction observes a violent explosion and emission of gasses so the whole reaction was performed in a glovebox with adequate precautions. Oxidants used in our work were Yttrium/Yitterbium nitrate ($Y/Yb(NO_3)_3{\cdot}6H_2O$, 99.9%pure) and chromium nitrate ($Cr(NO_3)_3{\cdot}9H_2O$, 99.9% pure). Glycine (NH_2CH_2COOH) was used as fuel. These reactants were thoroughly mixed in the required molar ratios using a magnetic stirrer. Then the mixture was heated uptill 100°C. On thermal dehydration a viscous liquid (gel) was formed. When this gel was further heated to ≈250 °C, the viscous liquid swelled and auto-ignited, thus producing the powder which was calcinated at 600°C to obtain chemically pure and crystalline product. Due to a fuel-deficient ratio (1:0.5), product was majorly $YbCrO_4$. To obtain $YbCrO_3$ the products were further heated at 800^{o}C for 1 hour. The final powder was indexed on an orthorhombic cell of $YbCrO_3$ with lattice parameters a = 5.193Å, b= 5.491Å and c=7.481Å (Fig: 4.1).

This powder was then used to make a pellet using **Surface Plasma Sintering technique** with the help of Prof. Mats Nygren at the Stockholm University, obtaining as a result 99.5 % dense pellets of about one inch diameter which were used as target for Pulsed LASER deposition (PLD).

Specifications of target pellet:

Diameter = 20.1 mm

Radius= r = 10. 05 mm

Thickness= h = 2.2 mm

Volume = V = лr^2 h =0.6977 cm^3

Mass = m = 5.67 g

Density = m/v =8.126 g/cm^3

Theoretical value= 8.513 g/cm^3

Density is 95, 46% of the theoretical value.

Target pellet was checked again for its crystallographic consistency with chromite and possible contamination with any other phase during sintering (Fig: 4.1).

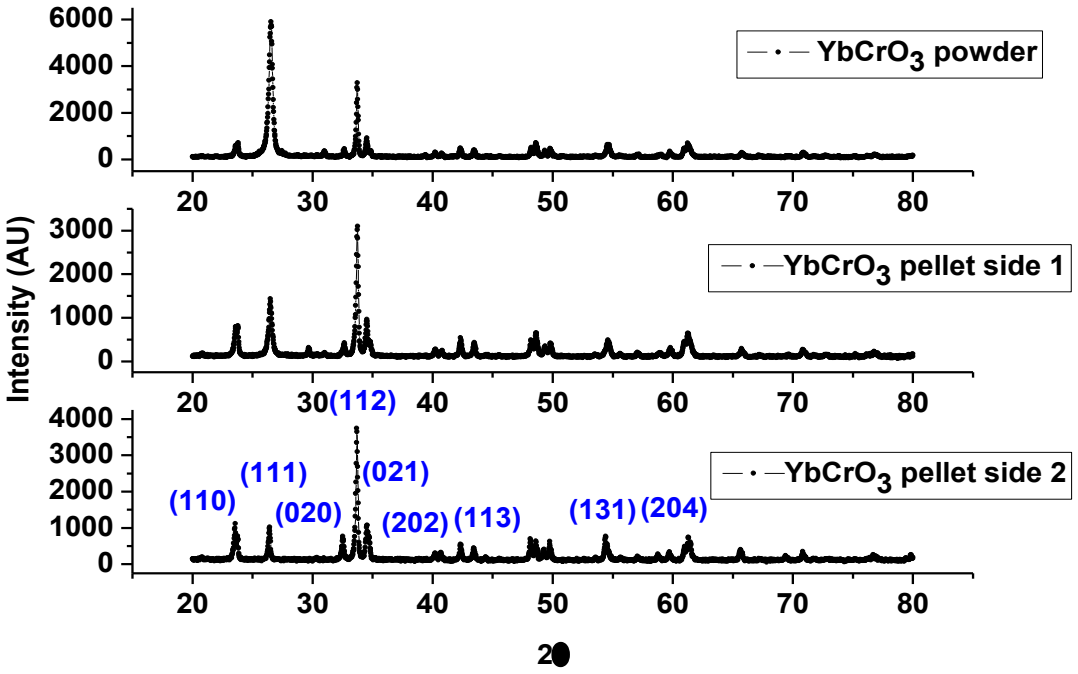

Fig. 4.1 *XRD pattern for pellet and powder shows that during spark plasma sintering, neither crystal structure changes nor any new phase is detected*

Target pellet was further checked for purity using Energy dispersive spectroscopy (EDS) attached to a Scanning Electron Microscope (SEM) and EDS scan at four different spots confirmed absence of any impurity.

	Yb(at. %)	Cr(at.%)	O(at. %)
Spot 1	10.34	9.18	80.48
Spot 2	10.05	9.01	80.94
Spot 3	10.85	8.94	80.21
Spot 4	10.77	8.85	80.38

Table: 4.1 *EDS scan results for detection of elements in atomic percent. Yb concentration is found in slightly more quantity than Cr in each case. Similar observations were found for $YCrO_3$ too.*

4.2.1.2 PLD deposition

Using this pellet, the thin films were deposited by means of PLD. Nd:YAG Laser with UV wavelength of 355nm mode at 10 Hz and energies of the order of 200 mJ per pulse. This energy range was chosen since this produce respectable deposition rate of 8.5 nm/minute. Deposition rate was determined by measuring the cross-section image of a thin film using Focussed Ion Beam (FIB) NOVA 600 nanolab (Fig.).

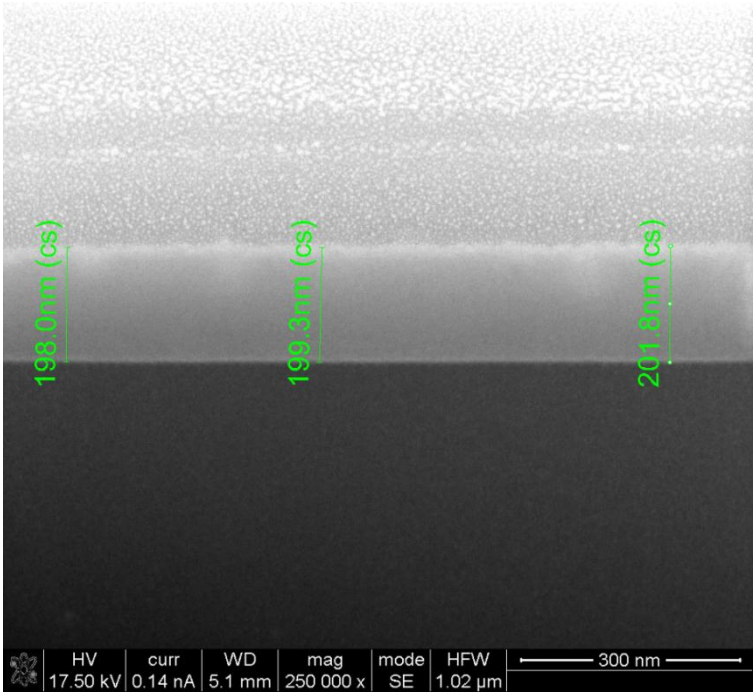

Fig: 4.2 *Crossection of one of the $YbCrO_3$ thin film to measure thickness (~200nm).*

Thin films were deposited in Oxygen and nitrogen atmospheres on silicon, glass and sapphire substrates kept at 300 ^{o}C. Thin films on silicon substrates were used for magnetic characterization and those on glass and sapphire substrates were used for electrical characterization.

4.2.1.3 Structural characterization

Thin films were first checked for their crystal structure using X-ray Diffraction (XRD) technique. This yielded surprising results that deposition conditions yielded amorphous thin films (Fig.). The peak positions for these thin films matched only with the Si substrate.

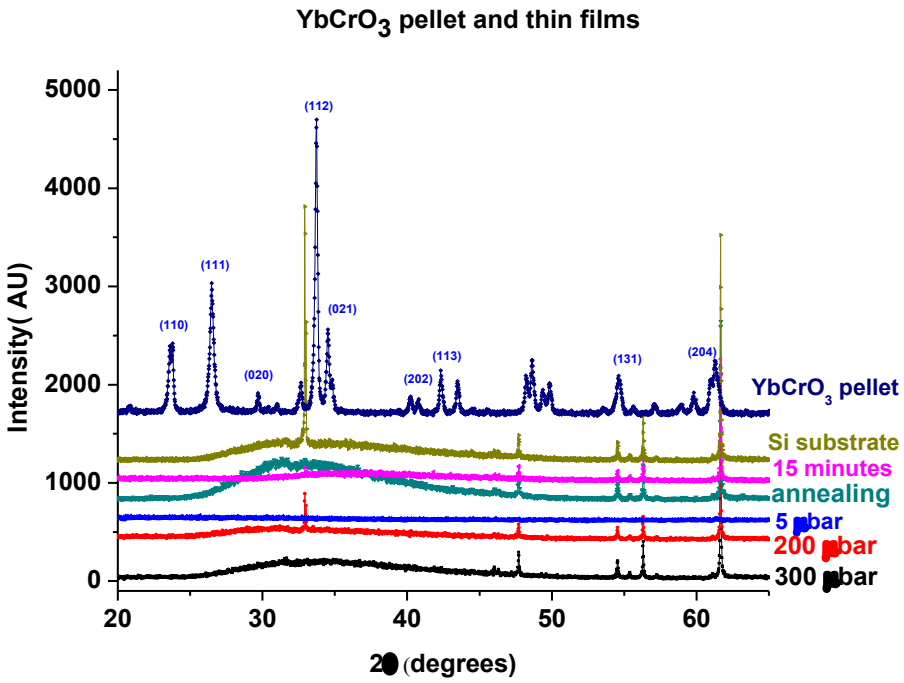

Fig: 4.3 *XRD spectra for pellet and thin films of $YbCrO_3$.*

To verify this, Transmission Electron Microscopy (TEM) imaging was done. FIB was used for TEM sample preparation. First a protective Pt coating was deposited on a suitable area and then using ion beams, a TEM sample was etched out on both sides of coating.

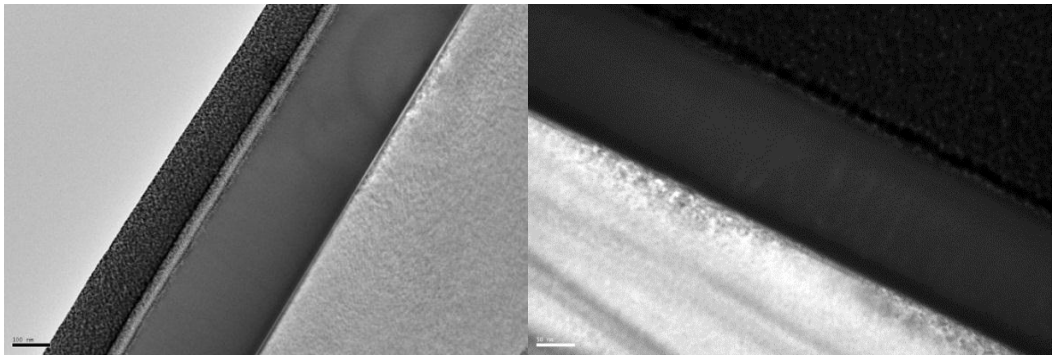

Fig. 4.4 *Cross-sectional view of thin film deposited on silicon substrate. We observe a fairly uniform dense thin film of $YbCrO_3$ sandwiched between Pt coating on one side and Si substrate on the other.*

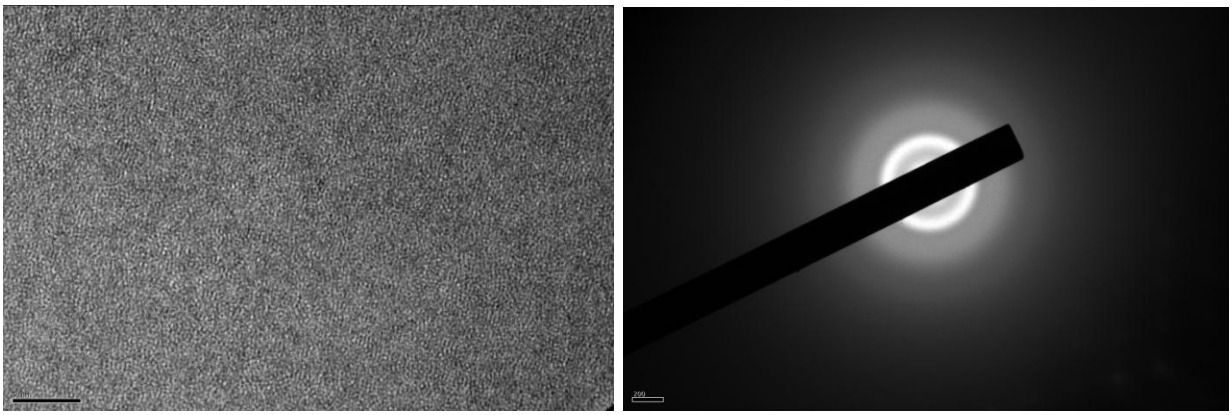

Fig. 4.5 *High Resolution TEM (HRTEM) image and diffraction pattern for this selected area of $YbCrO_3$ thin film showing amorphous structure, which confirms our XRD results.*

4.2.2 Magnetic characterization (discovery of ferromagnetism in the amorphous state)

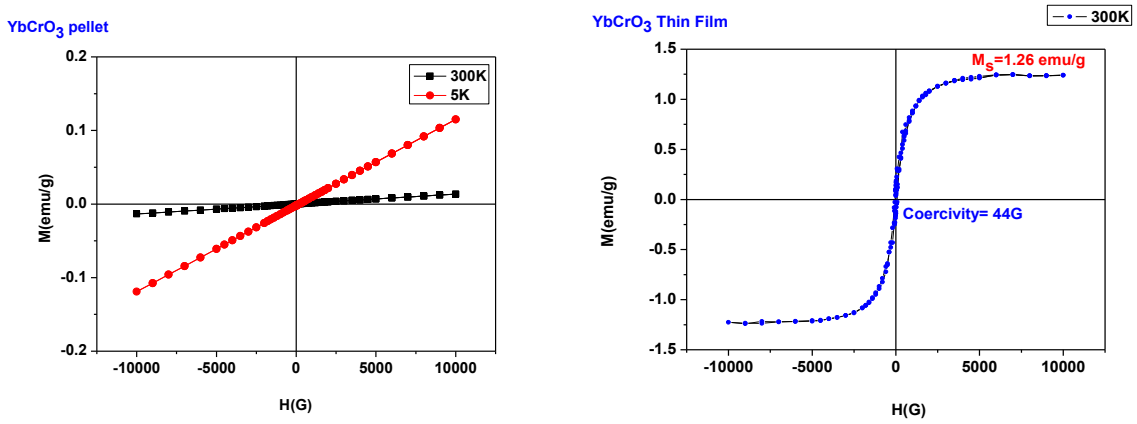

Fig: 4.6 *M vs H curve for a piece of pellet and thin film.*

Magnetic properties (Fig: 4.6) of bulk and thin film material were characterized in SQUID magnetometer. The Bulk material (pellet) showed paramagnetism expected for anti-ferromagnetic (T_N ~150K) as expected for $YCrO_3$ and $YbCrO_3$, but interestingly the thin film showed hysteresis with saturation magnetization of 1.26 emu/g and coercivity of 44G. This is an unexpected robust ferromagnetic behavior. Cr^{+3}-O^{2-}-Cr^{+3} superexchange interactions are known to be antiferromagnetic in nature. This accounts for the anti-ferromagnetism obtained for bulk material. Ferromagnetism in thin film form cannot originate due to strain both since XRD and TEM results shows that they are amorphous. Since Cr^{+3}-O^{2-}-Cr^{+3} superexchange interactions are known to be antiferromagnetic in nature, the origin of ferromagnetic behaviour should be linked to ions other than Cr^{3+}. To find out other ions or different charge states of ions in the material,

we performed XES on this thin film (figure) and found out that the oxidation state of the Cr ion in the thin films is a mixture of Cr^{+3} and Cr^{+4} (Fig.4.7).

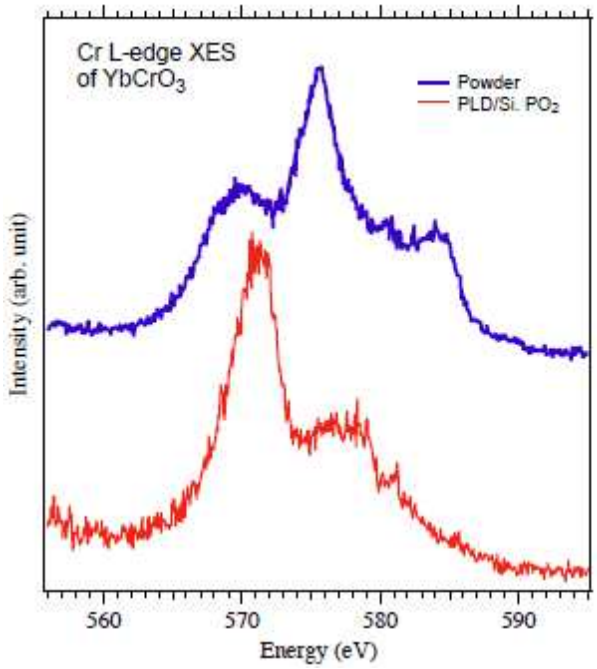

Figure: 4.7 *The XES spectra of the thin films indicates a mixture of Cr^{+3} and Cr^{+4}*

In the case of Stoichiometric (Y/Yb)CrO_3, Cr^{+3}-O^{2-}-Cr^{+3} superexchange interaction makes the material anti-ferromagnetic because the localized d-shell electrons of Cr^{+3} ions align parallel to 2p electrons of O^{2-}. Two electrons in the p orbital of O^{2-} ions are antiparallel hence the spins of Cr^{+3} ions will also be anti-parallel to each other, making an overall anti-ferromagnetic order in the system. This arrangement also requires electrons to be localized, which in turn makes the material an insulator, as is the case for bulk (Y/Yb)CrO_3. Now if there exist a mixed valence state of Cr ions as Cr^{+3} and Cr^{+4} then the picture changes drastically. Now ferromagnetic double exchange interaction [13], where electron hops between two metal ions, comes into picture. Since spin does not change during this hopping, so metal ions can align ferromagnetically. Also the conductivity should increase due to gained mobility by hopping electrons, which was cross-checked during electrical characterization.

One of the possible explanations about why Cr exists in divalent state is that Yb is one of the few lanthanides which can become divalent according to its surrounding ions. Due to

amorphous structure of our thin films, Yb ions can exist in more stable Yb^{+2} valence state, which in turn is compensated by Cr^{4+} to preserve overall charge neutrality.

4.2.2.1 Electrical characterization

Electrically conductive Cu contacts were fabricated on the substrate using sputtering technique and after masking some part of these contacts (this area was used to make contacts to bottom electrodes) as shown in Fig: 4.8

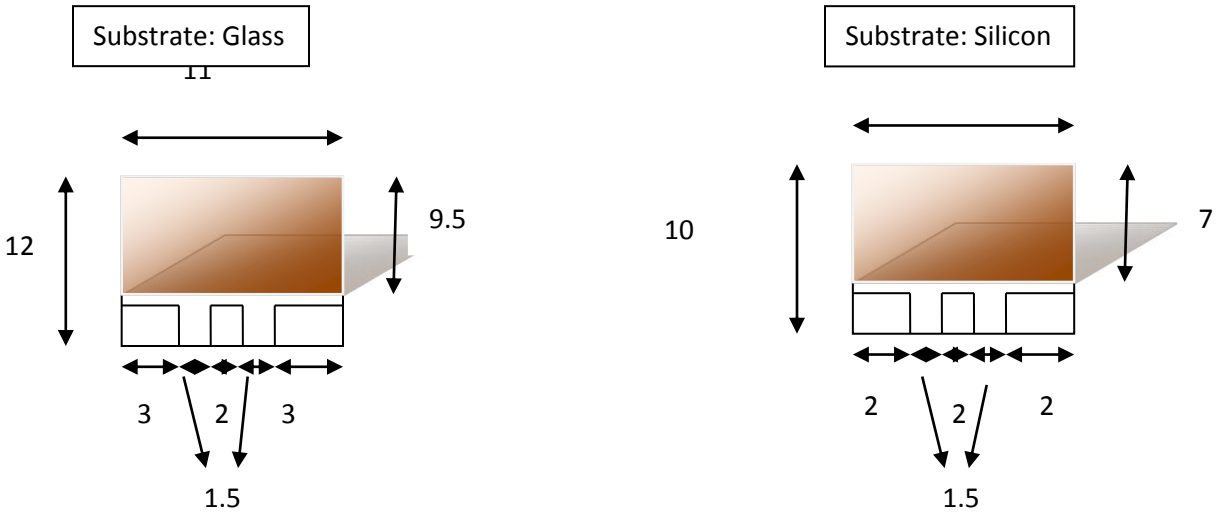

Fig. 4.8 *Electrical contacts for $YbCrO_3$ thin films. Brown colored area signifies the deposited thin film over the bottom electrodes. All dimensions are mentioned in mm.*

Ferroelectric measurements were performed using a Radiant RT6000 ferroelectric tester. Ferroelectric hysteresis loops are usually performed by integrating the total charge flow from one electrode to another, on the application of a suitable voltage to the sample. These kinds of measurements however have one major loop hole. We have to assume that the sample behaves like an ideal insulator so that dielectric displacement and/or ferroelectric switching are the only two possible source of charge flow between electrodes. Since XES measurement indicates towards the existence of Cr^{+3} and Cr^{+4} ions which makes it poor insulator, voltage induced by leakage current will also be integrated by the instrument resulting in ferroelectric hysteresis [14] (Fig: 4.9).

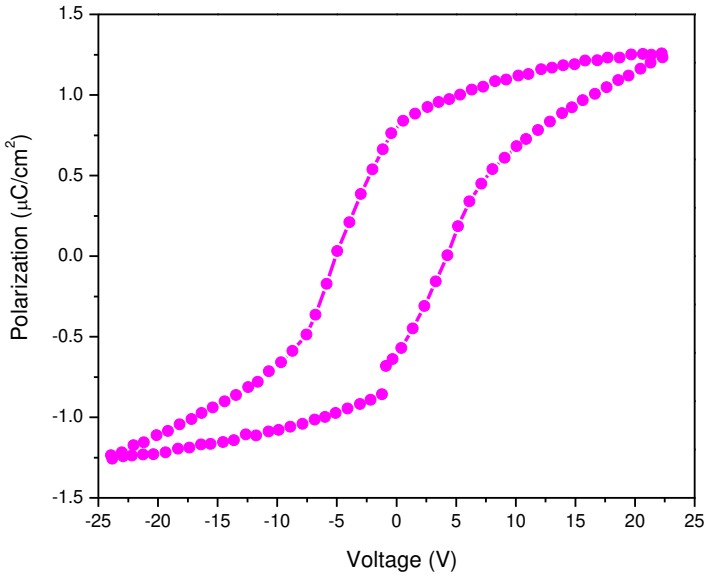

Fig. 4.9 *Hysteresis loop of an $YbCrO_3$ thin film. The shape of the curve is identical to that which can be measured in any genuinely ferroelectric film, yet in our case it cannot be due to ferroelectricity because the $YbCrO_3$ films were amorphous and hence centrosymmetric. Note also that, although the vertical axis is labelled as "polarization", the apparatus actually measures integrated charge, and cannot discern whether this actually comes from true polarization or from leakage currents.*

The total integrated charge in a hysteresis cycle is given by

$$Q = A \times \left(2(P_r + \varepsilon E) + \int_{\tau} I(V)dt \right) = A \times \left(2(P_r + \varepsilon E) + \int_{\tau} \frac{\partial I}{\partial V}\frac{\partial V}{\partial t} dt \right)$$

Where A= Area of electrode, P_r is the remnant polarization (switching polarization), εE is the polarization due to dielectric displacement, and I(V) is the leakage current.

When the current as a function of voltage is non-linear (as may be the case when the two dielectric-electrode interfaces act as back-to-back Schotky diodes), the integrated charge can look very similar to true ferroelectric hysteresis [15]. All testers will automatically label the charge integrated in each half of the hysteresis cycle as $Q/A=P_r$, but note that this is only true if the leakage is zero throughout the entire cycle, which is not true in our case.

There are two ways to check the possibility of this artefact.

- **Ferroelectric Polarization Hysteresis loops at different frequencies**

True ferroelectric polarization switches within a matter of nano-seconds, so the shape of hysteresis is essential time-independent for frequency range (Hz to KHz). But the charge due to leakage current (equation) grows monotonically with the integration period, which should reflect an increase of magnitude of "apparent polarization". This is found to be true in our case (Fig: 4.10). Also the slowest physical cycle at 1KHz show a negative slope in P-E characteristics, which would be completely unphysical if real polarization would contribute to this hysteresis generation, as it would imply negative dielectric constant.

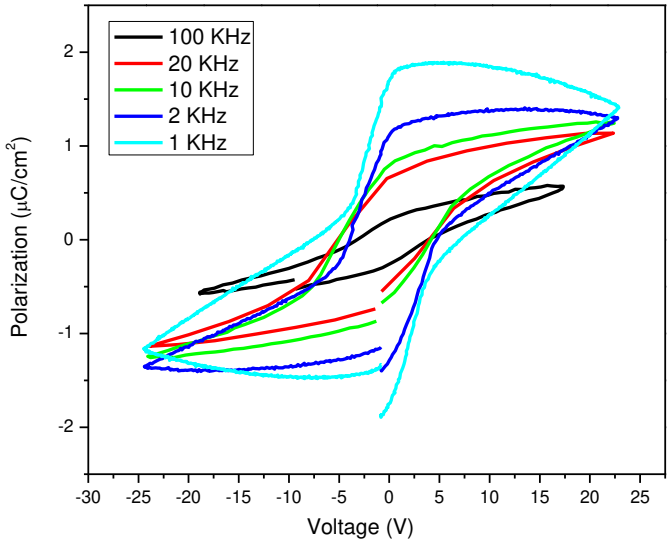

Fig. 4.10 *The size of the hysteresis loops increases as the frequency of the measurement is decreased, clearly indicating that most of the integrated charge does NOT come from switched polarization but from leakages.*

- **Pulsed measurements**:

Pulsed measurements allow separating the switchable from the non-switchable part of polarization and in this way, quantification of the contribution of the real ferroelectricity. PUND (Positive-Up-Negative-Down) works by first pre-poling the sample in the negative direction, then applying two positive and two negative voltages, as shown in schematic diagram (Fig: 4.11).

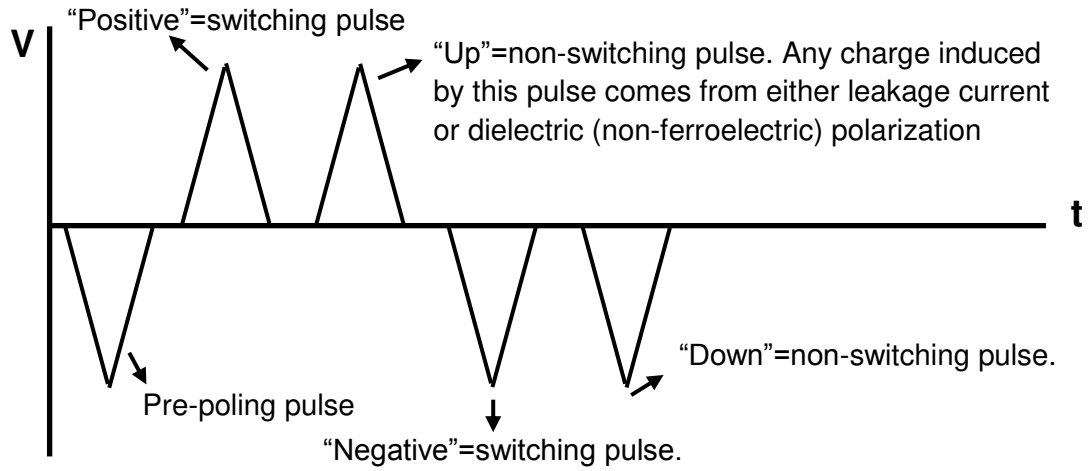

Fig. 4.11 *Schematic of a PUND measurement. Subtracting the charges integrated in the non-switching voltage pulse from those of the switching ones allows quantifying the true remnant polarization.*

The first pulse of each pair is the non-switching pulse which entertains the leakage contribution and the second pulse is the switching pulse since it is free of any leakage contribution and hence results from the real switchable part of polarization. True polarization is obtained by subtracting both of these.

The PUND measurement for the amorphous (Y/Yb)CrO_3 (Fig: 4.12) shows no true ferroelectric contribution, which is consistent with the fact that these thin films are amorphous and hence centrosymmetric. It is evident that the true remnant polarization after the subtraction of the non-switching part is exactly 0 at all voltages.

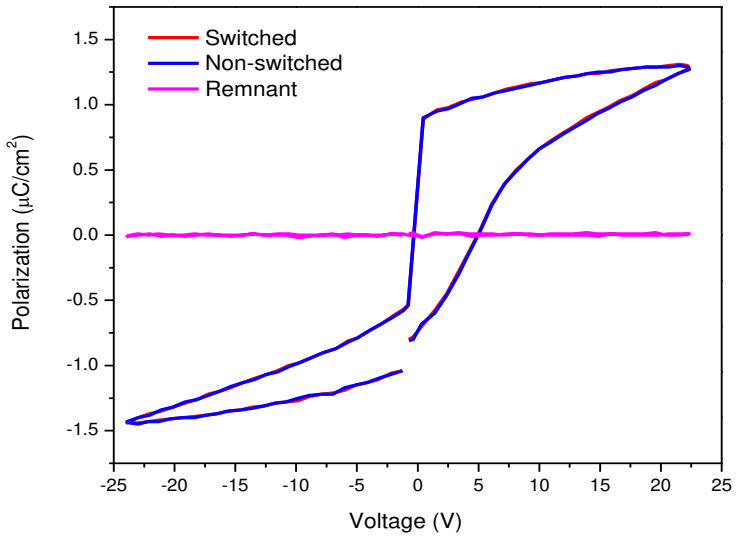

Fig. 4.12 *Pulsed (PUND) measurement of a $YbCrO_3$ amorphous film. Note that when the non-switching polarization is subtracted, there is no real remnant polarization left.*

The results confirms our assertion that hysteresis loop showing ferroelectric (Y/Yb)CrO_3 amorphous thin films are not the true ones, since amorphous material have no global inversion axis and therefore they are centrosymmetric on an average. We investigated this aspect of the study at great length because quasi-amorphous thin films have been shown to display pyroelectric characteristics in right conditions [16] and we wanted to check if our thin films fall under this category truly. Hence we conclude that measuring a hysteresis loop is not sufficient to establish true ferroelectricity.

4.3 Conclusions:

In sum, our present work on (Yb/Y)CrO_3 thin film illustrates that even though we obtain hysteresis-like loop for P-E measurements, this material is not ferroelectric. Careful ferroelectric measurements are essential to find out "true" ferroelectric loops and ascribe them to ferroelectric property of the material. Magnetic and transport properties of (Yb/Y)CrO_3 thin film are directly proportional to the valence state of Cr ions; mixed valence states of Cr as Cr^{3+} and Cr^{4+} leads to ferromagnetism and increased conductivity due to possible local double-exchange phenomenon.

4.4 Future work:

Following experiments can be designed to study multiferroic properties of $(Yb/Y)CrO_3$:

- Non-stoichiometric $(Yb/Y)CrO_3$ can be studied for the effect of concentration of rare-earth element (Yb and Y) and magnetic ion element (Cr) on electronic and/or magnetic properties
- $(Yb/Y)CrO_3$ thin films can be deposited at different deposition conditions (different thickness, temperature, pressures and gas environment in the deposition chamber) to study their growth in crystalline form.
- Present $(Yb/Y)CrO_3$ thin films can be annealed and checked for the same properties to check for the effect of crystallization (first as nanocrystals grown from amorphous material) on electronic and/or magnetic properties.
- Attempts to grow truly multiferroic $(Yb/Y)CrO_3$ will be very useful towards a multiferroic devise fabrication.

4.5 References

1. N. A. Hill, *J. Phys. Chem.*, B104, **(2000)** 6694
2. Shtrikman, S., Wanklyn, B. M., Yaeger, I., *Int. J. Magn.* 1 **(1971)** 327
3. T. Yamaguchi and K. Tsushima, *Phys. Rev. B* 8 **(1973)** 5187
4. Norimichi Kojima, Kunirõ Tshushima, Susumu Kurita, Ikuji Tsujikawa, *J. Phys. Soc. Japan* 49**(1980)**1449
5. R.M Hornreich, *J. Magn. & Magn. Mater.* 7**(1978)**280
6. S. Sugano, K. Aoyagi, K. Tsushima, *J. Phys. Soc. Jpn*. 31 **(1971)** 706
7. M. Kajiura, K. Aoyagi, T.Tamaki, *J. Phys. Soc. Jpn*. 39 **(1975)**1572
8. A.H. Cooke, D.M. Martin, M.R. Wells, *J. Phys. C* 7**(1974)**3133
9. G.V. Subba Rao, G.V. Chandrashekhar and C.N.R. Rao, *Solid State Communications*, 6**(1968)**177- 179
10. C. R. Serrao, A. K. Kundu, S. B. Krupanidhi, U. V. Waghmare and C. N. R. Rao, *Phys. Rev. B* 72 **(2005)** 220101R
11. J. R. Sahu, C. R. Serrao, N. Ray, U. V. Waghmare and C. N. R. Rao, *J. Mat. Chem.* 17**(2007)**42–44
12. J. H. Haeni, *Nature* 430 **(2004)** 758-761
13. C. Zener, *Phys. Rev.* 82 **(1951)** 403
14. L. Pintilie, M. Alexe, *App. Phys. Lett.* 87**(2005)**112903
15. J. F. Scott, *J. Phys: Cond. Matt.* 20 **(2008)**21001
16. D. Ehre, V. Lyahovitskaya , A. Tagantsev, I. Lubomirsky, *Advanced Materials* 19 **(2007)**1515 – 1517

Chapter 5

A New Class of Multifunctional Amorphous Fe-based Films by PLD.
Tailoring Magnetic Bulk Metallic Glasses for Devices

In this Chapter we present studies of a new class soft magnetic, transparent, multifunctional thin films based on $(Fe_{72}B_{24}Nb_4)_{95.5}Y_{4.5}$ bulk metallic glass targets and fabricated by PLD in the thickness regime 5-30nm suitable for applications in MEMS and magneto-optic devices. Outstanding Room temperature Magnetic, optical, electrical, Faraday rotation, and mechanical properties are described.

5.1 Introduction to Bulk Metallic Glasses

Since 1950s, metallurgists have been looking out for non-crystalline alloys in search of improved properties of metals. All crystalline solids have structural order i.e. a well-defined three-dimensional atomic lattice with a space group can be defined. This structural order replicates itself until the three dimensions of the material. Amorphous materials on the other hand lack this long-range order. Thus amorphous materials due to the lack of microstructural features such as grain boundaries, dislocation and stacking faults etc. makes them remarkably different than nanocrystals of same compositions.

Amorphization of an alloy from its liquid state requires kinetic suppression of nucleation and growth from an undercooled melt. The first metallic glass was an $Au_{75}Si_{25}$ alloy manufactured by Klement et.al. [1] in 1960. Rapid cooling of molten liquid at rates close to one mega-kelvin per second, 10^6 K/s, was used to avoid crystallization. This approach enabled scientists to produce metallic glasses in limited number of form like ribbons, foils, or wires since one of the dimensions in these shapes was small so that heat could be extracted quickly enough to achieve the necessary cooling rate. However recently it has been found that in alloys containing more than three elements the rate of cooling can be reduced to as low as to 1 K/s to 100 K/s in fabricating oxide glasses. As the cooling rate became more comfortably achievable, research was driven towards production of metallic glass in "bulk" dimensions and hence the field of Bulk Metallic Glasses (BMG) was born.

Differential scanning calorimetery (DSC), as shown in Fig: 5.1a, is typically used to determine thermodynamics of phase transitions by measuring amount of energy (as heat) absorbed or released by the same during a temperature scan. A differential scanning calorimetery scan of a glass brings out three distinct temperature defined transitions, namely:

1. Melting point (T_m)
2. Glass transition temperature (T_g)
3. Crystallization temperature (T_x)

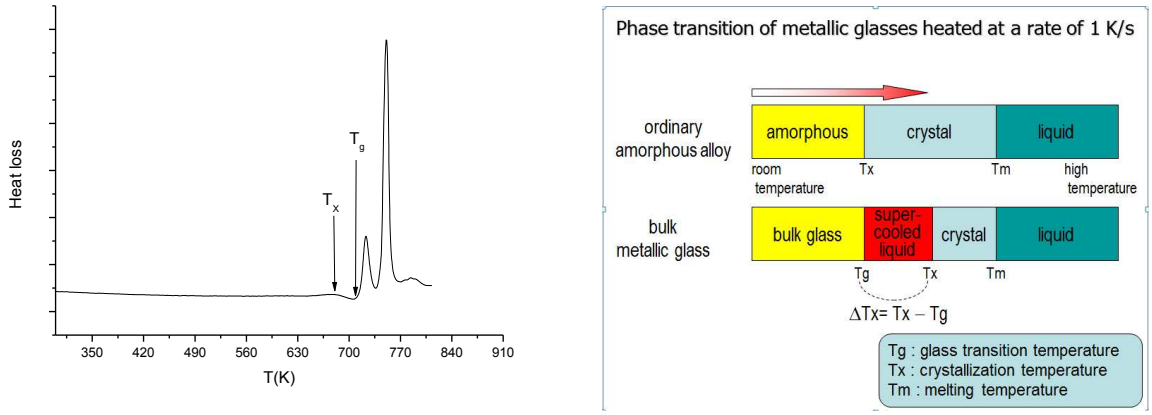

Fig. 5.1 *DSC scan showing distinct T_x and T_g for a glassy system and schematics showing distinction between amorphous and BMG materials.*

As shown in Fig 5.1, ordinary amorphous alloy and bulk glassy materials differ due to a distinct super cooled region i.e ΔT_x is finite. In this region, a material behaves like a super cooled liquid and onset of crystallization is delayed. In this super-cooled region, atoms can be re-arranged and hence physical properties can be tuned, while maintaining non-crystalline crystal structure.

Turnbull [2] emphasized on the reduced glass temperature T_{rg} ($=T_g/T_m$) for an alloy. When it increases from 0·5 to 0·66, the required cooling rate for glass formation decreases, making it possible to synthesize thicker glasses at slower cooling rates. Another parameter ΔT_x ($= T_g-T_x$) has been emphasized by Inoue et. al. [3]. Since it denotes the accessible super-cooled liquid region the larger ΔT_x is, the greater is the glass-forming ability (GFA).

5.1.1. Glassy materials

Glassy materials are those amorphous systems where T_g and T_x are distinctly different so that they show ability of super-cool liquid flow without crystallization. This unique ability makes it possible to fabricate larger sizes and meta-stable phases on crystallization since super-cooled regime allows us to move constituent atoms in desired fashion without crystallization.

Definition of glass transition temperature [4] depends on the time scale of thermal treatment and thermal history of the material. Thermodynamically, T_g is the temperature at which temperature dependence of volume or enthalpy changes. Experimentally, this is determined using caloriemetry by monitoring the temperature at which there is an abrupt change in heat capacity. Another way to define T_g is using kinetic viewpoint. A glass is a low-temperature liquid, which has very long relaxation times exceeding the experimental time scales, and hence Angell [5] defined T_g as the temperature at which shear viscosity is 10^{13} poise.

Early work of Inoue et.al [6-8] led the foundation of BMG research. It has been known for long that heat of formation and atomic size difference of constituent atoms are the key parameters for glass formation. Three empirical rules (Fig: 5.2a) were proposed to make bulk metallic glass (BMG) [9-11]:

1. Multicomponent system should consists of three or more components
2. There should be a significant difference (>~12%) atomic size of constituent atoms
3. Elements should have negative heat of mixing

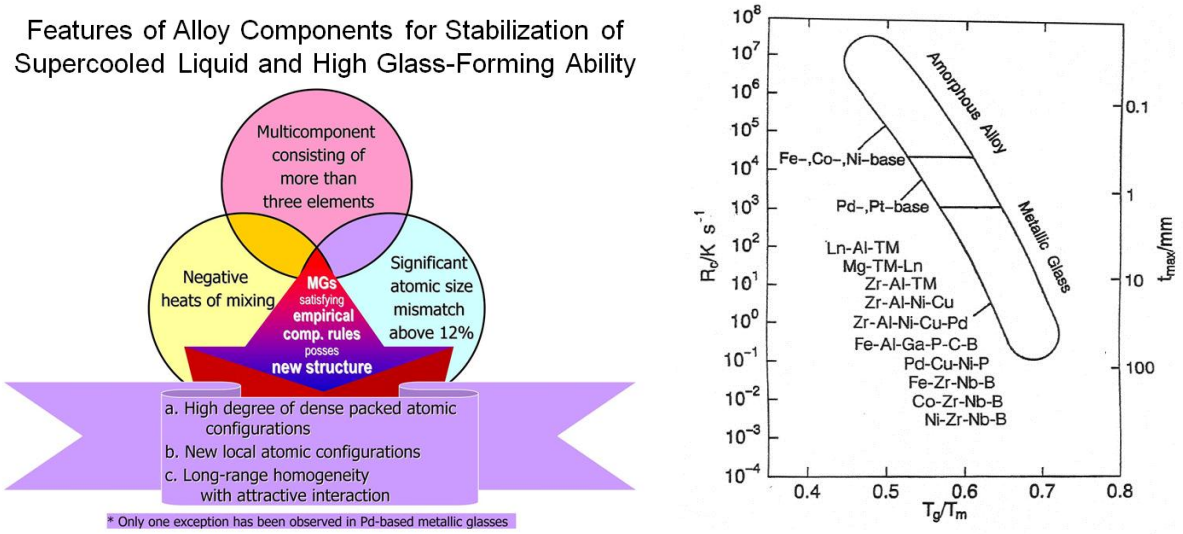

Fig. 5.2. *(a) Schematics illustrating Inoue's empirical rules (b) Diagram illustrating the distinction between amorphous, and Bulk metallic glasses as a function of rate of cooling*

While the atomic mismatch and negative heat of mixing has been obvious to metallurgists fabricating glasses, the importance of multi-component system was recognized particularly for fabricating BMGs. Exploration into the crystal structure of compounds and solid solutions phases reveal that order of structure goes from elementary to binary, tertiary and higher order and the number of new structures diminishes in the same order. Thus, long-range diffusion would be necessary for crystal nucleation in a multi-component system and this can be controlled by introducing multicomponent system because this introduces atomic level strain along with chemical disorder, thus frustrating crystallization.

A variety of Fe, Co, Ni, Cu, Pd, Pt, La, Zr, Mg-based BMGs have been developed using these rules,as shown in Table [4] and Fig 5.2(b)

Base metal	***Physical properties***	
Fe-based	Soft magnetism (glass, nanocrystal) Hard magnetism (nanocrystal) High corrosion resistance High endurance against cycled impact deformation	12-16
Co-based	Soft magnetism (glass, nanocrystal) Hard magnetism (nanocrystal) High corrosion resistance High endurance against cycled impact deformation	17-19
Ni-based	High strength, high ductility High corrosion resistance High hydrogen permeation	20-22
Cu-based	High strength, high ductility (glass, nanocrystal) High fracture toughness, high fatigue strength High corrosion resistance	23-27
Pd-based	High strength High fatigue strength, high fracture toughness High corrosion resistance	28-31
Pt-based	Very low Tg Very low Tl High GFA High corrosion resistance Good nanoimprintability	32

Table:5.1 *Different BMG composition along with thier physical properties*

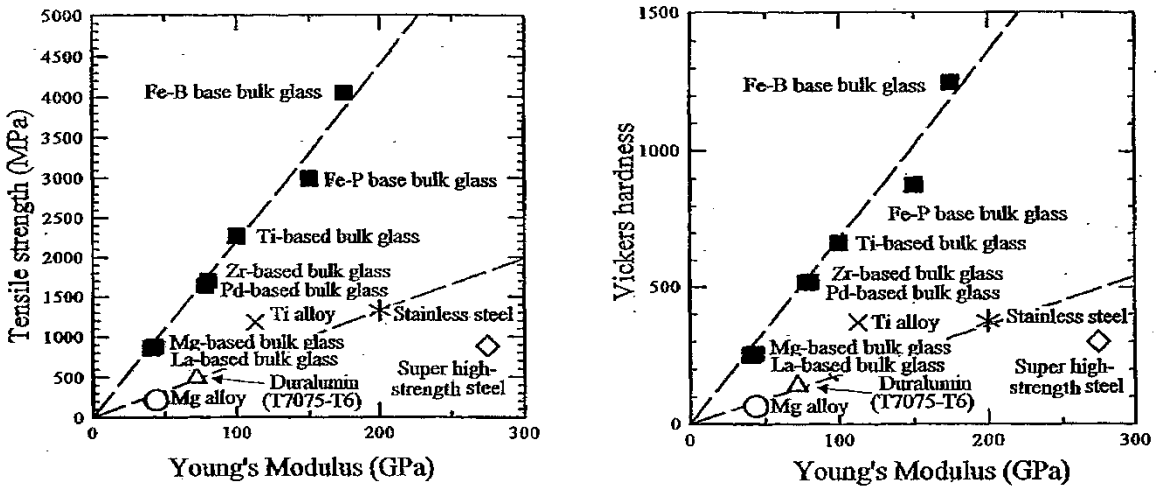

Fig:5.3 *comparison of mechanical properties of glassy versus crystalline materials*

5.2. ***Crystallization and preparation of nanocrystals in bulk forms*:**

Since glassy state is a meta-stable state, hence they crystallize on heating. Herold and Koster [33] classified crystallization phenomenon into three categories:

1. Primary crystallization
2. Polymorphism
3. Eutectic crystallization

In primary crystallization, a crystal of different atomic composition than parent matrix crystallizes. In Polymorphism, a crystal of same atomic composition as the parent matrix crystallizes. In eutectic crystallization, glassy matrix crystallizes in two separate phases according to eutectic reaction.

In the era of nanotechnology, BMGs find an important position because mass production of nanoparticles of specific size and size distribution is possible by simply heating under desired conditions. Also partial crystallization of a BMG results in nanocrystals in a glassy matrix and this has shown to enhance mechanical properties. High corrosion resistance of a BMG is contrary to expectation as they are in a higher energy state. But absence of microstruture (defects, grain boundaries, dislocations etc) and chemical homogeneity provides a very high degree of corrosion resistance. BMGs have also been proposed for unconventional applications such as harvesting low grade heat to generate electricity [34].

BMG can be prepared by water-quenching (alloy is melted in a vacuum sealed quartz tube and then water quenched) based solidification when cooling rate requirements are within the range of 10-100Ks^{-1}. Better results can be achieved by arc melting and then injection molding or suction molding in a copper mould to give specific shape and size. Commercial fabrication of BMGs by companies like Liquidmetal ® Technologies have demonstrated the viable market for these new materials and hence large scale synthesis of BMGs is one of the most active areas of research in present times.

BMG possess superior mechanical strength (Fig 5.3) and anti-corrosive properties, which makes them prospective candidate for replacement in virtually all metal parts of machines (especially those where these properties hold most significance). Soft magnetic and high magnetic moment behavior of Fe- based BMGs has been investigated for their used in electromagnetic systems where heat losses are significant factor in performance of the whole system (like transformer core). Fluery et.al [35] demonstrated application of Fe-based BMG for its application in polymer electrolyte membrane fuel cell owing to their superior anti-corrosion properties. Lee et.al. [36] fabricated ultra-high density phase change storage media using AlNiGd BMG.

A coating of amorphous material on any surface can enhance its mechanical, magnetic, electrical, optical and anti-corrosion properties. Very few reports in this area has come up since most of the work up till now has been concentrated on making BMG in larger dimensions for fabricating machine parts. Alternatively, in our work we emphasized on another approach to improve the performance of a machine part i.e by coating it with an amorphous thin films.

5.3. $(Fe_{72}B_{24}Nb_4)_{95.5}Y_{4.5}$ BMG

Fe-based BMGs have been extensively studied particularly for their magnetic properties. Stoica et.al [37] demonstrated that copper mold casted 2mm diameter rod-type $Fe_{66}B_4Nb_{30}$ material posses soft magnetic properties (1.5 A/m coercivity, due to absence of crystalline anisotropy), high saturation magnetization (105 Am^2/kg) and high thermal stability (31°K of super-cooled region and T_{rg}=0.55) against crystallization (activation energy of 760kJ/mol). This makes it a good experimental system to investigate its applications for soft magnetic components

in electro-magnetic devices. Song et.al [38] demonstrated that addition of Y to Fe-B-Nb system markedly improves the GFA of this composition. Y improves GFA in three ways:

1. Large atomic size difference between Y and B increases the atomic packing density of liquid structure.
2. Y acts as oxygen scavenger and thus suppresses heterogeneous nucleation since Y atom has stronger affinity for oxygen atom compared to other elemts in the system (Y2O3=-1904kJ/mol, Fe2O3=-820.5kJ/mol, B2O3=-1273kJ/mol)

Hence $(Fe_{72}B_{24}Nb_4)_{95.5}Y_{4.5}$ system seems to be better glass than FeBNb system. Bulk samples of diameter up to 2mm diameter have been prepared in these studies [39] but for PLD system, we would need a pellet of at least 1cm diameter. These were cast and produced by our colleague Mr. Ansar Masood while visiting IMR, Tohoku in Sendai, Japan.

5.4. $(Fe_{72}B_{24}Nb_4)_{95.5}Y_{4.5}$ Thin films

Yoona et.al [40] demonstrated that spray coating of Fe-based BMG produced a dense coating of BMG composition on the machine part and markedly improved the wear resistance and showed low friction coefficient. But this method is insufficiently equipped to control the thickness and uniformity of coating. For this purpose, we employ PLD technique. The unique property of stoichiometric preservation is an additional advantage in fabricating $(Fe_{72}B_{24}Nb_4)_{95.5}Y_{4.5}$ thin films in our case since the ratio of elemental constituents is a primary condition for GFA. We used 355nm UV radiation at 100mJ/Pulse as incident light for ablation as this was found to produce a respectable deposition rate of about 6nm per minute. Depositions were performed under 8μBar vacuum and substrates were kept at room temperature. Silicon substrates were used for magnetic measurements, Glass for electrical measurement and quartz for optical measurements. Wang et.al [41] fabricated Zr-Based BMG composition thin films and found that oxidation was a main issue. We have avoided this issue by careful selection of composition of BMG as well as deposition conditions. We also confirmed that properties of BMG thin films did not change over the period of time indicating the absence of possible oxidation. The main motivation of using PLD technique to produce thin films of BMG material is guided by the fact that the superior mechanical properties of BMG materials can be maintained even at thin dimensions and because they are amorphous, patterning and tailoring

architecture made off these films render them valuable materials in NEMs and MEMs applications.

5.5. *PLD deposition*

Thin films from Fe, and $(Fe_{72}B_{24}Nb_4)_{95.5}Y_{4.5}$ targets for 5, 8, 25 and 30 nm thickness were deposited on one side of quartz (1.5 cm^2 area), silicon and glass substrates from the target of same composition. Choice of substrate was judged by the requirements of the various characterization method used i.e silica substrate were used for optical measurements, Si were used for magnetic measurements and Glass substrates were used for electric measurements. All depositions were carried out under similar conditions i.e. Energy=100mJ/Pulse, wavelength=355 nm, Repetition rate=10 Hz, chamber pressure =8 μbar, Substrate temperature= 20°C). Thickness of the thin film was determined by cross-sectional analysis performed by SEM/FIB (Focused Ion Beam, Nova 600 Nanolab, FEI Company) and deposition rate of 6nm/minute was obtained for $(Fe_{72}B_{24}Nb_4)_{95.5}Y_{4.5}$thin films and 10.4 nm/minute for Fe thin. SEM images as well as conductive AFM analysis showed that all thin films are continuous. Some droplets are found on the surface of all the films, which is characteristic of deposition from a metallic target using PLD. Since all deposition conditions were kept same for all thin films, deposition rate was assumed to be constant for particular set of thin films from one target.

5.6.*Characterization*

5.6.1.Structural Characterization

X-ray diffraction (using Siemens D5000 diffractometer employing wavelength of Cu-K_α=1.54Å) study shows a very broad hump close to 25° which confirms the amorphous nature (same as target material) for all $(Fe_{72}B_{24}Nb_4)_{95.5}Y_{4.5}$ thin films irrespective of the substrate (Fig.). On the other hand, Fe thin films were found to be crystalline. Energy Dispersive X-ray spectroscopy did not showe any impurity elements in the PLD target as well as the thin films and verified the presence of all desired elements in right proportion as formulated.

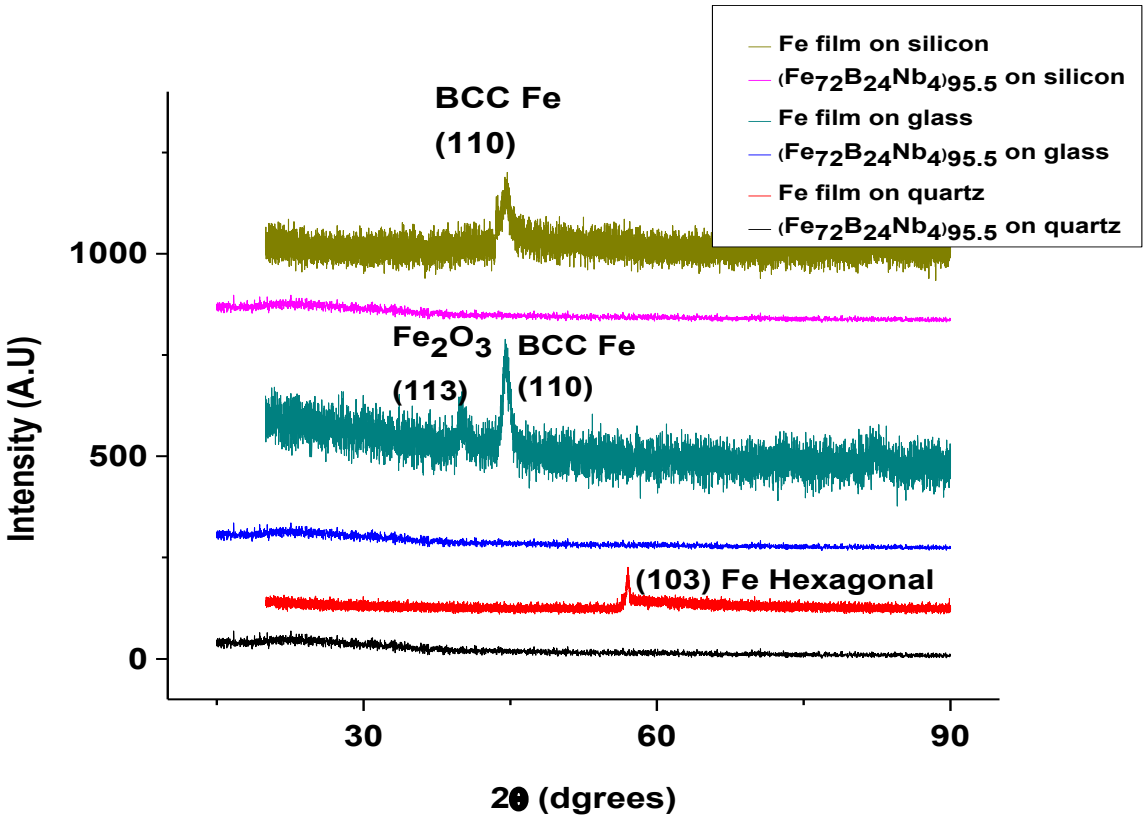

Fig: 5.4 *X-ray Diffraction for Fe and* $(Fe_{72}B_{24}Nb_4)_{95.5}Y_{4.5}$ *glassy composition thin films showing that* $(Fe_{72}B_{24}Nb_4)_{95.5}Y_{4.5}$ *thin films grow amorphous irrespective of the choice of substrate whereas crystalline Fe thin film grow differently on different substrates.*

5.6.1.1. Magnetic properties

Fe based BMG materials cast in form of ribbons, tapes and rods, are found to be soft ferromagnetic with low finite coercivity Hc values. We studied the thickness dependence of magnetization and also the existence of possible consequence of anisotropy due to frozen strains in the films. For magnetization studies of $(Fe_{72}B_{24}Nb_4)_{95.5}Y_{4.5}$ thin films with various thicknesses, we used a Quantum Design MPMS SQUID magnetometer. In our case, all thin films were also found to be soft ferromagnetic (Table 5.2) at room temperature. As expected, saturation magnetization per unit volume is quite independent of film thicknesses (from 9nm to 360 nm) which indicate that magnetization is simply proportional to the amount of Fe in the thin film. Thus mean magnetic saturation moment found for $(Fe_{72}B_{24}Nb_4)_{95.5}Y_{4.5}$ thin films is 372.52 emu/cc (standard deviation =1.08 emu/cc).

Thickness (nm)	M_s@300K (emu/cc)	H_c (G)
9	373.54	6.18
30	373.06	11.3
39	373.45	14.7
51	371.48	24.4
60	372.24	15
90	373.36	11.6
120	370.73	11
180	371.39	33
360	373.43	14.8

Table: 5.2 *Saturation magnetic moments and Coercivity values for $(Fe_{72}B_{24}Nb_4)_{95.5}Y_{4.5}$ thin films of various thicknesses. Saturation magnetization values are almost same for all thicknesses. Thickness independence of saturation values indicate that soft ferromagnetism simply depends on the Fe content in thin films.*

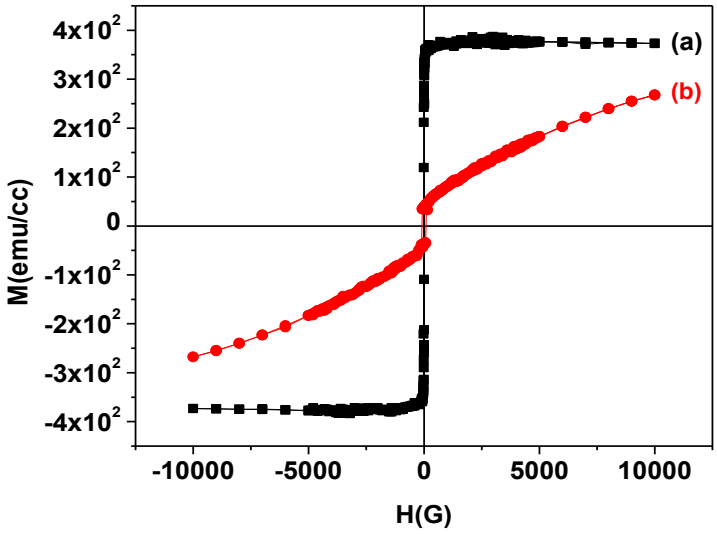

Fig: 5.5 *Hysteresis loop for 30nm thick $(Fe_{72}B_{24}Nb_4)_{95.5}Y_{4.5}$ thin film fabricated on diamagnetic Si substrate in two situations: (a) when magnetic field was directed parallel to plane of thin film, (b) when magnetic field was directed perpendicular to the plane of thin film. This clearly establishes that though easy-axis of magnetization is in the plane of thin film some randomly oriented moments do exist.*

In general, magnetic thin films have been found to have an in-plane easy axis of magnetization and with a demagnetization factor as 1 in out-of plane direction. Also, Sorescu et.al. [50,51,52] had reported that for glassy thin films fabricated using PLD, magnetic moment is sensitive to fluence of LASER energy. Glassy thin films grown at lower fluence develop an in-plane magnetization, intermediate fluence develops a random orientation of magnetic moments and higher fluence develops out-of-plane magnetic orientation. For any practical use in NEMS/MEMs devises, the knowledge of distribution of magnetic moment orientations in $(Fe_{72}B_{24}Nb_4)_{95.5}Y_{4.5}$ thin films is essential. To investigate this, hysteresis loops on these thin films were performed in two orientations: first when magnetic field was directed parallel to the plane of thin film (Parallel geometry) and second when magnetic field was directed normal to the plane of thin film (Perpendicular geometry).

Hysteresis loops in both these geometries are similar irrespective of film thickness which again indicates that magnetic structuture is mostly thickness independent. In case of parallel geometry, a soft magnetic and high saturation magnetization values are obtained indicating that magnetic easy axis is in-plane of the thin film (Fig.). The hysteresis loop in the case of perpendicular geometry shows a complex shape arising from moments which aligns themselves parallel to the field (these moments are perpendicular to plane of thin film) and moments whose easy axis remains in the plane of thin film (as indicated by parallel geometry) and experience a demagnetization factor of 1. This mixed orientation of magnetic moments is consistent with the description of mixed magnetic orientation for intermediate LASER fluence as discussed by Sorescu et.al. [50,51,52]. In our case, laser energy of 100mJ/pulse at 10Hz seems to fall under the intermediate range due to development of random orientation of moments. Hence $(Fe_{72}B_{24}Nb_4)_{95.5}Y_{4.5}$ thin films show a majority of moments with easy axis of orientation directed in-plane of the film but there also exists a small fraction of moments which are aligned out-of-plane of thin film. This mixed magnetic nature is found to be thickness independent which indicates that orientation of magnetic moments depends exclusively on the LASER fluence during deposition.

5.6.1.2. Optical properties

Since these thin films have been found to be ferromagnetic, so we tested them for their transparency. If they can be transparent into a useful frequency regime, they can be used to optical devices, make faraday rotators. Faraday rotators are widely used in telecommunication engineering to manipulate the polarization of light. A transparent ferromagnetic thin film is ideal candidate for such a device and our $(Fe_{72}B_{24}Nb_4)_{95.5}Y_{4.5}$ glassy thin films falls into such a category.

Optical measurements were performed on thin films deposited on quartz substrates, using Perkin-Elmer 900 spectrometer equipped with 150mm integrating sphere detector (spectralon PELA 100) over a wide wavelength range from 300 to 2500 nm. Specular (angle<8°) and diffuse (angle>8°) scattering transmittance (T_{spec} and T_{scat} respectively) and reflectance spectra (R_{spec} and R_{scat}) were measured. The light beam in the spectrophotometer was wider than the sample size. Therefore a sample holder with a black aperture was used in order to minimize the reflection of the incident light by the aperture. The reflection from the empty aperture was measured in separate experiments and was used to make careful corrections to the experimental transmittance and reflectance spectra. The maximum artifacts due to the aperture were found to be of the order 2 - 4 % of the total reflectance spectrum. No significant corrections were necessary for the transmittance data. However, only 50 % of the total light beam was available for the transmission measurements. The optical transmittance spectra T_{spec} and reflectance R_{spec} spectra are used for the subsequent analysis, because both diffuse spectra T_{scat} and R_{scat} were found to be negligible. The reflectance spectra $R_{spec}(\lambda)$ were corrected for errors related to the geometry of the integrating sphere and its ports, by multiplying with a factor 0.96.

5.6.1.2.1. Theory (calculating optical constants) [42]

Three sets of optical functions are used to describe the optical behavior: complex refractive index N, the complex dielectric constant ε and the complex optical conductivity. *N* and *ε* containing this information are related as:

$$\varepsilon = N^2$$

In general, refractive index is useful to study the direction and intensity of light while propagating through a medium while dielectric constant describes the polarization of charges (microscopic effects).

Introduction of real and imaginary parts for $N = n + ik$ and $\varepsilon = \varepsilon_1 + i\varepsilon_2$ gives:

$$\varepsilon_1 = n^2 - k^2$$

$$\varepsilon_2 = 2nk$$

Also, since$|\varepsilon| = \sqrt{\varepsilon_1^2 + \varepsilon_2^2}$, we have

$$n = \sqrt{\frac{|\varepsilon| + \varepsilon_1}{2}}$$

$$k = \sqrt{\frac{|\varepsilon| - \varepsilon_1}{2}}$$

$n, k, \varepsilon_1, \varepsilon_2$ are all dimensionless numbers and they describe the optical properties of a medium.

Since we had a thin film of $(Fe_{72}B_{24}Nb_4)_{95.5}Y_{4.5}$ on a quartz surface, we have to take care about what happens at the interface. Fresnel's equations are used to describe behavior of light at interfaces of two mediums. Considering the following case (Figure), Fresnel's equations are given by:

$$t_p = \frac{T_p}{A_p} = \frac{2N_1 cos\varphi_1}{N_1 cos\varphi_2 + N_2 cos\varphi_1}$$

$$t_s = \frac{T_s}{A_s} = \frac{2N_1 cos\varphi_1}{N_1 cos\varphi_1 + N_2 cos\varphi_2}$$

$$r_p = \frac{R_p}{A_p} = \frac{N_2 cos\varphi_1 - N_1 cos\varphi_2}{N_1 cos\varphi_2 + N_2 cos\varphi_1}$$

$$r_s = \frac{R_s}{A_s} = \frac{N_1 cos\varphi_1 - N_2 cos\varphi_2}{N_1 cos\varphi_1 + N_2 cos\varphi_2}$$

And the two angles φ_1 and φ_2 are related by Snell's law:

$$N_1 sin\varphi_1 = N_2 sin\varphi_2$$

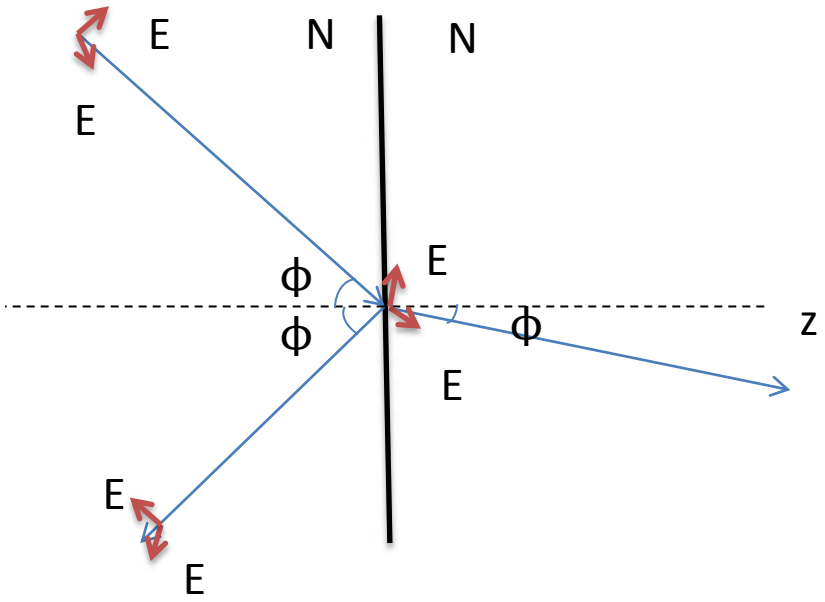

Fig: 5.6 *The incident (i), reflected (r) and transmitted (t) rays decomposed into parallel (o) and perpendicular (s) components.*

Using Fresnel's equations and guessing N, we can simulate transmission and reflectance spectra. This simulated spectrum is then compared with experimental one and optical parameters are obtained by best fit. Next step is to consider oscillator models for the response of charged particles to an electromagnetic wave, which will give us a general expression for optical constants of a solid. This is done by following steps:

- Formulate an equation of motion for one charge particle
- Solve and obtain amplitude of the particle oscillatory motion using boundary conditions
- Use the amplitude and the charge density to express the macroscopic electric polarization of the solid.
- Using the equation: $\vec{D} = \varepsilon_0 \varepsilon \vec{E}$, obtain the dielectric constant from polarization.

The charges can be considered in two distinct ways:

- Bound charges (Lorentz Model) which is more suitable for semiconductors and insulators
- Free charges (Drude Model) which is more suitable for metals.

5.6.1.2.1.1. Lorentz Model

In our case, electrons (charge = -e) are accelerated by the EM wave (light). In our case we are dealing with frequencies$\omega > 10^{12}$, hence strong magnetic moments are too slow to

interact. Since only weak dielectric moments are able to respond to such high frequencies, so only electric field part of this electromagnetic wave needs to be taken care of. Hence only electric force $-e\vec{E}(\omega)$ needs to be considered as the accelerating force. If ω_0 is the resonating frequency, then this electron is bound by a elastic force $m\omega_0\vec{r}$. Inertia $m\frac{d^2\vec{r}}{dt^2}$ and viscous force $m\Gamma\frac{d\vec{r}}{dt}$ also prevent the acceleration.

Hence equation of motion of electron can be written by equating these forces:

$$-e\vec{E}(\omega) = m\frac{d^2\vec{r}}{dt^2} + m\Gamma\frac{d\vec{r}}{dt} + m\omega_0\vec{r}$$

When electron interacts with this electromagnetic wave, it starts interacting at same frequency, hence:

$$\vec{r} = \vec{r}_0 e^{-i\omega t}$$

Solution for displacement of charge will have complex amplitude:

$$\vec{r}_0 = \frac{-e\vec{E}_0/m}{(\omega_0^2 - \omega^2) - i\omega\Gamma}$$

This displacement of charge induces a dipole moment given by:

$$\vec{p}(\omega) = -e\vec{r} = \frac{e^2\vec{E}}{m}\frac{1}{(\omega_0^2 - \omega^2) - i\omega\Gamma}$$

This dipole will oscillate at the same frequency as that of incoming light wave, but in general will be out of phase to the electric field inducing it (due to opposing forces).

If we assume the charge density to be n then macroscopic polarization can be simply written as:

$$\vec{P} = np = \frac{ne^2\vec{E}}{m}\frac{1}{(\omega_0^2 - \omega^2) - i\omega\Gamma}$$

Also the expression for dielectric displacement is:

$$\vec{D} = \varepsilon_0\varepsilon\vec{E} = \varepsilon_0\vec{E} + \vec{P}$$

This gives us "Lorentz model" complex dielectric constant as:

$$\varepsilon(\omega) = 1 + \frac{ne^2}{\varepsilon_0 m}\frac{1}{(\omega_0^2 - \omega^2) - i\omega\Gamma}$$

Since $\varepsilon = \varepsilon_1 + i\varepsilon_2$ hence

$$\varepsilon_1(\omega) = 1 + \frac{ne^2}{\varepsilon_0 m}\frac{(\omega_0^2 - \omega^2)}{(\omega_0^2 - \omega^2)^2 - \omega^2\Gamma^2}$$

$$\varepsilon_2(\omega) = \frac{ne^2}{\varepsilon_0 m} \frac{\omega\Gamma}{(\omega_0^2 - \omega^2)^2 - \omega^2\Gamma^2}$$

Let $\omega_p = \sqrt{\frac{ne^2}{\varepsilon_0 m}}$

when $\omega_p \gg \omega_0$ and $\Gamma \ll \omega_p$, then ε_1 goes through zero.

Once ε_1 and ε_2 are found then n and k can be found using the relation:

$$n = \sqrt{\frac{|\varepsilon| + \varepsilon_1}{2}}$$

$$k = \sqrt{\frac{|\varepsilon| - \varepsilon_1}{2}}$$

Hence by finding appropriate electron density and resonance frequency using other experiments, all the optical constants can be determined.

5.6.1.2.1.2. Drude Model

Drude model is a special case of Lorentz model where charges are not assumed to be bound by an elastic force hence $\omega_0 \to 0$ (also, by convention we introduce $\tau = {}^{1}/_{\Gamma}$ which has dimension of time and termed as relaxation time) which results in:

$$\varepsilon_1(\omega) = 1 - \frac{(\omega_p\tau)^2}{1 + (\omega\tau)^2}$$

$$\varepsilon_2(\omega) = \frac{{\omega_p}^2\tau}{\omega(1 + (\omega\tau)^2)}$$

5.6.1.2.2. Transparency measurements

The measured specular transmittance and reflectance are shown in Fig. for four samples of varied film thickness (5, 8, 25 and 30 nm).The diffuse transmittance and reflectance were also measured, but were found to be negligible. A clear difference is seen in the level and shape of the reflectance curve between the thin 5-8 nm samples and the thicker 26 – 30 nm samples. These curves can be compared with our measurements of R and T for crystalline thin Fe- films, shown in Fig. c and d. It is observed that the amorphous films exhibit a higher transmittance and a lower

reflectance as compared to crystalline Fe films. Basically they have less pronounced metallic character, which is expected in view of their much lower electrical conductivity (Table , Fig.) with negative temperature coefficient of resistivity, when compared to that of iron thin films whose conductivity lies in the range of 1.5 X 10^{-4} Ohm.cm and having a positive temperature coefficient of resistivity.

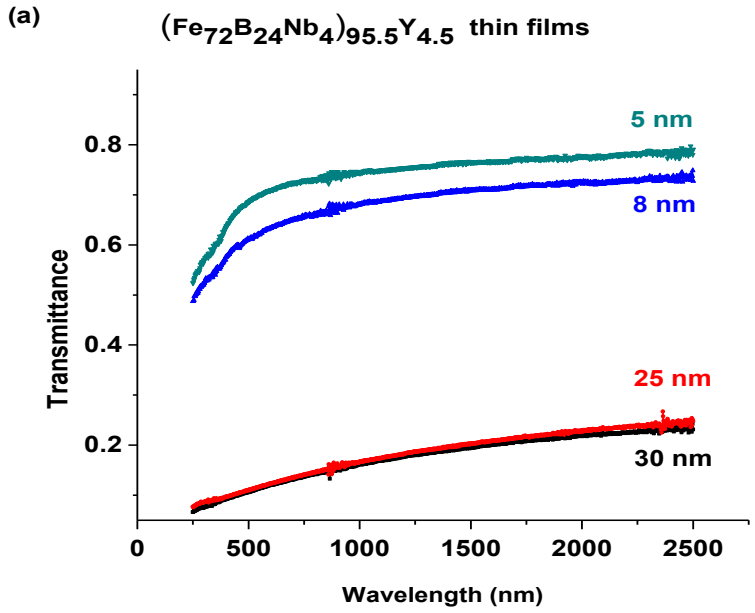

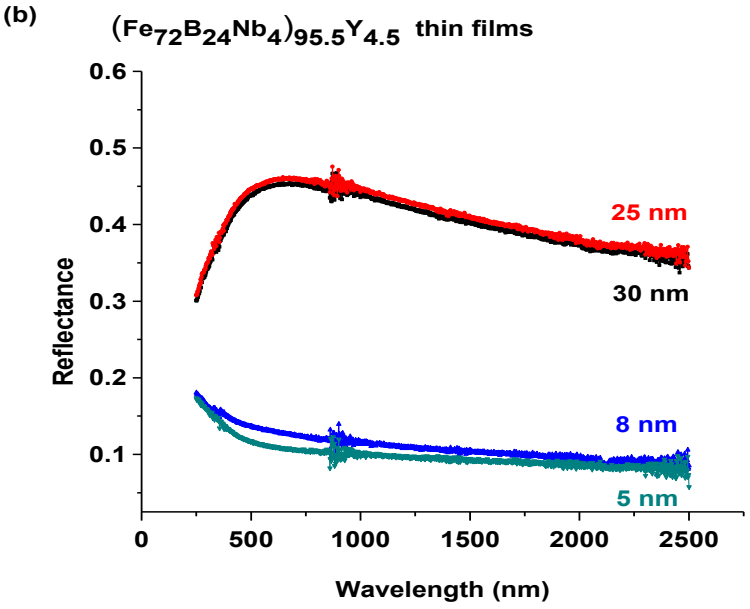

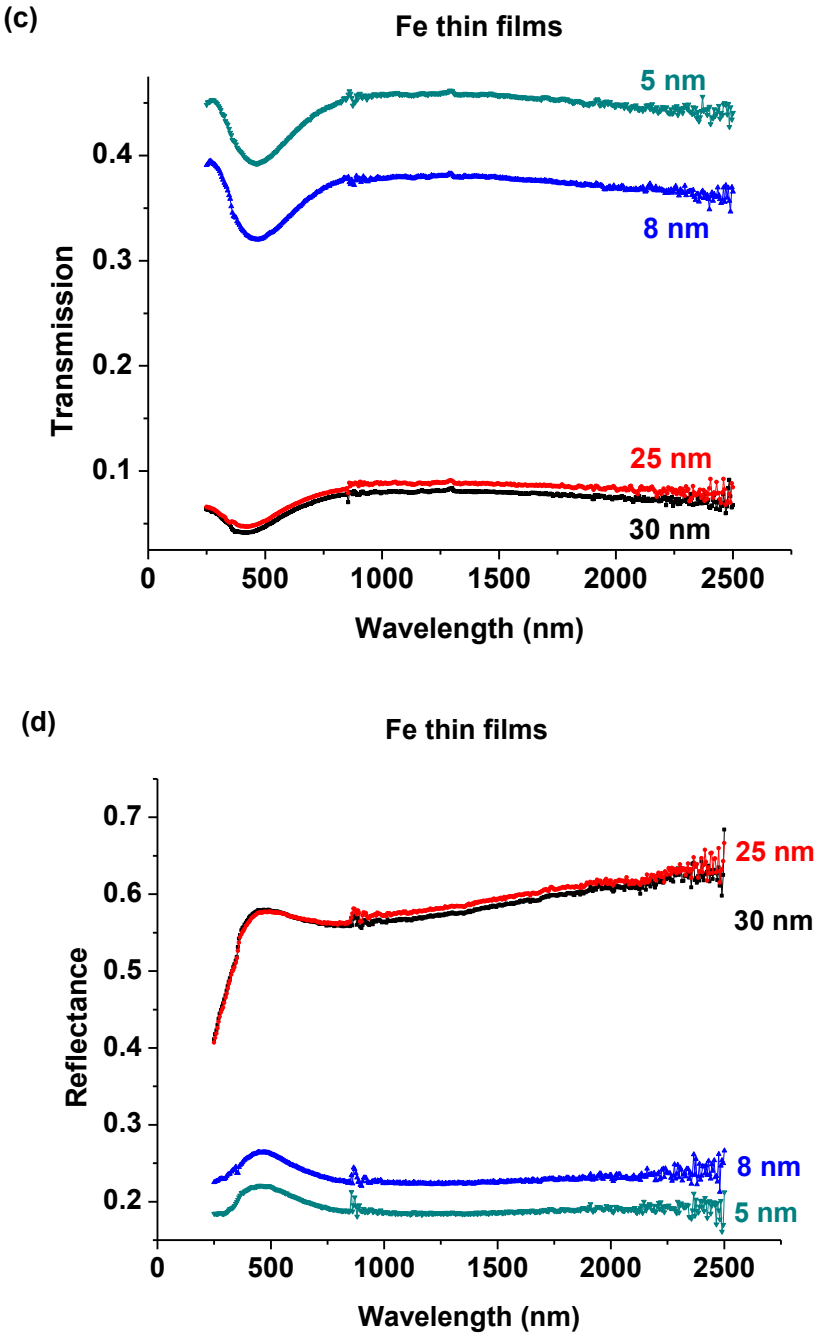

Fig: 51.7 *The measured specular transmittance (a,c) and reflectance (b,d) spectra are shown for $(Fe_{72}B_{24}Nb_4)_{95.5}Y_{4.5}$ films, and 5, 8, 25 and 30 nm Fe thin films on quartz substrate. The kink at 800 nm is due to change of source lamp and hence should be disregarded as an instrument artifact.*

It is also seen that the spectra for $(Fe_{72}B_{24}Nb_4)_{95.5}Y_{4.5}$ thin films appear more smeared out and are more featureless. This can be understood as a consequence of the relaxing of the k-

selection rule for amorphous structures, since this will broaden any sharp features in the spectra coming from interband transitions at special points in k-space.

Using this data wavelength dependence of optical constant ε_2 was calculated (Fig) for both Fe and $(Fe_{72}B_{24}Nb_4)_{95.5}Y_{4.5}$ thin films. Data for Fe thin films are found to match well with data reported in literature. Amorphous films have lower values of this quantity, which means that they are less absorbing, especially the very thin ones. This is in line with the Reflectance and Transmission spectra (fig.) and is connected with the fact that they have a lower electrical conductivity and are not good metals. Another difference is that absorption of the amorphous $(Fe_{72}B_{24}Nb_4)_{95.5}Y_{4.5}$ thin films show pronounced thickness dependence, while the crystalline Fe films do not.

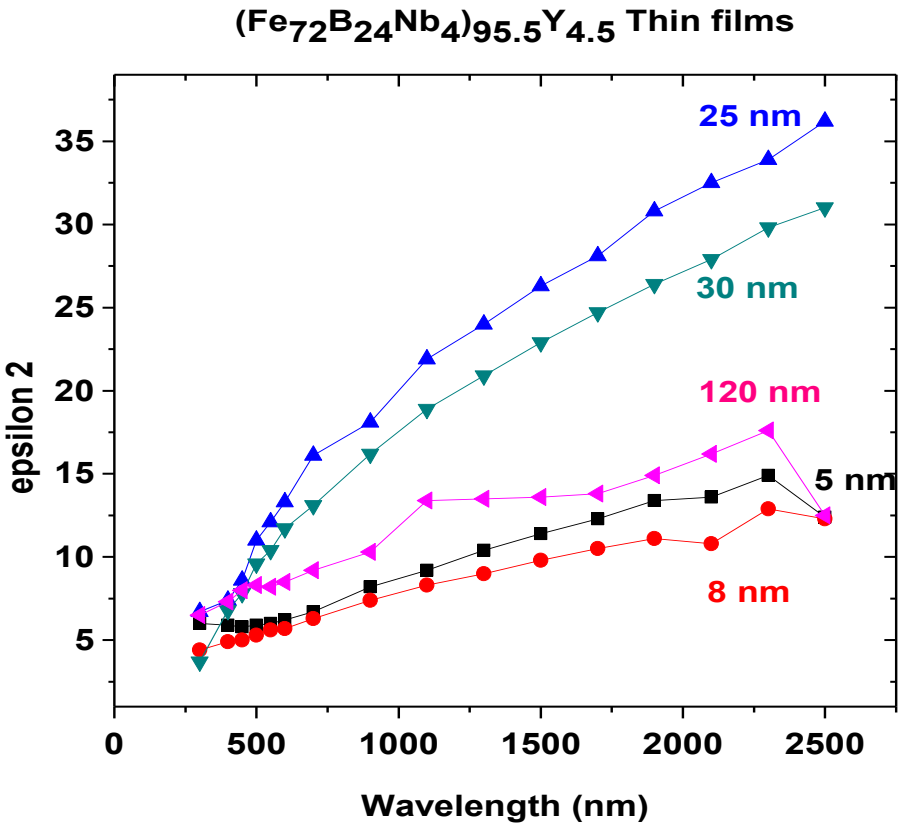

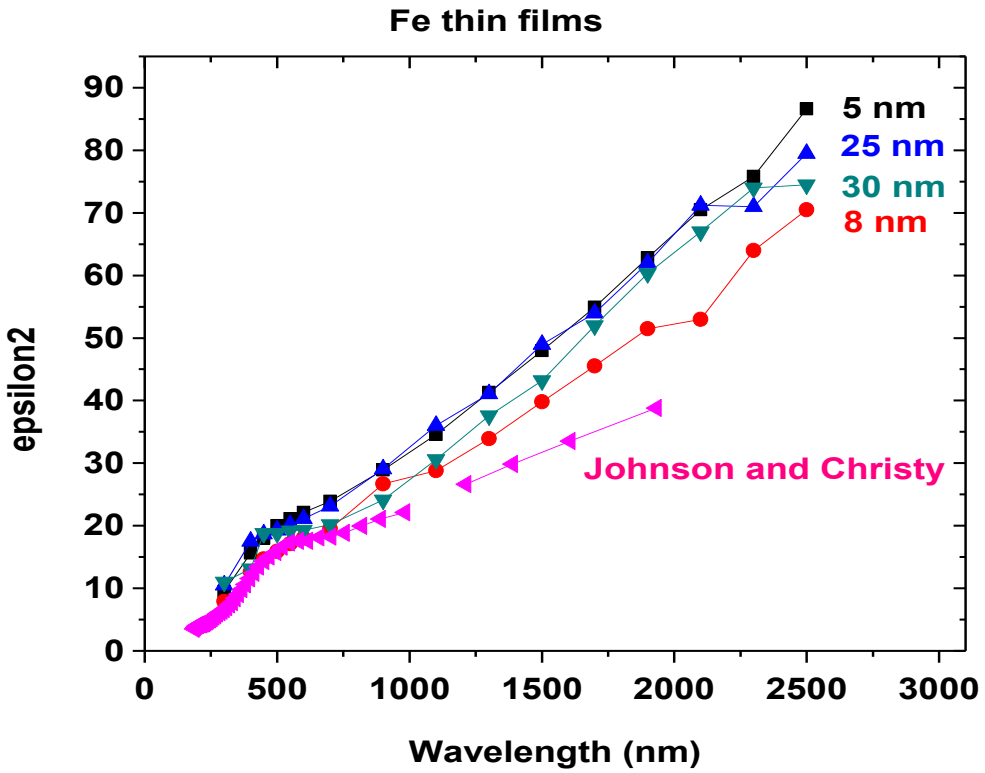

Fig: 5.8 *Optical constant ε_2 calculated for amorphous $(Fe_{72}B_{24}Nb_4)_{95.5}Y_{4.5}$and crystalline Fe thin films for 5, 8, 25 and 30 nm.*

It is nice to recognize that The crystalline Fe films do not show any significant difference in their ε_2 for thicknesses between 5 and 30 nm. The optical absorption is also rather close to available bulk data for the dielectric function of Fe. It is seen that the optical properties of Fe in the UV-Vis-NIR range are dominated by interband transitions, as is the case for most transition metals. Free electron (Drude) absorption, which is expected to be modified by increased electron scattering as the film thickness becomes very thin, does not significantly affect ε_2 for wavelengths below 10 μm. Our data shows that the interband transitions in nanocrystalline Fe are not significantly modified for film thicknesses down to 5 nm.

$(Fe_{72}B_{24}Nb_4)_{95.5}Y_{4.5}$ thin film on the other hand, displays a pronounced thickness dependence which is also seen in the electrical conductivity (Table). The ε_2 is undoubtedly due to interband transitions and attempts at fitting to the Drude function were unsuccessful. Thinner films exhibit lower interband absorption strength, which is a feature that is hard to understand at

present. The shape of the curves is also quite different from those of crystalline Fe, which is not unexpected because of the difference in composition and structure.

5.6.1.3. Magneto-optic measurements

Faraday rotation (FR) of thin films was measured. As seen in Fig., FR loop at 590, 611, 660 nm o not show magnetic saturation indicating that easy axis of magnetization of these thin films is directed in-plane with a demagnetization factor of 1 in out of plane direction. FR of 5nm thick Fe thin film and $(Fe_{72}B_{24}Nb_4)_{95.5}Y_{4.5}$ thin film is similar but 30nm $(Fe_{72}B_{24}Nb_4)_{95.5}Y_{4.5}$ thin film shows higher FR value. 5nm thin film signal is quite low and is prone to errors, hence we shall use data from 30nm $(Fe_{72}B_{24}Nb_4)_{95.5}Y_{4.5}$ thin film for further discussion. FR in the entire visible spectrum shows a maximum of 0.18 degrees (580nm) of rotation for 30nm $(Fe_{72}B_{24}Nb_4)_{95.5}Y_{4.5}$ thin films at 1kOe magnetic field. When compared with conventional materials (Table) which are usually at least some micron thick and includes complex preparations, our technique proves to be simpler one to achieve same results.

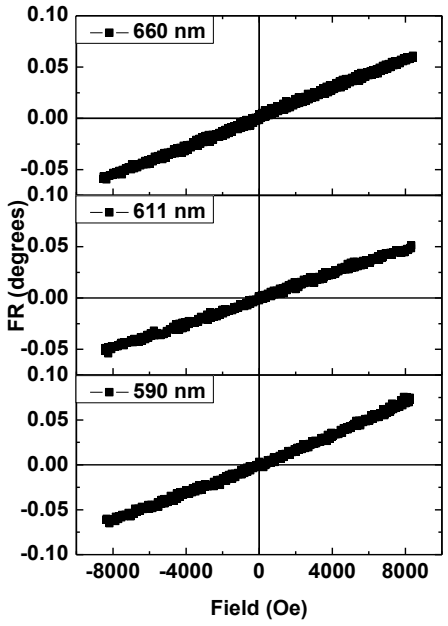

Fig: 5.9 *Faraday rotation curves for 5nm $(Fe_{72}B_{24}Nb_4)_{95.5}Y_{4.5}$ thin film (after removing substrate effect) at 590nm, 611nm and 660 nm*

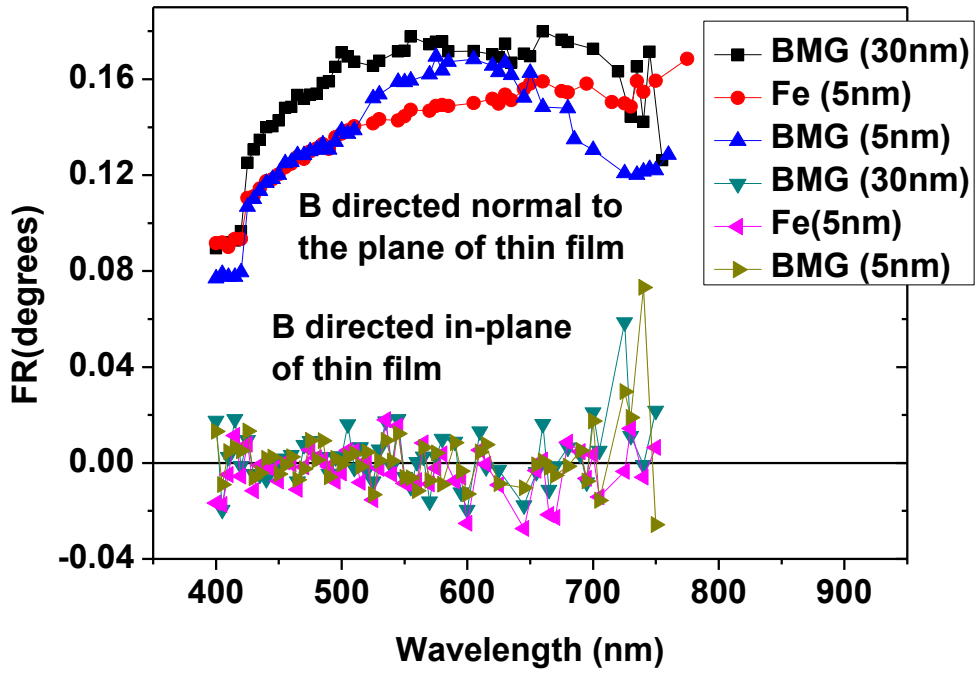

Fig: 5.10 *Faraday rotation versus wavelength at 1kOe magnetic field for* $(Fe_{72}B_{24}Nb_4)_{95.5}Y_{4.5}$ *(BMG) thin films.*

Material	Wavelength (nm)	FR (deg/μm)	Reference
$Ce_{2.2}Bi_{0.8}Fe_5O_{12}$ (1μm)	1550	0.55	[46]
$Lu_{1.619}Y_{0.625}B_{0.683}Pb_{0.064}Fe_{3.842}Ga_{1.144}$ of 7.5 μm	510	4.6	[47]
Magneto-optical photonic crystal composed of stacks of Bismuth Iron garnet and Yttrium Iron garnate (836 nm)	750	6.3	[48]
Bi substituted Iron garnate (1μm)	633	1.5	[49]

Table 5.3 *Faraday rotation parameters for comparable crystalline counterparts to our thin films*

5.6.1.4. *El*ectrical properties

Resistivity of amorphous phase and crystalline phase differ by considerable ratio and this is why, resistance measurements are one of the most important techniques for studying the onset of crystallization. Most of crystalline materials properties are explained using the crystal periodicity. Lack of periodicity imposes a problem to calculate density of state of an amorphous material in a conventional manner. So an alternative approach needs to be devised.

Over the years, literature has been enriched with data from measurement of electrical resistivity, thermo-power and hall coefficient. This indicates the following trends [43]:

- At high temperatures ($T > \theta_D$: θ_D is Debye temperature) properties of amorphous materials are very similar to that of a liquid state.
    - This implies that although conduction electrons cannot be represented by Bloch waves due to lack of translational invariance, they can still be represented by plane waves. This further indicates that "nearly free electron model i.e Drude model" can work in this case.
    - This suggests that amorphous state is a frozen liquid state with a fairly sharp and spherical Fermi surface (energy boundary between occupied and unoccupied states)
- Disorder based anomalies exist:
    - At low temperatures, specific heat has an additional linear temperature dependent term
    - Thermal conductivity has a term which varies as the square of temperature
    - Sound velocity and attenuation have peculiar anomalies
    - Electron mean free path is of the order of atomic distances.
        - Boltzmann transport equations are not valid
        - Possibility of electron localization exist.

Taking clue from electron localization as a result of shortening of mean free path (of the order of atomic distances) Mooji [44] established an empirical conclusion that temperature coefficient of resistivity of alloys with resistivity >150 $\mu\Omega cm$ will be negative.

Electrical resistance of an amorphous material depends on many different parameters like:

- Various scattering process
- Disorder
- Stress relaxation
- Structural relaxation
- Changes in local atomic arrangements
- Remnant crystallinity

Generally, resistivity in an amorphous system is dominated by disorder scattering (100-300 $\mu\Omega cm$), which has a very small temperature coefficient of resistance (TCR) that can be positive, negative or even zero over a part or whole temperature range upto crystallization.

We investigated electrical properties of $(Fe_{27}B_{24}Nb_4)_{95.5}Y_{4.5}$glassy thin films by sputtering four Au-Pt electrodes on top of the thin films and using four probe method. Glassy thin films were deposited on thick corning glass substrates along with the samples used for magnetic, XRD and optical measurements hence the film quality on all substrates is considered to be same. XRD analysis of thick films has already indicated that they are amorphous in nature. Conductive AFM (Fig.) study shows that thin films develop as a continuous media even to very small thicknesses.

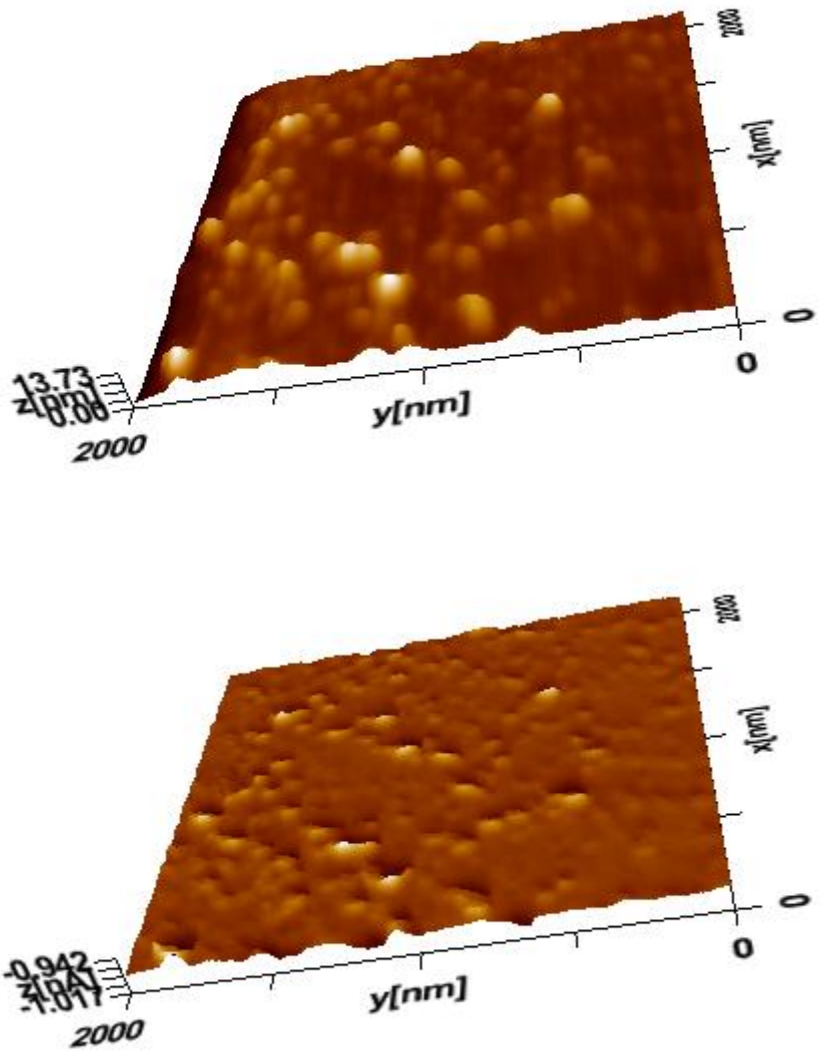

Fig: 5.11 *Conductive AFM (a) topographic and (b) current image for 6 nm* $(Fe_{72}B_{24}Nb_4)_{95.5}Y_{4.5}$ *glassy thin films measured for an area of* $2\mu m^2$*. PLD droplets can be seen in the surface of thin film. Current image shows that the only variation in current profile seen is due to the instrument artifact when tip comes close to a droplet. Table shows the results from electrical measurements on these thin films*

Thickness (nm)	Resistivity (Ohm.cm^{-1})
6	0.134
9	0.138
30	0.016
39	0.016
51	0.017
60	0.015
90	0.017
100	0.012
120	0.023
150	0.067
180	0.099
200	0.115
250	0.113
300	0.112
360	0.114

Table: 5.4 *Results from electrical measurements of* $(Fe_{27}B_{24}Nb_4)_{95.5}Y_{4.5}$*glassy thin films using four probe method.*

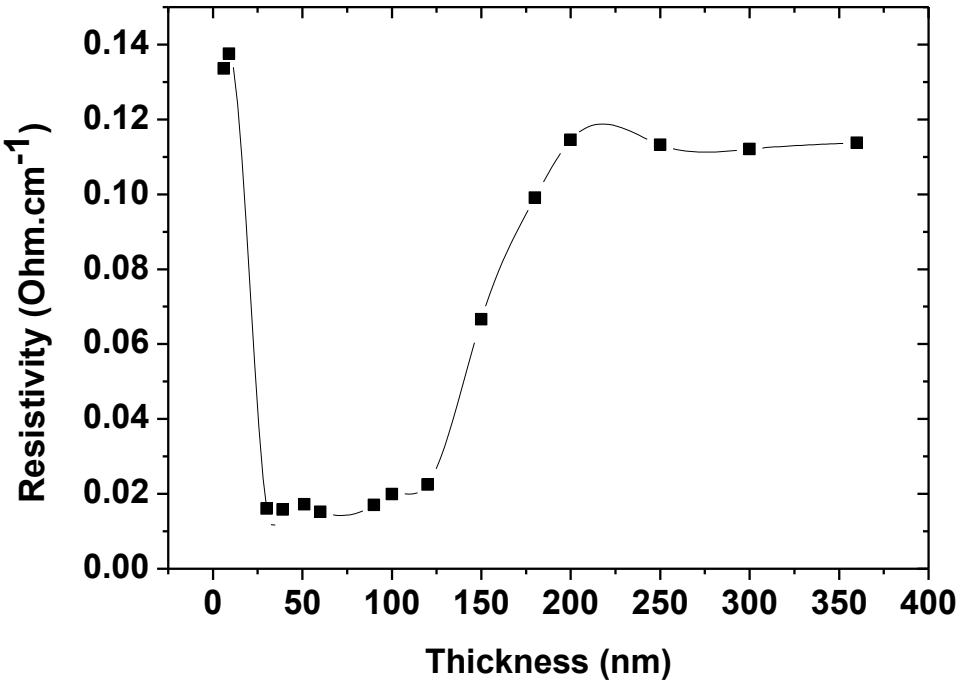

Fig: 5.12 *Resistivity versus thickness for* $(Fe_{27}B_{24}Nb_4)_{95.5}Y_{4.5}$ *glassy thin films using four probe method showing a minima for thickness between 50 and 100nm.*

Temperature dependence of the thin films was performed using the same set up for IV measurements and placing the sample in a cryostat. R vs T curve is fitted to the formula [45].:

$$\sigma = \sigma_0 e^{\left[-\left(\frac{T_0}{T}\right)^p\right]}$$

Where pre-exponential factor may be either independent of temperature or a slowly varying function of T while T_0 is a constant of the material. Values of p determines the conduction mechanism as:

- p=0.25 indicates Mott hopping (M) and
- p=0.5 for Efros-Shklovskii (ES) Hopping mechanism

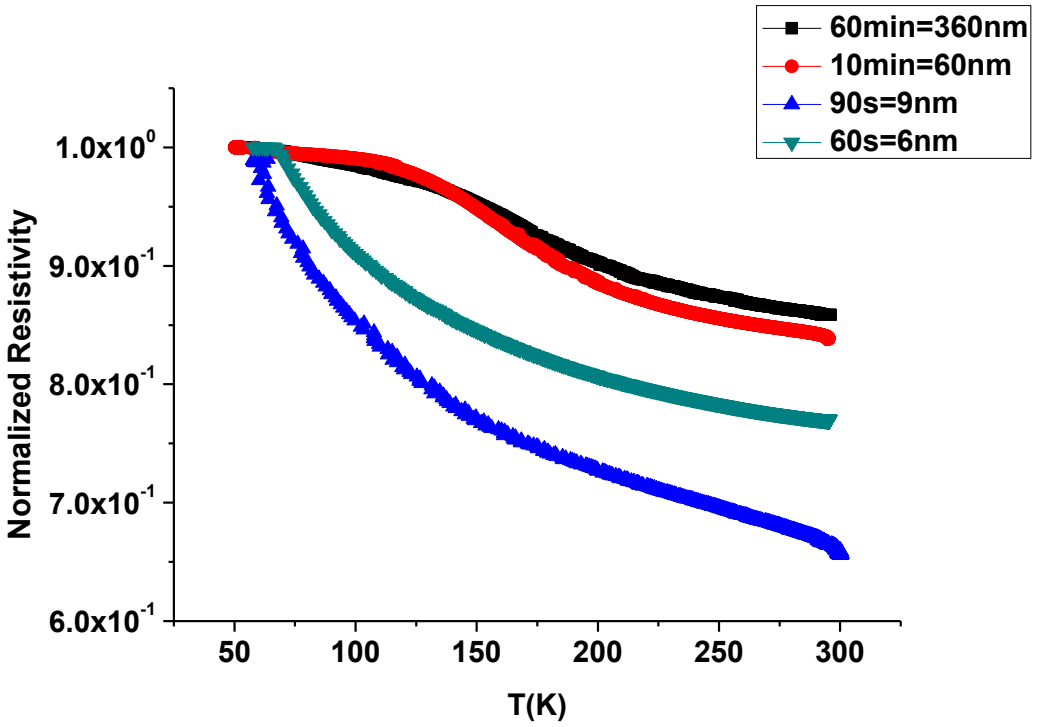

Fig: 5.13 *Normalized resistivity versus Temperature scan for* $(Fe_{27}B_{24}Nb_4)_{95.5}Y_{4.5}$ *glassy thin films measured using four probe method.*

Sample Number	Thickness (nm)	Temperature Range (K)	p	Mechanism indicated
P1004082	6	50-100	0.342	M->ES
		100-293	0.22	M
P1004081	9	54-293	0.22	M
P1003302	60	50-110	0.79185	ES
		110-133	0.526109	ES
		133-211	.199087	M
		211-293	0.33104	M->ES
P1004141	360	51-137	0.58991	ES
		137-293	0.66822	ES

Table: 5.4 Fitting parameters and hopping mechanism involved for various thickness of $(Fe_{72}B_{24}Nb_4)_{95.5}Y_{4.5}$ *thin films.*

5.7. *Summary*

We have successfully fabricated soft ferromagnetic with high saturation magnetic moment, transparent and conductive thin films using pulsed LASER deposition technique. These thin films develop as continuous media even at 6nm thickness and hence present themselves as a potential candidate for base material for NEMS/MEMS architecture as well as other applications like faraday coupler, soft magnetic underlayer, high density recording head core, optical modulator and thin film transformers for integrated circuits. Multi-functional properties of bulk metallic glassy composition thin film when added with its ease of deposition (being amorphous, these thin films can be deposited on a variety of substrate without loss of any valuable property) presents an exciting new area of research and application development for electrical and optical industry.

5.8. *Future work*

Following experiments are suggested for future work with this system:

1. Fabrication of droplet free thin films using various methods as illustrated in chapter 2
2. Fabrication of multilayed GMR and TMR structures using this system. Droplet free thin films will be essential at this stage
3. Fabrication of functional faraday rotator unit using this system.
4. Study of effect of iron content on physical properties especially the effect on faraday rotation and magnetization etc.
5. Fabrication of MEMS/NEMS architectures on these thin films.

5.9. ***References***

1. Klement, W.; Willens, R. H.; Duwez, POL (1960). *Nature* **187** (4740): 869-870. doi:10.1038/187869b0
2. Turnbull D 1969 *Contemp. Phys.* 10: 473–488
3. Inoue A, Fan C, Saida J, Zhang T 2000. *Sci. Technol. Adv. Mater.* 1: 73–86
4. Bulk Metallic Glasses, Michael Miller, Peter Liaw, *Springer,* ISBN 978-0-387-48921-6, Chapter 3, pg. 67
5. C. A. Angell, Science 267 **(1995)**1924–1935
6. A. Inoue, K. Ohtera, K. Kita, and T. Masumoto, Jpn. *J. Appl. Phys. Part 2* 27(12) **(1988)** L2248–L2251
7. A. Inoue, T. Zhang, and T. Masumoto, *Mater. Trans. JIM* 30(12) **(1989)** 965–972
8. A. Inoue, T. Zhang, and T. Masumoto, *Mater. Trans. JIM* 31(3) **(1990)**177–183
9. A. Inoue, *Mater. Trans. JIM* 36(7) **(1995)** 866–875
10. A. Inoue, *Acta Mater.* 48(1)**(2000)** 279–306
11. A. Inoue, *Mater. Sci. Eng. A* 304–306 **(2001)**1–10
12. A. Inoue, T. Zhang, and A. Takeuchi, *Appl. Phys. Lett.* 71(4) **(1997)** 464–466
13. A. Inoue, A. Murakami, T. Zhang, and A. Takeuchi, *Mater. Trans. JIM* 38(3) **(1997)** 189–196
14. B. L. Shen, H. Koshiba, T. Mizushima, and A. Inoue, *Mater. Trans. JIM* 41(7) **(2000)**873–876
15. A. Inoue and B. L. Shen, *Mater. Trans.* 43**(2002)** 766–769
16. A. Inoue, B. L. Shen, and C. T. Chang, *Acta Mater.* 52(14) **(2004)** 4093–4099
17. A. Inoue and A. Katsuya, *Mater. Trans. JIM* 37(6) **(1996)** 1332–1336
18. A. Inoue, B. L. Shen, H. Koshiba, H. Kato, and A. R. Yavari, *Nat. Mater.* 2(10) **(2003)** 661–663
19. B. L. Shen and A. Inoue, *J. Phys.: Condens. Matter.* 17(37) **(2005)** 5647–5653
20. X. M. Wang, I. Yoshii, A. Inoue, Y. H. Kim, and I. B. Kim, *Mater. Trans. JIM* 40(10) **(1999)** 1130–1136
21. T. Zhang and A. Inoue, *Mater. Trans.* 43 **(2002)** 708–711

22. A. Inoue, W. Zhang, and T. Zhang, *Mater. Trans.* 43**(2002)**1952–1956
23. A. Inoue, W. Zhang, T. Zhang, and K. Kurosaka, *Acta Mater.* 49(14) **(2001)** 2645–2652
24. A. Inoue, T. Zhang, K. Kurosaka, and W. Zhang, *Mater. Trans.* 42 **(2001)** 1800–1804
25. A. Inoue, W. Zhang, T. Zhang, and K. Kurosaka, *Mater. Trans.* 42 **(2001)**1805–1812
26. T. Zhang, K. Kurosaka, and A. Inoue, *Mater. Trans.* 42 **(2001)** 2042–2045
27. W. Zhang and A. Inoue, *Mater. Trans.* 44 **(2003)** 2346–2349
28. Drehman A J, Greer A L, Turnbull D *Appl. Phys. Lett.* 41**(1982)** 716–717
29. Inoue A, Nishiyama N, Matsuda T *Mater. Trans. Jpn. Inst. Met.* 37(**1996**)181–184
30. Inoue A, Nishiyama N, Kimura H *Mater. Trans. Jpn. Inst. Met.* 38(**1997**) 179–183
31. Nishiyama N, Inoue A *Appl. Phys. Lett.* 80**(2002)**568–570
32. H. kato, T. Wada, M. Hasegawa, J. Saida, A. Innoue, H.S. Chen, *Scripta Materialia*, 54 **(2006)** 2023
33. Herold U, Koster U The influence of metal or metalloid exchange on crystallisation of amorphous Fe–B alloys. *Rapidly quenched metals* (**1978**) *III* (ed.) B Cantor (London: Metals Society) vol.1, p. 281
34. Peipei Li and Jing Liu, *Appl. Phys. Lett*. 99**(2011)**094106
35. E. Fleury. J. JayarajY.C. KimH.K. SeokK.Y. KimK.B. Kim, *Journal of Power Sources* 159 **(2006)** 34–37
36. Mei Ling Lee, K. Khine Win, Chee Lip Gan, Lu Ping Shi, *Intermetallics* 18 **(2010)**119-112
37. M. Stoicaa,, S. Kumar, S. Roth, S. Ram, J. Eckert, G. Vaughan, A.R. Yavari, *Journal of Alloys and Compounds* 483 **(2009)** 632–637
38. D.S. Song, J-H Kim, E. Fluery, W. T. Kim, D. H. Kim, *Journal of Alloys and Compounds* 389 **(2005)** 159-164
39. Sangmin Lee, AnsarMasood, Takahiko Tamaki, Strom Valter, K V Rao, Akihiro Makino and Akihisa Inoue, *Journal of Physics: Conference Series* , 144 **(2009)** 012074
40. SanghoonYoona, JunghwanKima, GyuyeolBaea, ByungdooKimb, Changhee Lee, *Journal of Alloys and Compounds* 509 **(2011)** 347-353
41. Xinlin Wang, Peixiang Lu, Nengli Dai, Tuhua Li, Changrui Liao, Yanxiao Chang, Guang Yang, Qiguang Zheng, *Appl. Phys. A* 89 **(2007)** 547-552
42. Introduction to Material Optics, Carl-Gustaf Ribbing, Chapter 1, Page 1

43. Amorphous Matallic Alloys, Butterworths Monographs in Materials, Chapter 21
44. Mooij, J.H., *Phys. Status Solidi*, A17 **(1973)** 521
45. A. Ganguly, S.K. Mandal, S. Chaudhuri, A.K. Pal . *Journal of Applied Physics*, 90**(2001)**5652
46. Manda Chandra Sekhar, Jae-Yeol Hwang, Marcello Ferrera, YoavLinzon, Luca Razzari, CatalinHarnagea, Michael Zaezjev, Alain Pignolet, and Roberto Morandotti, *App. Phys.Lett*. 94, **(2009)** 181916
47. L. E. Helseth, R. W. Hansen, E. I. Il'yashenko, M. Baziljevich, and T. H. Johansen, *Phy. Rev. B*, 64 **(2001)**174406.
48. S. Kahl and A. M. Grishin, *App. Phys.Lett*. 84**(2004)** 1438.
49. M. Gomi, T. Tanida and M. Abe, *J. Appl. Phys.* 57 **(1985)** 3888
50. Monica Sorescu, *J. Appl. Phys.* 87 **(2000)**5855
51. M. Sorescu, L. Tsakalakos and T. Sands, *J. Appl. Phys.* 85 **(1999)** 6652-6654
52. M. Sorescu and E. T. knobbe, *Phys. Rev. B*, 49 **(1994)**3253, M. Sorescu, *Jour. Appl. Phy*. 87 **(2000)** 5855

Chapter 6

d^0 Ferromagnetism in Dilute Magnetic Insulators: *DMI undoped MgO, and Vanadium doped MgO*

6-1 Introduction:

MgO is an abundantly used material across many spheres of applications. It is widely used as a refractory material [1] due to its physical and chemical stability at higher temperatures (Melting point = 2852°C). Its medicinal uses are found in drugs for relief of heartburn and sore stomach as an antacid and short-term laxative respectively. It is odorless, which makes it friendlier to work with. An aerosolized solution of MgO is popularly used in libraries for de-acidification of old paper made articles since alkalinity of MgO neutralizes the acidity of paper. MgO has been the interest of study in many fields of research and scientific industry for its dielectric and optical properties. With an electronic band gap of 7.8 eV, it serves as one of the most frequently used insulating material in electronic industry. Since it shows good diffusing and reflectivity, so its used as a reference white color in colorimetry and is used to smoke an opaque material to form an integrating sphere which can be used to study the optical constants of materials [2]. Crystalline solid MgO is transparent from 0.3 to 7μm and has refractive index of 1.72 at 1μm and Abbe number of 53.58. Owing to its high melting point and excellent optical properties, it's used as a protective layer in plasma displays [3]. It is suggested that oxygen vacancies in MgO might improve the energy conversion efficiency in solar cells [4] and open the way for tunable solid-state lasers [5].

It is formed by an ionic bond between a Magnesium and oxygen atom. It is hygroscopic in nature and turn into a hydroxide:

$$MgO+H_2O \rightarrow Mg(OH)_2$$

This reaction can be reversed by heating. Some more physical properties of MgO are listed below:

Molar mass=40.3044 g/mol

Density= 3.58 g/cm^3

Melting point = 2852°C

Boiling point = 3600°C

Solubility in water = 0.086g/L

Band gap = 7.8 eV

Refractive index = 1.736

Appearance = white powder

MgO is widely used in electronic industry as an insulating spacer layer in GMR structures. It is considered to be diamagnetic in idea case. We have investigated the magnetic properties of MgO in view of the recent report about defect based d^0 magnetism.

6.2. *d^0 magnetism*

Magnetism is usually associated with a very narrow region of periodic table i.e *3d* and *4f* series. In these atomic shells, localized magnetic moments are produced due to Hund's rule imposition where same spin electrons are filled up in the shell completely before the spins can be compensated by their opposite spin electrons. Partially filled *3d* and *4f* shell are responsible for magnetism in these elements. It's also important to note that the formation of magnetic moments does not imply a macroscopic magnetic state as this depends heavily on the crystalline structure and other parameters. Apart from conventional metallic magnets, semiconductors doped with magnetic impurities have been recently investigated for their potential use in spintronic applications.

Following the theoretical prediction of Dietl et. al [6], many experimental evidences emerged for room temperature ferromagnetism (RTFM) in transition metal (TM) doped semiconductors [7-14]. Our labs also produced reports for RTFM for a variety of doped semiconducting systems [15-19].

When the dopant ion is magnetic, then magnetism originates from the introduction of dopant but what if magnetism could be generated without a magnetic dopant! Magnetic ordering in undoped oxides is particularly interesting since they provide alternate way to fabricate magnetic materials for spintronic applications with an added advantage of absence of impurity atom/ion

clusters and secondary phases formed by dopants, which sometimes contribute to magnetism of the material.

One such report for insulators was presented by Coey et.al. [20], who found magnetic ordering in insulating thin films of HfO_2 , which was counter intuitive since neither Hf^{4+} (closed shell [Xe]$4f^{14}$]) nor O^{2-} (closed shell[He]$2p^6$) ions are magnetic and d and f shells are either empty or full. This new phenomenon was termed d^0 magnetism. In general d^0 magnets are the class of materials without a magnetic dopant and with open *d* or *f* shells, which should not be ferromagnetic in principle but show the signs of RTFM (room temperature ferromagnetism).

It is well known that two-electron defect centers in oxides (V^0 centers i.e. neutral cation vacancy) do exist in spin triplet ground state or low-lying excited state [21]. Elfimov et.al [22] showed that these V^0 centers in insulating CaO produces a moment of about $2\mu_B$ due to two electrons in orbitally degenerate e_g molecular orbitals, mainly associated with holes on the surrounding oxygen ions, which couple to form a $^3A_{2g}$ triplet state. Coey et. al [23] extended this idea for explaining magnetism in undoped HfO_2 on the basis of impurity band formed by oxygen vacancies (which makes the material n-type) where the associated electrons occupy large Bohr orbitals (hence forming impurity band) where they may be localized by correlations and local potential fluctuations [24] maintaining the insulating behavior (since moment is produced by localized electros and not itinerant electrons). These vacancy generated impurity bands mix with the empty 5*d* states of hafnium (defects) and transfer a fraction of an electron for each vacancy and thus polarize the impurity band providing the necessary ferromagnetic order. From first-principle DFT (in local spin density approximation) band calculations using Ceperly-Alder exchange correlation potential on HfO_2 system, Pemmaraju and Sanvito [12] found that observed ferromagnetism is most likely due to Hf cation vacancies (V_{Hf}) instead of Oxygen vacancies which form high-spin states by coordinating with oxygen p-orbitals. They reported the charge distribution of the HfO_2 cell that gave a better understanding of d^0 phenomenon. Using Mülliken population analysis, it was reported that:

- O atoms in the cell are polarized to different degrees depending on their orientation and distance relative to the vacancy site but always with the same sign
- Hf atoms in the cell are also polarized but importantly, the sign of polarization is opposite to that of the O

- Total polarization of all the O atoms in the cell is 3*:*92μ_B and that for the Hf atoms is 0*:*40 μ_B, leaving a moment of the cell of 3*:*52 μ_B.
    - This suggests that the magnetic coupling between the O atoms in the cell is mediated by minority-spin electron delocalization across the Hf bridge connecting the O atoms. This applies also to O atoms belonging to two different V_{Hf} sites. The delocalization is larger when local moments on the two V_{Hf} are ferromagnetically aligned, resulting in lower kinetic and exchange energies relative to the antiferromagnetic case.

So it is safe to conclude that oxygen and/or Hf vacancies play a role in d^0 magnetism shown HfO_2 and similar logic applies for other set of oxide semiconductors and insulators. Magnetic impurities are a major issue when dealing with d^0 magnetism since small amounts of magnetic impurities can show similar moments and thus system under study should be checked for its impurity free status.

Sundaresan et.al. [25] studied CeO_2, Al_2O_3, ZnO, In_2O_3 and SnO_2 and argued if d^0 magnetism is a universal feature of nanoparticle systems which are otherwise diamagnetic in their bulk state! The defects at the surface of nanoparticles (especially oxygen vacancies) are known to trap electrons (similar to what Coey et.al [23] explained as impurity band by V^0 vacancies) which are polarised. These results from thin films as well as nanoparticle powder systems indicate a defect-mediated d^0 magnetism mechanism for otherwise diamagnetic bulk oxide insulators and semiconductors. Based on these explanations, a variety of other reports were published for a new class of ferromagnets and half-metallic materials [22] based on d^0 magnetism in a range of materials [26,27]. These undoped systems will be a suitable choice for fabricating future spintronic materials and devises since they do will not show complications which arise from additional phase and clustering effects, which presently limit their use under particular chemical and physical boundaries.

Ohno etl.al. [28] commented that carrier mediated and RKKY like interactions, can explain ferromagnetism in insulating configuration since near metal-insulator transition, the localization length does not extend to whole sample size (atleast millimeters) but it can be longer than that required for magnetic interactions (nm) leading to RKKY interactions. This further confirms the results of nanometer sized system showing ferromagnetic order, as reported by Sundaresan et.al. [25].

Amidst the reports of ferromagnetism in otherwise diamagnetic systems, it is obvious to doubt the results that seem too good to be true! The very first experimental artifact can arise from the tiny amounts of magnetic impurities. Abraham et.al [29] warned that using stainless steel tweezers can induce iron impurities, which could account for magnetism in these systems but Coey et.al [23] verified the amount of impurities as Mn=3ppm, Fe<1ppm, Co=3-4 ppm and Ni<1ppm and thus ruled out production of large magnetic moment from these impurities. They also verified that straw and substrates used in squid measurements were also impurity free. Sundaresan et.al. [25] also confirmed that chemicals used for making ferromagnetic CeO_2, Al_2O_3, ZnO, In_2O_3 and SnO_2 nanoparticles were free of any magnetic impurity. So it is safe to assume that experimental evidence of d^0 ferromagnetism in thin films and nanocrystalline power does not originate from impurities, but it should be checked rigorously for the same, for any new system which should be studied.So to conclude there exist two distinct classes of d^0 magnetism [30]:

1. Undoped oxides and nitrides

Compound	References
CaO	22
HfO_2	12,20
TiO_2	31-34
ZnO	35, 36
SnO_2	37,38
GaN	39,41
CeO_2	42
CuO_2	43
MgO	44-47

Table: 6.1 *List of undoped oxides and nitrides showing d^0 magnetism*

*Fo*r this class of d^0 magnetic materials, cation vacancies may be responsible for the ferromagnetism.

2. Oxides doped with 2p light elements such as C or N-doped:

Compound	References
ZnO	48-51
SrO	22
MgO	52,53
TiO_2	54-56

Table: 6.2 *List of oxides doped with C or N, which show d^0 magnetism*

In this class of materials, substitutional dopants (C- or N substitutes for Oxygen) can produce holes in dopant 2p orbitals which provide local magnetic moment.

6.3. *d^0 magnetism in MgO*

MgO is a widely used oxide insulator and commercial optical material. In late 80's, Stoneham et.al. [47] predicted that neutral Mg vacancy induces large magnetic moment on neighboring oxygen atoms and this has been studied recently too [44-46, 57]. But further work in this regard did not exist in literature. As mentioned before, various semiconducting and insulating oxides have been reported to show RTFM so we decided to study MgO for d^0 magnetism phenomenon in the similar manner as reported above, for both thin film form and powder form.

We chose MgO system because it's widely used in electronic and optical industry. Also it's quite economical compared to other oxide insulators which have been reported for d^0 ferromagnetism. Its wide use in magnetic tunnel junctions (which proved to be a quantum leap in magnetic data storage) makes it an attractive candidate for study of d^0 ferromagnetism. A magnetic insulator spacer layer can couple the two ferromagnetic layers between which it's sandwiched, in a desired fashion and thus giving better control over tunnel junction properties. Theoretical prediction [58,59] of Giant magneto resistance (GMR) effect for Fe/MgO/Fe and its experimental [60-61] confirmation signifies the importance of magnetic MgO layer for electronic industry in coming times. Ohno etl.al. [28] fabricated (Ga,Mn)As/(Al, Ga)As/(Ga,Mn)As GMR

structure and signified the critical role of holes in the spacer layer for efficient ferromagnetic coupling of sandwiching layers. It was found that oxygen vacancies lower the energy barrier for tunnel current and thus significantly altering the performance of whole structure and signifying the importance of defect states in spacer layer for GMR configuration.

It must be noted that ferromagnetism has already been predicted for MgO doped with non-magnetic (C) dopant [10] and it has already been observed experimentally with magnetic dopants (Ni and Co) [62] and in undoped form as powder [46] and thin films [63]. Fabrication of MgO thin films using PLD provides an alternative fabrication technique for thin films and in some cases easier (to control surface uniformity, roughness, thickness and faster deposition rates) way to control deposition parameters.

6.4.*Ab initio calculations*

Droghetti et.al. [57] highlighted the issue of sensitivity of theoretical results upon the subtle interplay between covalency and Hund's coupling. Importance of including coulomb potential into the calculation was found to be very important to obtain delocalization which leads to magnetic ground state. These concerns were duly taken into consideration while performing theoretical calculations for this work.

A 3x3x3 supercell made up of 216 atoms ($Mg_{108}O_{108}$) in MgO rock salt structure was used for *ab-inito* calculations and following intrinsic defects were studied.

- oxygen vacancy (V_O),
- oxygen interstitial (O_i),
- oxygen antisite (O_{Mg}),
- magnesium vacancy (V_{Mg}),
- magnesium interstitial (Mg_i)
- magnesium antisite (Mg_O)

Their formation energies is given in Fig 6.1

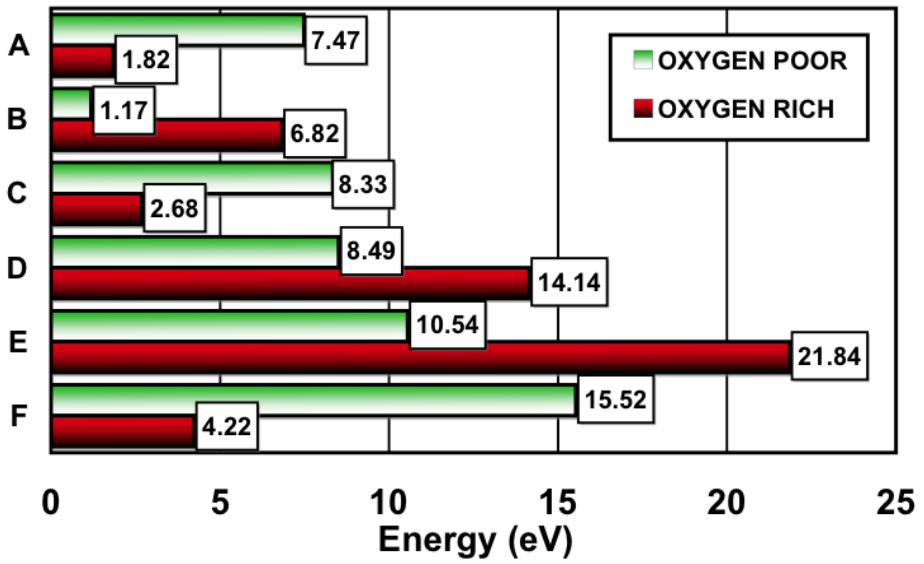

Fig: 6.1 *Defect formation energies. The upper-case letters label the defects as follows: A = Mg-vacancy, B = O-vacancy, C = Mg-interstitial, D = O-interstitial, E = Mg-antisite, F = O-antisite. The formation energies are written on top of the corresponding bars.*

Formation energy of V_O (1.17) and that of V_{Mg} (1.82) is found to be low and very close so that they have a high chance to be found in our samples as all other defects show higher formation energies. V_{Mg}, O_{Mg} and Mg_O defects display an open shell electronic structure carrying a local magnetic moment using electronic density of states and spin density calculations. Since V_{Mg} is common to both these results its reasonable to assume that if magnetism is observed in pure MgO, it may be due to V_{Mg}.

Total spin density of state of perfect and with defect (having two V_{Mg} in ferromagnetic configuration) was performed using projected augmented wave (PAW) method [64] as implemented in VASP package [65]using the parametrization obtained by Perdew and Wang (PW91) [66] and this is presented in Fig.(above). Also it can be observed from Fig: 6.2, that pristine MgO behaves like a diamagnetic semiconductor, whereas if two V_{Mg} in ferromagnetic configuration is added then it induces spin polarization on top of valence band and thus create spin-polarized holes, thus giving a p-state like character.

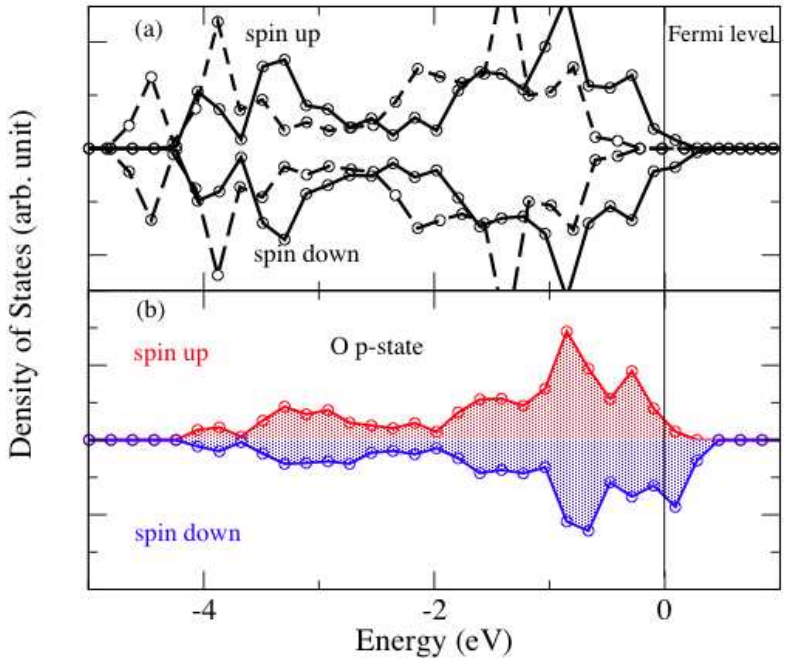

Fig: 6.2 *Total spin density of states of the pristine (dashed line) and defect (solid line) 3x3x3 supercell containing 216 atoms. In the latter, two Mg vacancies are ordered ferromagnetically. (b) Partial spin density of states project on oxygen p-states.*

The difference between the total energies (ΔE) of ferromagnetic (FM) and antiferromagnetic (AFM) configurations for defect pairs was calculated as a function of number of V_{Mg}-V_{Mg} distances. FM state was found to be the more stable one for all distances and the highest ΔE (130 meV) was found at d_0 (lattice constant of MgO). We have found a magnetic moment of around 1.9 μ_B per defect. Beyond 1.71 d_0 (corresponding to fifth fcc neighbors), ΔE drops to values lower than that of thermal energy corresponding to the room temperature (k_BT = 25.69 meV). In this case FM state cannot be stable against thermal fluctuation according to mean field theory ($k_BT_c \approx 2/3\Delta E$, where T_c is the Curie temperature) which implies that a ferromagnetic ordering at room temperature may require an interaction range of, at most, fourth fcc neighbors. For these conditions a defect concentration of the order of 10^{21} cm^{-3} would be needed to establish magnetic percolation as have been reported by Permmaraju et.al.[12] and Bergqvist et.al. [67]. We have evaluated a V_{Mg} concentration of the order of 10^{19} cm^{-3} under equilibrium growth conditions at a temperature of 3100 K (which is the melting temperature of MgO). Here, we have considered the defect population probability according to the Boltzmann factor and the oxygen poor conditions. Thus, a non-equilibrium enhancement factor of about two

orders of magnitude would be needed to observe ferromagnetic ordering in MgO at and above room temperature. Thus, our results on the magnetism in MgO come into line with the study of CaO by Pemmaraju et. al. [12].

Based on these theoretical predictions, we investigated magnetic properties of pure MgO samples grown under different conditions using sputtering, Inkjet and PLD. Results from these investigations were published in Applied Physics Letters provided in appendix.

6.5. *Investigation of d^0 magnetism in undoped and doped MgO:V nanoparticles*

6.5.1. Synthesis

The synthesis of MgO nanoparticles was accomplished using a two-step wet chemical process: 1 gram of Magnesium acetate and 0.6 gram of 2-ethanolamine (obtained from Sigma Aldrich) is dissolved in 15 ml of 2-methoxyethanol. These chemical precursors were heated on a hot plate at 130°C for 8 hours to obtain a completely dry residue at the bottom of the glass beaker. Here, 2-ethanol amine acts as capping agent, 2-methoxy ethanol acts as solvent and reducing agent. The dried residue, found to be amorphous $Mg(OH)_2$, is calcinated in 'Ar' at 450^oC for 2 hours. From this dehydration we obtain the pure and crystalline MgO nanoparticles. These powders are further calcinated at 600°C to remove all carbon components in the finally obtained uncapped MgO nanoparticles powders. The total weight of final MgO powders is around 150 mg. V doping was done using Vanadium acetate during the reaction, in appropriate quantities according to doping concentration.

6.5.2. Structural Characterization

Doped MgO systems have been under study for some time recently [52-53]. We tested MgO:V system for studying d^0 magnetism. The crystallinity of the powder material was characterized by X-Ray Diffraction (Siemens D5000 powder X-ray diffractogram) and these diffraction patterns were examined using MAUD (Material Analysis Using Diffraction) software [68] as shown in Fig: 6.3 and Table: 6.3.

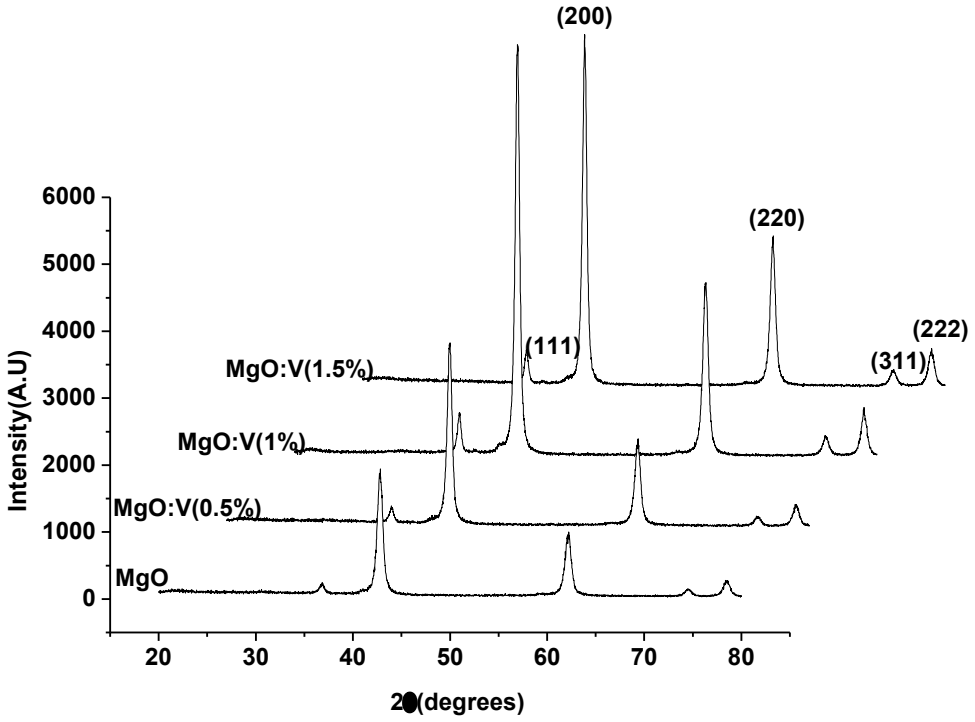

Fig: 6.3 *X-Ray Diffraction for MgO nanoparticles and MgO:V(0.5 at.%, 1 at.%, 1.5 at.%) nanoparticles matches with ICSD 80058 Cubic MgO structure with a = 4.2198Å.*

Sample Description	**Particle Size (nm) ± error(nm)**
MgO	34.85±2.87
MgO:V(0.5%)	38.25±0.20
MgO: V(1%)	38.25±4.66
MgO: V(1.5%)	38.34±2.32

Table: 6.3 *Average particle size calculated by MAUD software on X-ray diffraction data.*

XRD data reveals 38nm MgO nanocrystals of cubic structure (space group Fm-3m, ICSD#88058). No foreign phase was detected even after doping with V. Transmission Electron

Microscope (TEM) was employed for imaging and taking electron diffraction pattern to confirm the XRD results. Gatan DigitalMicrograph [69] software was employed to analyse TEM images. Energy Dispersive Spectroscopy (EDS, OXFORD D7021 Energy Dispersive X-ray Spectrometer) attached to TEM shows that all powder samples are free of any impurity and dopants are indeed present in their precursor concentration ratio. EDS for larger area was taken at an SEM (Hitachi 3000N) and the result matches with EDS at TEM which proves the purity of powder samples beyond doubt.

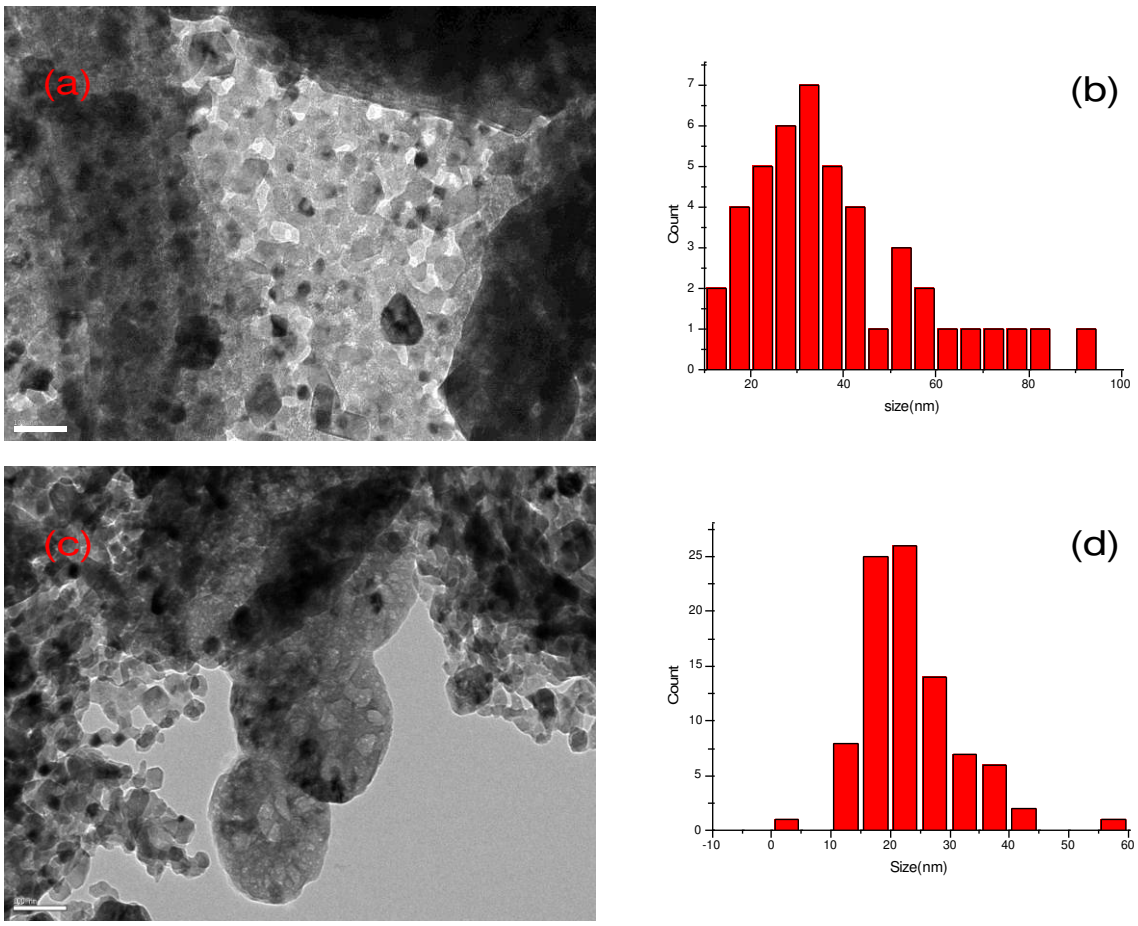

Fig: 6.4 *TEM analysis for size and size distribution for doped and undoped samples. (a) MgO:V(1%) powder TEM image. (b) Size distribution histogram for image (a) showing a mean size of 23.18nm, (c) MgO powder TEM image. (d) Size distribution for image (b) showing a mean size of 38.47 nm.*

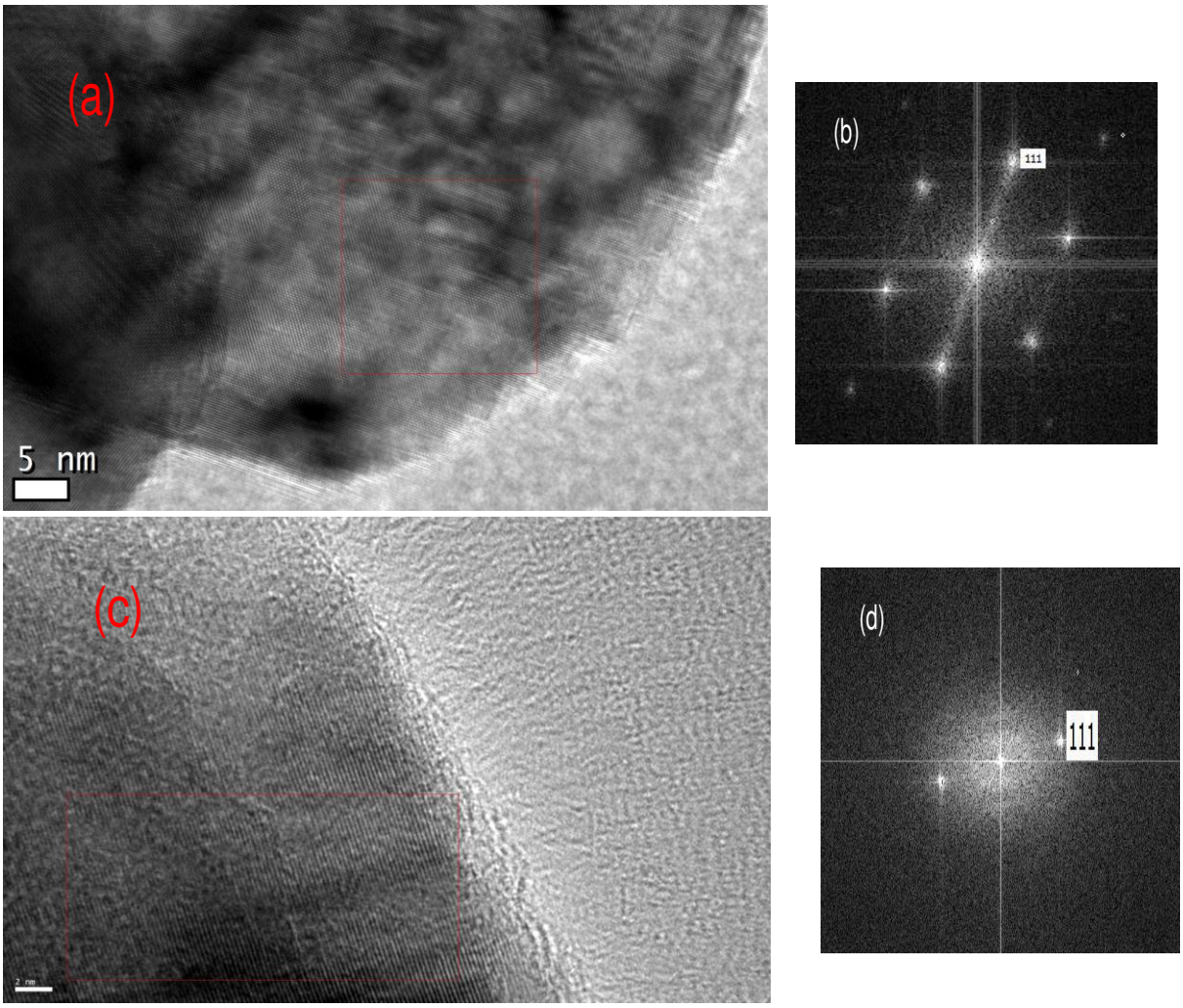

Fig: 6.5 *Lattice images for doped and undoped samples. (a) Lattice image for MgO:V(1%), (b) Reduced Fast Fourier Transform for image (a) showing (111) diffraction spot with d=2.4731Å, (c) Lattice image for MgO, (d) Reduced Fast Fourier Transform for image (c) showing (111) diffraction spot with d=2.424Å*

TEM (JEOL TEM 21000F) analysis (Fig: 6.4,6.5) confirms the XRD results about the phase and mean diameter of MgO nanocrystals and also about absence of a possible impurity phase.

6.5.3.Magnetic Characterization

SQUID (Superconducting Quantum Interference Device, MPMS2-SQUID magnetometer) was used for the characterization of the magnetic properties.

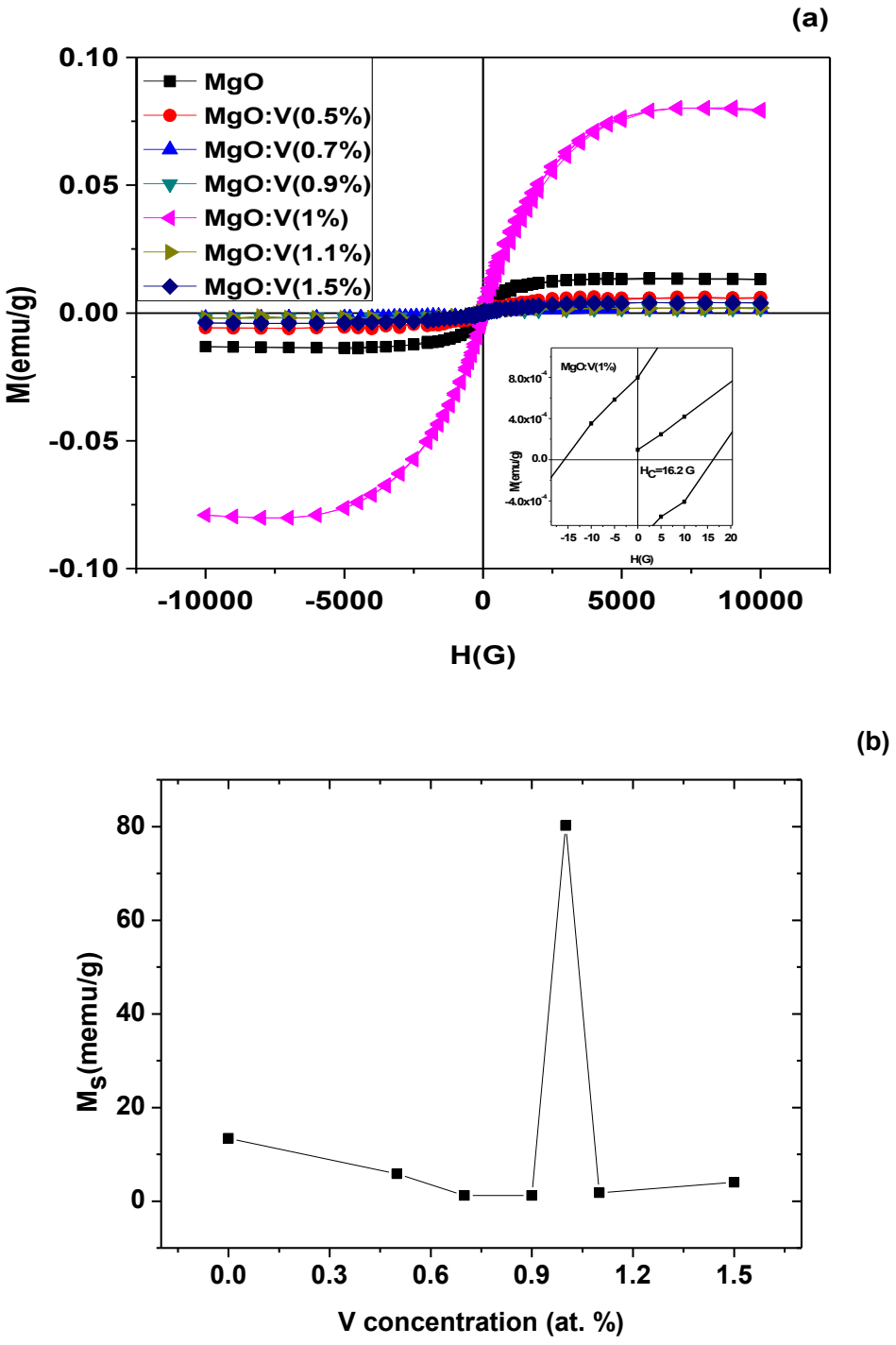

Fig: 6.6 *Hysteresis curves at room temperatures for MgO and MgO:V(0.5%, 0.7%, 0.9%, 1%, 1.1%, 1.5%) powder showing ferromagnetic behaviour.(a) ferromagnetic behaviour of undoped and V doped MgO powders at different concentrations., (b) Change in saturation magnetization with dopant concentration at 300K.*

The magnetic hysteresis curves clearly indicate robust ferromagnetism at room temperature with finite magnetic coercivity. Undoped MgO nanoparticles show saturation magnetization of 13.4 memu at room temperature. Various doping concentrations of V affect this ferromagnetic behavior differently. While 1 atomic percent doping of vanadium increases this behavior up to 80.2 memu, 0.5 and 1.5 atomic percent doping decreases it to 5.84 memu and 4.02 memu respectively. This indicates that interaction of magnetic V ion with magnetic MgO matrix depends on the local concentration of dopant. Theoretical calculations pointed out that certain distances between V_{Mg} defects are preferable for ferromagnetism and beyond fifth ffc neighbor ($1.71d_0$), ferromagnetic interactions degrade drastically. Thus it's reasonable to assume that certain concentrations of V ion degrade FM due to change in distances between V_{Mg} defects beyond $1.71d_0$.

Supporting theoretical calculations for V-doped MgO system was reported by Århammar et.al [70] where substitutional V impurities on the (001) surface and bulk were compared. 3x3x3 supercell consisting of 216 atoms was built up and one V atom was substituted ($Mg_{107}VO_{108}$) which corresponded to 0.92 at%. In the case of substation at the bulk site, V atom assumes V^{2+} charged state since 4s-like states are transferred to oxygen sites forming ionic bonds and localized 3d states of oxygen anion (O^{2-}) leading to local magnetic moment of $3\mu_B$. The V 3d states form a deep impurity band in host band gap which leads to hybridization of these with 2p orbitals of nearest neighbor (NN) oxygen atoms. The exchange splitting is greater than the crystal-field splitting which is quite large (2.13 and1.15 eV respectively) for the spin-up (down) channel with a magnetic moment of 3 μ_B/V. System remains insulating with an occupied spin up channel and empty spin down channel because V^{2+} is an isovalent ion with Mg^{2+} and hence induces only localized spins and not the itinerant carriers needed for conduction. Incorporation of one V atom in this supercell changes the volume of pristine cell from 2076.03 $Å^3$ to 2076.04$Å^3$ which is insignificant. There wasn't any significant change in lattice parameters from undoped MgO to MgO:V (1%). By adding another V atom at different distances, it was found that antiferromagnetic coupling was the most prominent magnetic interaction for the system. Then the effect of native defect like V_{Mg} was studied by placing one V_{Mg} between two V atoms placed at a distance of 1.4 d_0 in the lattice. This new configuration showed that point defects were able to form a FM state along with V dopant. Lattice also contracted in this new configuration from 2076.03 $Å^3$ to 2073.87A^3.

In the case of substitution of V atom at (001) surface, properties are significantly different. Now Fermi level lies in 3d band with majority spin channel posing metallic character. Delocalization induced metallic character indicates towards a carrier-mediated ferromagnetic ordering of the local moments as opposed to Oxygen nearest-neighbor mediated super exchange mechanism for bulk case.

Comparing our experimental results with the stated theoretical results, we find that V concentration affect its concentration in both bulk and surface of the nanocrystal. Since V dopant at surface has more pronounced effect on the ferromagnetic character than a bulk dopant so it's reasonable to assume that higher magnetic moment at 1 at % in our case is due to increase of surface dopants. When dopants are less than 1%, there aren't sufficient V atoms to induce appreciable delocalization due to oxygen NN mediated super-exchange and hence the magnetic moment is appreciably lower than that of at. 1% dopant concentration. Again, when V dopant concentration is increased to 1.5 at% then dopants enter the bulk of lattice from the surface and hence magnetic moment decreases.

6.6. *MgO thin films*

MgO thin films were fabricated from pure MgO target (2" diameter). FIB was used to check the thickness of thin films (Fig: 6.7).

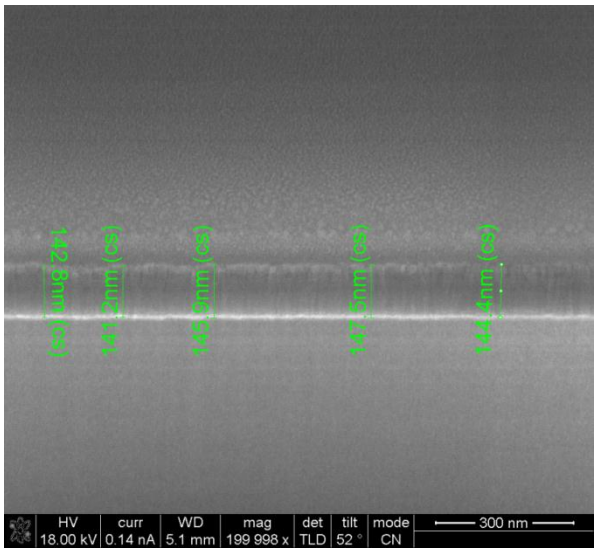

Fig: 6.7 *FIB crossection of MgO thin film for thickness measurement*

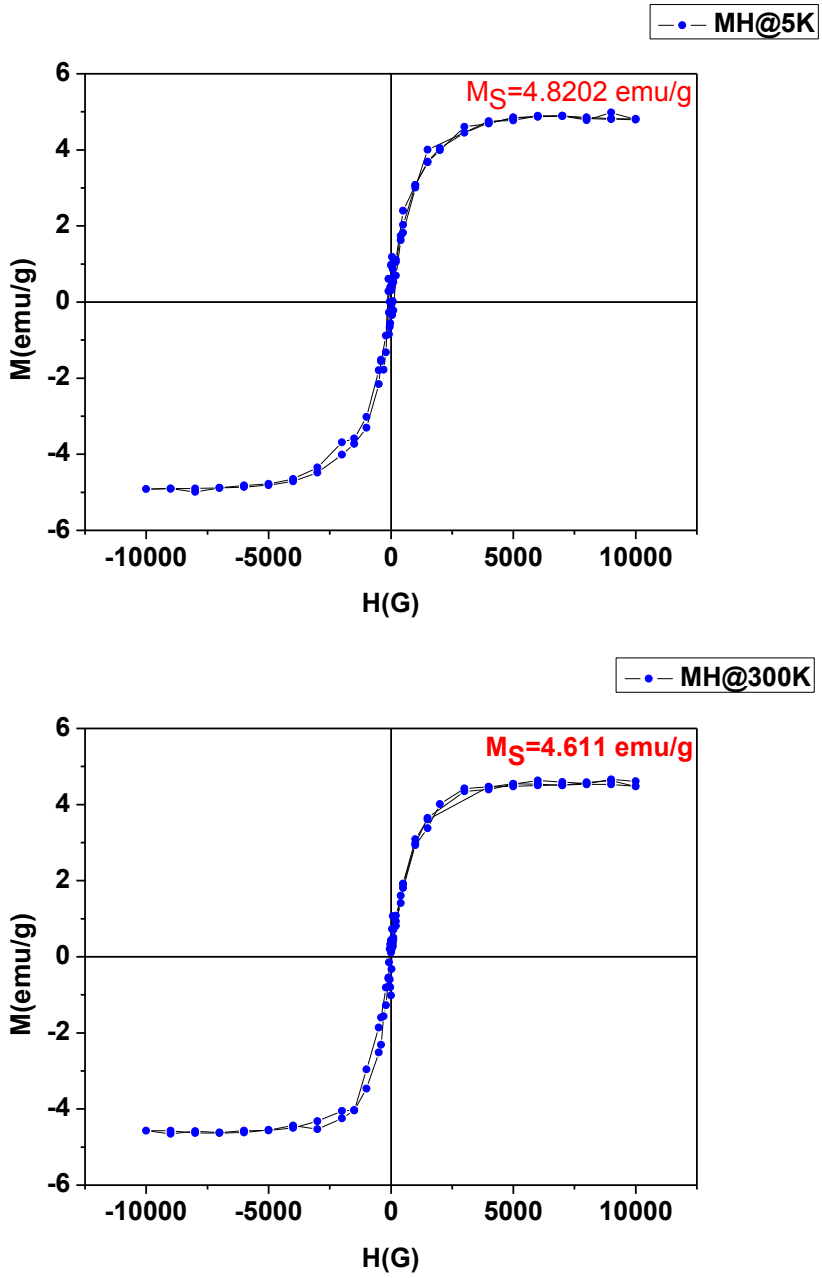

Fig: 6.8 *MH@5K and 300K for MgO thin film fabricated using PLD shows ferromagnetic hysteresis loop both at low temperatures (5K) and room temperature (300K)*

Ferromagnetic thin film was obtained for deposition of MgO thin films. Robust room temperature ferromagnetic behavior was observed and this was comparable by thin films fabricated using PLD, sputtering and inkjet printing.

6.7. ***Summary***:

Robust room temperature ferromagnetism was found in MgO (undoped and V doped) powders and undoped thin films. Using *ab-initio* calculations, experimental results were found to match theoretical results that defects are responsible for room temperature ferromagnetic behavior. On varying V dopant concentration in powders, it was found that the effect of V dopant is sensitive and critically dependent of a particular composition of 1 at% V. Further doping above 1 at.% V produces detrimental effects.

6.6.***Future work*:**

Following experiments are suggested for future work with this system:

1. Study of ferromagnetism w.r.t amount of defects
2. Fabrication of GMR structures using magnetic MgO spacer layer

6.7.*References*

1. T. F. Dossin, M.-F. Reyniers, R. J. Berger, and G. B. Marin, *Appl. Catal*., B 67**(2006)**136
2. Peter A. Teller, Jack P. Waldron, *Journal of the optical society of America* 45 **(1955)**19
3. K. Oumi, H. Matsumoto, K. Kashiwagi, and Y. Murayama, *Surf. Coat. Technol.* 169-170**(2003)** 562
4. H. S. Jung, J.-K. Lee, M. Nastasi, S.-W. Lee, J.-Y. Kim, J.-S. Park, K. S. Hong, and H. Shin, *Langmuir* 21**(2005)** 10332
5. T. Uchino and D. Okutsu, *Phys. Rev. Lett*. 101 **(2008)** 117401
6. T. Dietl, H. Ohno, F. Matsukura, J. Cibert, and D. Ferrand, *Science* 287 **(2000)** 1019
7. Buchholz, D. B., Chang R. P. H., Song, J. H., & Ketterson, J. *Appl. Phys. Lett.* 87 **(2007)** 082504
8. Hong, N., Sakai, J., & Hassini, A. *J. Appl. Phys.* 97 **(2005)** 10D312
9. Wang, Q., Sun, Q., Jena, P., Hu, Z., Note, R. & Kawazoe, Y. *Appl. Phys. Lett.* 91**(2007)**063116
10. Kenmochi, K., Dinh, V. A., Sato, K., Yanase, A., Katayama-Yoshida, H. *J. Phys. Soc. Jpn.* 73, **(2004)** 2952-2954
11. Kenmochi, K., Seike, M., Sato, K., Yanase, A., & Katayama-Yoshida, H. *Jpn J. Appl. Phys.* 43**(2004)**, L934-L936
12. Pemmaraju, C. D., & Sanvito, S. *Phys. Rev. Lett.* 94 **(2005)** 217205
13. Hong, N. H., Sakai, J., & Brize, V. *J. Phys.: Condens. Matter* 19 **(2007)** 036219
14. Wang, Q., Sun, Q., Chen, G., Kawazoe, Y., & Jena, P. *Phys. Rev. B* 77 **(2008)** 205411
15. Gupta, A. Novel Room Temperature Ferromagnetic Semiconductor. Ph.D. Thesis, ISBN 91-7283-820-5, Royal Institute of Technology, Sweden **(2004)**
16. Gupta, A., Cao, H., Parekh, K., Rao, K. V., Raju, A. R., & Waghmare, U. V. *J. Appl. Phys*. 101**(2007)** 09N513
17. Gupta, A., Owens, F. J., Rao, K. V., Iqbal, Z., Guille, J. M.O., & Ahuja, R. *Phys. Rev. B* 76 **(2006)**24449
18. Gupta, A., Li, C., Owens, F. J., Rao, K. V., Browning, N. D., & Moeck, P. *J. Mater. Res.* 22**(2007)** 1396-1405
19. Owens, F. J., Iqbal, Z., Belova, L., & Rao, K. V. *Phys. Rev B* 69 **(2004)** 011403

20. Venkatesan, M., Fitzgerald, C. B., & Coey, J. M. D. *Nature* 430 **(2004)** 630-630
21. A. M. Stoneham, Theory of Defects in Solids Clarendon, Oxford, New York, **(1975)** Ch. 16
22. I. S. Elfimov, S. Yunoki, and G. A. Sawatzky, *Phys. Rev. Lett.* 89 **(2002)** 216403
23. Coey, J. M. D., Venkatesan, M., Stamenov, P., Fitzgerald, C. B., & Dorneles, L. S. *Phys. Rev. B* 72 **(2005)** 024450
24. Mott, N. F. *Conduction in Noncrystalline Materials* (Clarendon, Oxford, **1987**)
25. Sundaresan, A., Bhargavi, R., Rangarajan, N., Siddesh, U. & Rao, C. N. R. *Phys. Rev B* 74, **(2006)** 161306
26. Hong, N. H., Sakai, J., Poirot, N., & Brize, V.*Phys. Rev. B* 73 **(2006)** 132404
27. Osorio-Guillén, J., Lany, S., Barabash, S. V., & Zunger, A. *Phys. Rev. Lett.* 17 **(2006)** 107203
28. Ohno, H. *Science* 281 **(1998)** 951-956
29. D. W. Abraham, M. M. Frank, and S. Guha, *Appl. Phys. Lett*. 87 **(2005)** 252502
30. Kesong Yang, Rongqin Wu, Lei Shen, Yuan Ping Feng,Ying Dai, and Baibiao Huang, *Phys. Rev. B* 81 **(2010)** 125211
31. N. H. Hong, J. Sakai, N. Poirot, and V. Brizé, *Phys. Rev. B* 73 **(2006)** 132404
32. K. Yang, Y. Dai, B. Huang, and Y. P. Feng, *Phys. Rev. B* 81 **(2010)** 033202
33. H. Peng, J. Li, S.-S. Li, and J.-B. Xia, *Phys. Rev. B* 79 **(2009)** 092411
34. S. Zhou, E. Cizmar, K. Potzger, M. Krause, G. Talut, M. Helm, J. Fassbender, S. A. Zvyagin, J. Wosnitza, and H. Schmidt, *Phys. Rev. B* 79 **(2009)** 113201
35. N. H. Hong, J. Sakai, and V. Brizé, *J. Phys.: Condens. Matter* 19 **(2007)** 036219
36. K. Potzger, S. Zhou, J. Grenzer, M. Helm, and J. Fassbender, *Appl. Phys. Lett.* 92 **(2008)** 182504
37. N. H. Hong, N. Poirot, and J. Sakai, *Phys. Rev. B* 77 **(2008)** 033205
38. R. P. Panguluri, P. Kharel, C. Sudakar, R. Naik, R. Suryanarayanan, V. M. Naik, A. G. Petukhov,
39. B. Nadgorny, and G. Lawes, *Phys. Rev. B* 79 **(2009)** 165208
40. P. Dev, Y. Xue, and P. Zhang, *Phys. Rev. Lett.* 100**(2008)** 117204
41. H. Jin, Y. Dai, B. Huang, and M.-H. Whangbo, *Appl. Phys. Lett.* 94 **(2009)** 162505

42. Y. Liu, Z. Lockman, A. Aziz, and J. MacManus-Driscoll, *J. Phys.: Condens. Matter* 20 **(2008)** 165201
43. C. Chen, L. He, L. Lai, H. Zhang, J. Lu, L. Guo, and Y. Li, *J. Phys.: Condens. Matter* 21**(2009)** 145601
44. J. Hu, Z. Zhang, M. Zhao, H. Qin, and M. Jiang, *Appl. Phys. Lett*. 93**(2008)** 192503
45. J. I. Beltrán, C. Monty, Ll. Balcells, and C. Martínez-Boubeta *Solid State Commun.* 149 **(2009)** 1654
46. N. Kumar, D. Sanyal, and A. Sundaresan, *Chem. Phys. Lett.* 477 **(2009)** 360,
47. A.M. Stoneham, A.P. Pathak, R.H. Bartram, *J. Phys. C: Solid State Phys*. 9 **(1976)** 73.
48. H. Pan, J. B. Yi, L. Shen, R. Q. Wu, J. H. Yang, J. Y. Lin, Y. P. Feng, J. Ding, L. H. Van, and J. H. Yin, *Phys. Rev. Lett*. 99 **(2007)** 127201
49. C.-F. Yu, T.-J. Lin, S.-J. Sun, and H. Chou, *J. Phys. D* 40 **(2007)** 6497
50. L. Shen, R. Q. Wu, H. Pan, G. W. Peng, M. Yang, Z. D. Sha, and Y. P. Feng, *Phys. Rev. B* 78**(2008)** 073306
51. S. Zhou, Q. Xu, K. Potzger, G. Talut, R. Grotzschel, J. Fassbender, M. Vinnichenko, J. Grenzer, M. Helm, H. Hochmuth, M. Lorenz, M. Grundmann, and H. Schmidt, *Appl. Phys. Lett.* **93 (2008)** 232507
52. A. Droghetti and S. Sanvito, *Appl. Phys. Lett*. 94, **(2009)** 252505,
53. B. Gu, N. Bulut, T. Ziman, and S. Maekawa, *Phys. Rev. B* 79 **(2009)**024407
54. K. Yang, Y. Dai, B. Huang, and M.-H. Whangbo, *Appl. Phys. Lett.* 93 **(2008)** 132507
55. Y. Bai and Q. Chen, *Solid State Commun.* 147**(2008)**169
56. K. Yang, Y. Dai, B. Huang, and M.-H. Whangbo, *Chem. Phys. Lett.* 481 **(2009)** 99
57. A. Droghetti, C. D. Pemmaraju, and S. Sanvito, *Phys. Rev. B* 81. **(2010)** 092403
58. Butler, W. H., Zhang, X. G., Schulthess, T. C., & MacLaren, J. M. *Phys. Rev. B* 63 **(2001)** 054416
59. Mathon, J., & Umerski, A. *Phys. Rev. B* 63 **(2001)** 220403
60. Yuasa, S., Nagahama, T., Fukushima, A., Suzuki, Y., & Ando K., *Nature Mater.* 3 **(2004)** 868-871
61. Diao, Z. T., Pakala, M., Panchula, A., Ding, Y. F., Apalkov, D., Wang, L. C., Chen, E., & Huai Y. M. *J. Appl. Phys.* **99 (2006)** 08G510

62. Narayan, J., Nori, S., Pandya, D. K., Avasthi, D. K., & Smirnov, A. I. *Appl. Phys. Lett.* 93 **(2008)** 082507

63. C. Martínez-Boubeta, J. I. Beltrán, Ll. Balcells, Z. Konstantinović, S. Valencia, D. Schmitz, J. Arbiol, S. Estrade,J. Cornil, and B. Martínez, *Phys. Rev. B* 82 **(2010)** 024405

64. P. E. Blöchl, *Phys. Rev. B* 50 **(1994)** 17953

65. G. Kresse, and J. Furthmüller, *Phys. Rev. B* 54 **(1996)** 11169

66. J. P. Perdew, and Y. Wang, *Phys. Rev. B* 45 **(1992)** 13244

67. Bergqvist, L., Eriksson, O., Kudrnovský, J., Drchal, V., Bergman, A., Nordström, L., & Turek, I. *Phys. Rev. B* 72 **(2005)** 195210

68. L. Lutterotti, S. Matthies, and H.-R. Wenk. "MAUD: a friendly Java program for material analysis using diffraction." *IUCr: Newsletter of the CPD*, 21:14--15, **(1999)**

69. D. R. G. Mitchell, DiffTools: Software Tools for Electron Diffraction in Digital Micrograph.' *Microscopy Research and Technique*, **71,** 588-593**(2008)**

70. C. Århammar, C. Moyses Araujo, K. V. Rao, Susanne Norgren, Börje Johansson and Rajeev Ahuja, *Phys. Rev. B* 82 **(2010)** 134406